PROTECT2024

9th International Colloquium on Performance, Protection & Strengthening of Structures Under Extreme Loading & Events

13 - 16 August 2024 I Singapore

CONFERENCE PROCEEDINGS

Organised by

NANYANG TECHNOLOGICAL UNIVERSITY SINGAPORE

NTU CEE Alumni Association

LIST OF TECHNICAL PAPERS

ID Number	Authors (s) – Paper Title
PCS-1	***Alex Sixie Cao, Andrea Frangi*** – Progressive Collapse Of A Timber Frame Building Subjected To Single-And Multi-Column Damage Scenarios
PCS-2	***Yumei Zhang, Junshan Liu, Bo Yang, Kang Chen –*** Experimental Study On Progressive Collapse Behavior For Beam-column Substructure Of Modular Steel Building
PCS-14	***Manrong Song, Xiaolong Chen, Jiaxuan He, Jingfeng Wang, Ruixue Cao, Yuwei Jin, Shenjiang Huang, Bingkang Liu*** – Performance And Mechanism Of Prestressed Fabricated Concrete Frame To Resist Progressive Collapse With A Side Column Failure
PCS-15	***Van Hung Nguyen, Xuan Dat Pham, Kang Hai Tan*** – Application Of Headed Bars In Precast Concrete Wet Joints Under Accidental Loads: Experimental And Numerical Investigations
PCS-16	***Xuan Dat Pham, Trung Hieu Nguyen, Ngoc Tan Nguyen, Kim Anh Do, Anh Tuan Pham, Quoc Cuong Tran, Truong Thang Nguyen, Van Hung Nguyen*** – Experimental Study On The Collapse Response Of Reinforced Concrete Flat Slab Structures With Column Capitals
PCS-18	***Hai-Rong Shi, Chun-Lin Wang, Jun Yu, Shaoping Meng*** – Experimental Investigation Of Unbonded And Bonded Post-tensioned Precast Concrete Frames Subject To A Penultimate Column Loss
PCS-20	***Bao Yintong, Qiao Meixia, Tan Kang Hai*** – Easy-to-use analytical model of compressive arch action of bi- directional primary RC beams in framed structures under different column removal scenarios

PROGRESSIVE COLLAPSE OF A TIMBER FRAME BUILDING SUBJECTED TO SINGLE- AND MULTI-COLUMN DAMAGE SCENARIOS

Alex Sixie Cao[1] and Andrea Frangi[2]

[1] Mr., ETH Zurich, Institute of Structural Engineering, cao@ibk.baug.ethz.ch.

[2] Prof. Dr., ETH Zurich, Institute of Structural Engineering, frangi@ibk.baug.ethz.ch.

Corresponding Author: Alex Sixie Cao, M.Sc.

ETH Zurich, Institute of Structural Engineering, Stefano-Franscini-Platz 5, 8093, Zurich, Switzerland

Email: cao@ibk.baug.ethz.ch

ABSTRACT

As part of the transition to a more sustainable future, more and larger multi-storey timber buildings are being realised. Simultaneously, the frequency and magnitude of potential hazards have been increasing. Therefore, the resistance of timber buildings to disproportionate collapse is becoming increasingly relevant. However, current robustness guidelines to limit disproportionate collapse were developed for reinforced concrete and steel buildings and are inappropriate for timber buildings. Consequently, there is an urgent need to bridge the knowledge gap on the robustness of timber buildings. To investigate the robustness of buildings, it is common to assess single-column damage scenarios on the ground-floor. However, recent research has shown that relevant damage scenarios are not limited to ground-floor damage. Various hazards, such as vehicle impact and far-field blast loading, may entail damage to multiple columns. To address these knowledge gaps, this paper presents a case study of a timber frame building subjected to single- and multi-column damage scenarios. A damage assessment and sensitivity analyses were conducted, where the societal and material consequences were quantified based on the life quality index. The analyses are conducted using a recently developed framework for modelling progressive collapse of inelastic building structures using nonlinear dynamic analysis.

Keywords: *Progressive Collapse, Multi-Column Damage Scenarios, Timber, Numerical Modelling, Consequence Assessment, Life Quality Index, Societal Willingness-to-Pay*

1. INTRODUCTION

The world is currently witnessing an increase in both the frequency and magnitude of extreme weather events, which has resulted in global losses of over 143 billion USD per year in the period between 2000 and 2019 [1]. In the same period, the frequency and consequences of terrorism have increased [2]. With the increasing frequency of natural and man-made hazards, society should invest in measures to reduce the vulnerability to extreme events and to increase the resilience and robustness of the built environment.

A robust structure is insensitive to initial damage and is less susceptible to experiencing a progressive or disproportionate collapse [3]. Most of the current building stock comprises reinforced concrete or steel buildings, and the research on robustness or progressive collapse has mainly been focused on such buildings [4]. With the increasing volume of modern timber buildings and the limited robustness research on such structures, increasing the knowledge of the progressive collapse of modern timber buildings is urgently needed [5].

To investigate the robustness of a structure, it is common to assess single ground-floor column-loss scenarios [4]. However, single ground-floor column-loss scenarios may not be surrogates for the damage scenarios stemming from low-probability high-consequence events. Such events may cause initial damage to multiple members elsewhere in a building [6]. Therefore, initial damage scenarios comprising single-member damage or ground-floor damage should not be used exclusively to assess the robustness of a whole structure.

There are several methods to quantify the robustness of a structure [4]. Risk-based methods may be advantageous over other methods as they include both the probabilities of the various components leading to a collapse and the resulting consequences. Baker et al. [7] proposed a risk-based robustness index $I_{Rob}=R_d/(R_d+R_{id})$, where R_d is the direct risk and R_{id} is the indirect risk of the initial damage. Voulpiotis et al. [8] used the risk-based robustness index I_{Rob} to quantify the robustness of a tall timber building, but only considered the material consequences. However, the material losses may be dwarfed by the societal losses that stem from the loss of life. Therefore, a risk-based method to assess the robustness should include not only the material consequences but also the societal consequences.

In this paper, the robustness of a multi-storey timber building was investigated. The building was designed for vertical and lateral loading in Switzerland according to the Eurocodes [9–12]. Two single-column and two multi-column damage scenarios were assessed using a state-of-the-art modelling framework for progressive collapse [13]. The modelling framework for progressive collapse uses nonlinear dynamic analysis to simulate a building collapse from the initial damage to its final collapsed state. To quantify the consequences of the damage scenarios, the material consequences were estimated based on assumed construction costs. The societal consequences were derived using the societal willingness-to-pay based on the life quality index [14] and an empirical expression for the fatality estimation [15]. To quantify the uncertainties of the material and societal consequences, sensitivity analyses were conducted on the societal willingness-to-pay and the total consequences using UQLab [16].

2. THEORETICAL BACKGROUND

2.1. Progressive collapse analyses

For the progressive collapse analyses, a state-of-the-art modelling framework for progressive collapse was used [13]. The modelling framework is fully parametric for buildings with structural members following an orthogonal grid and includes features such as element separation and removal [17], debris tracking and impact loading [18], failure criteria with rate-dependent effects for glued laminated timber subjected to impact loading [19,20], nonlinear and incremental damping [21], and hysteresis in the beam-column connection model [22].

The modelling framework can model beam-column members, trusses, and planar members, such as walls and slabs. It can assess single- and multi-member damage scenarios in a sequential or simultaneous manner. The modelling framework was implemented in Python 3.10 using the Python 3.10 interpreter of the open-source finite element framework OpenSees [23]. Full details on the modelling framework can be found in Cao et al. [13].

2.2. Consequence assessment

2.2.1. Societal consequences

The life quality index L can be defined as:

$$L = g^{q} e\,(1\text{-}w), \tag{1}$$

where w is the lifetime work-leisure ratio, e is the life expectancy, g is the gross national product per capita [14]. The gross national product per capita can be modelled using the Cobb-Douglas production model:

$$g = k^{1-\beta} w^{\beta}, \tag{2}$$

where k is the capital input, w is the labour input, and β is the output elasticity of labour [24]. The output elasticity of labour β can be estimated as the fraction of wages to the gross national product g. By substituting the Cobb-Douglas production model for the gross national product per capita g in Eq. (2) into the life quality index L in Eq. (1) and assuming that the life quality index L must be increasing, the parameter q can be derived as [25]:

$$\frac{\mathrm{d}L}{\mathrm{d}w} = 0 \therefore q = \frac{1}{\beta}\frac{w}{1\text{-}w}. \tag{3}$$

Accounting for the demographics of a country and discounting, the societal willingness-to-pay ($SWTP$) can be derived from the life quality index L in Eq. (1) as:

$$SWTP = \frac{g}{q} J_{\Delta}, \tag{4}$$

where J_{Δ} is a demographic constant that accounts for demographics, discounting rate γ, and a constant mortality reduction scheme [26,27].

Caredda et al. [6] recommended the empirical model by Hingorani et al. [15] to estimate the fatalities in a progressive collapse. Hingorani et al. [15] collected data on over 150 wholly or partially collapsed buildings to determine the following model for fatality estimations n_f:

$$n_f = 0.26 \cdot \frac{A_c^{0.89}}{CC^{0.7}} \cdot 0.38^{CE}, \tag{5}$$

where A_c is the collapsed floor area, CC is a factor accounting for the consequence class, and CE is 0.34 for multi-storey buildings. For consequence class 2, CC is 30. Using Eq. (4) and (5), the societal consequences c_s can be estimated from:

$$c_s = SWTP \cdot n_f. \tag{6}$$

2.2.2. Material consequences

The material consequences c_m can be estimated by considering the collapsed building volume or floor area. By assuming that the material consequences c_m are the cost associated with the original construction of the building, they can be estimated from:

$$c_m = A_c \cdot c_c, \tag{7}$$

where A_c is the collapsed floor area and c_c is the construction cost per floor square meter.

The collapsed floor area A_c can be determined from the progressive collapse simulations. In this paper, the slabs were assumed to be simply supported on all four sides and confined to one bay. If at least two intersecting and perpendicular beams were collapsed, the slab of a bay was defined as collapsed.

2.2.3. Consequence and robustness estimation

The conditional total consequences for a given damage scenario $c_t|D_i$ can be computed from its societal c_s and material c_m consequences in Eq. (6) and (7):

$$c_t|D_i = c_s + c_m = \left(0.26 \cdot \frac{A_{c,i}^{0.89}}{CC^{0.7}} \cdot 0.38^{CE}\right) SWTP + A_{c,i} c_c, \tag{8}$$

and can be used to quantify and compare the total consequences of a specific damage scenario.

The conditional robustness index for a specific damage scenario $I_{Rob}|D_i$ can be defined as :

$$I_{Rob}|D_i = \frac{(R_d|D_i)}{(R_d|D_i)+(R_{id}|D_i)}, \tag{9}$$

where D_i is a specific damage scenario, R_d is the direct risk, and R_{id} is the indirect risk [7]. The advantage of the conditional robustness index $I_{Rob}|D_i$ in Eq. (9) over the total robustness index $I_{Rob}=R_d/(R_d+R_{id})$ is that the robustness of specific damage scenarios can be assessed individually. The conditional direct risk simplifies to $R_d|D_i=c_d$ and the conditional indirect risk to $R_{id}|D_i=P(C|D_i)c_{id}$. Therefore, the conditional robustness index $I_{Rob}|D_i$ becomes:

$$I_{\mathrm{Rob}}|D_i=\frac{c_{\mathrm{d}}}{c_{\mathrm{d}}+\mathrm{P}(C\,|D_i)c_{\mathrm{id}}} \tag{10}$$

where the direct consequence c_{d} is associated with the initial damage scenario and the indirect consequence $c_{\mathrm{id}}=c_{\mathrm{t}}$ in Eq. (8) with the resulting progressive collapse. In this paper, the direct risk R_{d} is associated with the initial damage scenario and the indirect risk R_{id} with the final collapsed state and its associated material c_{m} and societal consequences c_{s}.

3. MATERIALS AND METHOD

3.1. Materials

A double-symmetric 5-storey timber frame building with five bays in each horizontal direction, rigid column-column and flexible beam-column steel-to-timber connections with laterally loaded dowels and slotted-in steel plates was designed according to the Eurocodes EN 1990:2002, EN 1991-1-4:2005, and EN 1995-1-1:2004 in the serviceability and ultimate limit states for gravity and wind loads [9–11]. For service-level wind-induced vibrations, the acceleration criterion from ISO 10137:2007 was used [12]. A utilisation of approximately 80% was targeted in the design.

The beam cross-sections were designed using the load combination:

$$q_{\mathrm{Ed}}=\gamma_{\mathrm{G}}g_{\mathrm{k}}+\gamma_{\mathrm{Q}}q_{\mathrm{k}}, \tag{11}$$

where q_{Ed} is the design load, $\gamma_{\mathrm{G}}=1.35$ is the partial factor for permanent actions, $\gamma_{\mathrm{Q}}=1.5$ is the partial factor for variable actions, $g_{\mathrm{k}}=3.5$ kN/m^2 is the permanent action, and $q_{\mathrm{k}}=3.0$ kN/m^2 is the variable action. The column cross-sections were designed using the load combination:

$$q_{\mathrm{Ed}}=n_{\mathrm{s}}\left(\gamma_{\mathrm{G}}g_{\mathrm{k}}+\gamma_{\mathrm{Q}}q_{\mathrm{k}}\right)\alpha_{\mathrm{N}}, \quad \alpha_{\mathrm{N}}=\frac{2+(n_{\mathrm{s}}-2)\psi_0}{n_{\mathrm{s}}}, \tag{12}$$

where n_{s} is the number of storeys, α_{N} is a reduction factor to account for the non-simultaneous maximum loading of all the storeys, and $\psi_0=0.7$ is a combination coefficient.

To determine the governing load combination for wind and gravity loading, the following load combination was used:

$$q_{\mathrm{Ed}}=\max\{\gamma_{\mathrm{G}}g_{\mathrm{k}}+\gamma_{\mathrm{Q,G}}q_{\mathrm{G},1}+\psi_{0,i}q_{\mathrm{k,W}};\ \gamma_{\mathrm{G}}g_{\mathrm{k}}+\gamma_{\mathrm{Q,G}}q_{\mathrm{W},1}+\psi_{0,i}q_{\mathrm{k,G}}\}, \tag{13}$$

where $\psi_{0,i}=0.7$ is the combination coefficient of the variable wind action, and subscript W denotes wind and G gravity.

Material parameters according to EN 14080:2013 for GL24h spruce glued laminated timber subjected to medium-term loads were used in the design [28]. Using Equations (11, (12, and (13 and a storey height of 3500 mm and a bay length of 6000 mm, the resulting column cross-section was 400×400 mm and the beam cross-section 120×840 mm. The beam-column steel-to-timber connections were designed assuming a single slotted-in S235 steel plate and Ø10 mm S235 steel dowels arranged in an orthogonal manner, with minimum spacing according to EN

1995-1-1:2004 [10]. The resulting beam-column connection comprised 8 dowels perpendicular-to-the-grain and 13 dowels parallel-to-the-grain, with an elastic rotational stiffness k_θ of 60 549 kNm/rad, elastic moment capacity M_R 405 kNm, and a rotational capacity θ_u of 19 mrad. In the progressive collapse analyses, the accidental load combination according to EN 1990:2002 [9] with an accidental combination coefficient ψ of 0.3 and mean strength values for GL24h spruce glued laminated timber [29] were used.

For Switzerland, the *SWTP* for various discount rates were determined, where the work-leisure ratio w includes the average annual working hours, commuting time, labour entry, and retirement. For the construction cost c_c, a Swiss market value of 3 497 CHF/m^2 (2021) was used based on a multi-storey residential timber frame building [30].

3.2. Sensitivity analysis

Sensitivity analyses were conducted with the uncertainty quantification framework UQLab [16] to quantify the uncertainties of the *SWTP* and its influence on the total consequences c_t. To quantify the uncertainties, total Sobol indices S_j^T were determined using polynomial chaos expansions [31], with a sampling space of 10 000 and a polynomial degree of five. For the total Sobol indices S_j^T, the importance of parameter j was established. If the parameters do not show any interactions, the sum of the total Sobol indices is less than unity $\Sigma_j S_j^T \leq 1$.

The probabilistic parameters for the sensitivity study of the *SWTP* and the total consequences c_t are given in Table 1. In Table 1, m is the mean value, $cov=s/m$ is the coefficient of variation, and s is the standard deviation. The log-normal parameters $\mathcal{LN}(\lambda,\zeta)$ are defined as $\lambda=\ln m - \zeta^2/2$ and $\zeta=(\ln(cov^2+1))^{1/2} \approx cov$.

Table 1. Parameters for the sensitivity study of the *SWTP* and the total consequences c_t.

Parameter	Distribution	Distribution parameters
γ (%)	Log-normal [m,cov]	[5,0.1]
w (-)	Log-normal [m,cov]	[0.10,0.10]
g (CHF/capita)	Log-normal [m,cov]	[82 657,0.03]
β (-)	Log-normal [m,cov]	[0.68,0.01]
A_c (m^2)	Constant	500
SWTP (kCHF)	Log-normal [m,cov]	[8 361,0.12]
c_c (CHF/capita)	Log-normal [m,cov]	[3 497,0.20]
c_d (CHF)	Log-normal [m,cov]	[1 500,0.50]
n_f (-)	Log-normal [m,cov]	[4.37, 0.50]

4. RESULTS AND DISCUSSION

4.1. Progressive collapse

The various damage scenarios D_i of the timber building are shown on the left and the final collapsed state on the right side of Figure 1. For the single-member damage scenarios, an internal column-loss scenario on the ground floor in Figure 1a and on the first floor in Figure 1c was simulated. For the multi-column damage scenarios, an edge and an internal column removal on the ground floor in Figure 1e and on the first floor in Figure 1g were assessed.

In the damage scenarios D_i, the building collapsed progressively to different extents. For the ground-floor damage scenarios D_i, the collapses progressed to all the floors in Figure 1b and Figure 1f. Contrary to the ground-floor damage scenarios D_i, the first-floor damage scenarios D_i did not result in the collapse of the structure beneath in Figure 1d and Figure 1h. This shows that the building could not develop alternative load paths, such as catenary action. However, the building could resist the impact loading from the debris of failed members.

When considering the composite rotational stiffness K_θ of the beam with the connections [13], the composite stiffness K_θ was about twice that of a beam with rigid connections and the elastic moment capacity M_R of the connections was smaller than the beam. Therefore, the behaviour of the building was governed by its connections. In this specific case, a minimum vertical deflection w of approximately 180 mm would be necessary to develop catenary action [32]. This is equivalent to a minimum rotational capacity $\theta_{u,min}$ of 30 mrad for an idealized system with flexurally rigid beams. However, the rotational capacity of the connections was smaller $\theta_u < \theta_{u,min}$. Therefore, the structure was unable to develop catenary action to arrest the progressive collapses of the damage scenarios D_i.

The pre-collapse maximum deformations w_{max} were similar for all the damage scenarios D_i. However, the time from the onset of damage until the final collapsed state was quite different. For the ground-floor damage scenarios D_i, the difference in the duration of the progressive collapse was approximately 13%. In comparison, the first-floor damage scenarios had a difference of approximately 38% and they were also shorter than the ground-floor damage scenarios D_i. If the duration is assessed together with the damage extent, it can be inferred that a longer duration may be used as an indicator of the severity of a progressive collapse.

4.2. Societal willingness-to-pay

In Table 2, the *SWTP* is presented using parameters for Switzerland in 2022. Depending on the discounting rate γ, the *SWTP* was between 7 123 and 9 356 kCHF (2022) based on the life quality index. Hürzeler et al. found that the value of a statistical life in Switzerland in 2020 was 6 915 kCHF (2022, adjusted for inflation) [33], and a meta-analysis by the OECD based on surveys found that it was 5 340 kCHF in 2009 (2022, adjusted for inflation) [34]. For assessing risk reduction measures in Swiss structures, SIA 269:2011 provides a range between 3 and 10 million CHF for the marginal lifesaving cost [35] and the SIA 269/8:2017 defines it as 10 million CHF [36]. Kägi et al. determined that the median value of the willingness-to-pay in road traffic was 8 379 kCHF (2022, adjusted for inflation) [37], and Fischer found the *SWTP* was 5.0 million CHF in 2010 (2022, adjusted for inflation) [38].

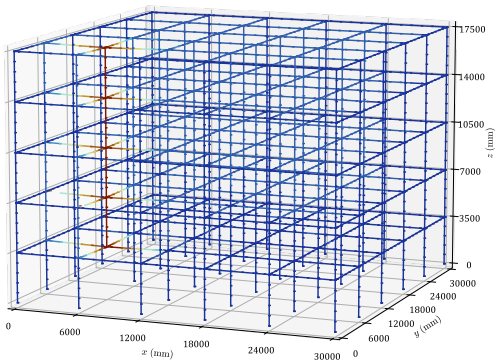

(a) x01-y01-z00, t=124 ms, w_{max}= 91 mm

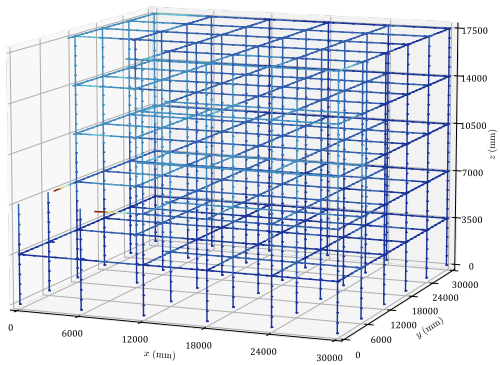

(b) x01-y01-z00, t=960 ms, w_{max}= 87 mm

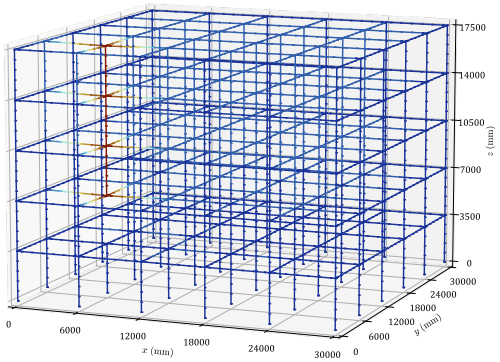

(c) x01-y01-z01, t=116 ms, w_{max}= 88 mm

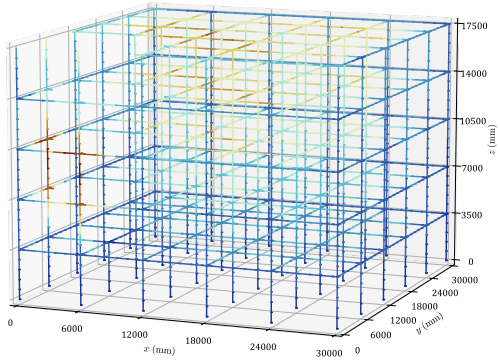

(d) x01-y01-z01, t=386 ms, w_{max}= 16 mm

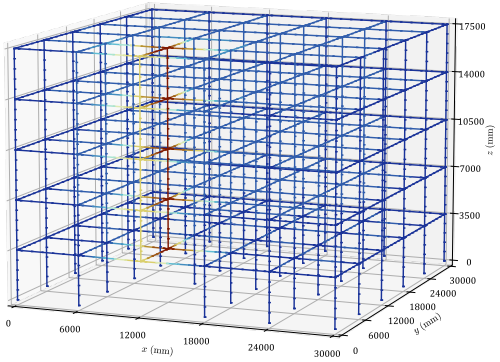

(e) x01/02-y01-z00, t=100 ms, w_{max}= 80 mm

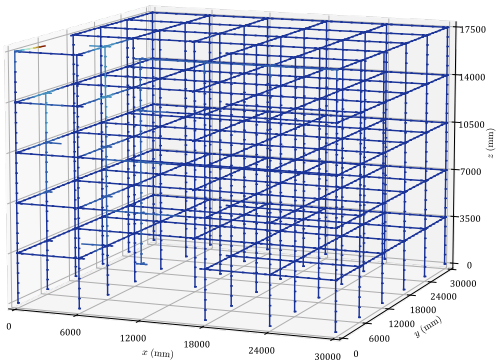

(f) x01/02-y01-z00, t=846 ms, w_{max}= 266 mm

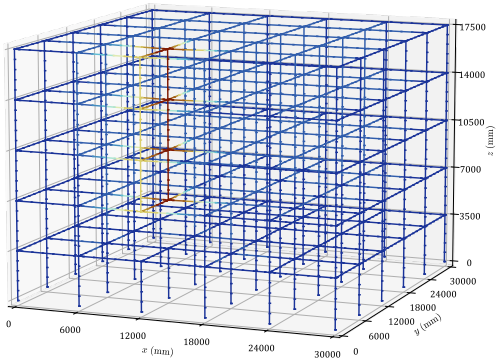

(g) x01/02-y01-z00, t=124 ms, w_{max}= 86 mm

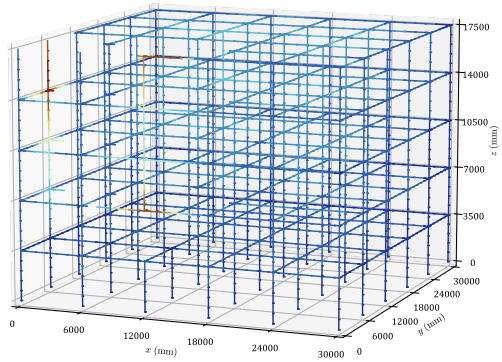

(h) x01/02-y01-z00, t=536 ms, w_{max}= 40 mm

Figure 1. Maximum deformations w_{max} before the initial failure (left) and after the final failure (right).

Table 2. *SWTP* in Switzerland in Swiss Francs (CHF, 2022). [a]Between 2013 and 2022. [b]Between 2011 and 2020. [c]Mortality distribution and population pyramid in 2019. 1 CHF ≈ 1.05 USD (2022).

SWTP (kCHF)	J_Δ (-)	γ (%)	*g* (CHF)	*w* (-)	*e* (years)	*β* (-)
7 123	14.9[c]	6	82 657[a]	0.091[a]	82.8[a]	0.68[b]
7 762	16.2[c]	5				
8 505	17.8[c]	4				
9 356	19.6[c]	3				
References	[39,40]	[38,41,42]	[43]	[44–48]	[46]	[49]

Table 3. Consequences of the initial damage scenarios D_i in Figure 1 using the *SWTP* in Table 4.

Damage scenario D_i	A_c (m^2)	c_d (kCHF)	$c_{m,id}$ (kCHF)	n_f (-)	γ (%)	c_s (kCHF)	c_t (kCHF)	$I_{Rob}\|D_i$ $\times 10^{-3}$ (-)
x01-y01-z00	720	7	2 518	6.0	6	43 033	52 551	0.133
					5	46 894	56 412	0.124
					4	51 382	60 900	0.115
					3	56 524	66 042	0.106
x01-y01-z01	576	7	2 014	5.0	6	35 282	44 296	0.158
					5	38 447	47 461	0.148
					4	42 127	51 142	0.137
					3	46 343	55 357	0.127
x01/02-y01-z00	792	14	2 770	6.6	6	46 843	63 612	0.220
					5	51 045	67 815	0.206
					4	55 931	72 701	0.193
					3	61 528	78 297	0.179
x01/02-y01-z01	648	14	2 266	5.5	6	39 181	55 447	0.253
					5	42 696	58 962	0.237
					4	46 783	63 049	0.222
					3	51 464	77 730	0.180

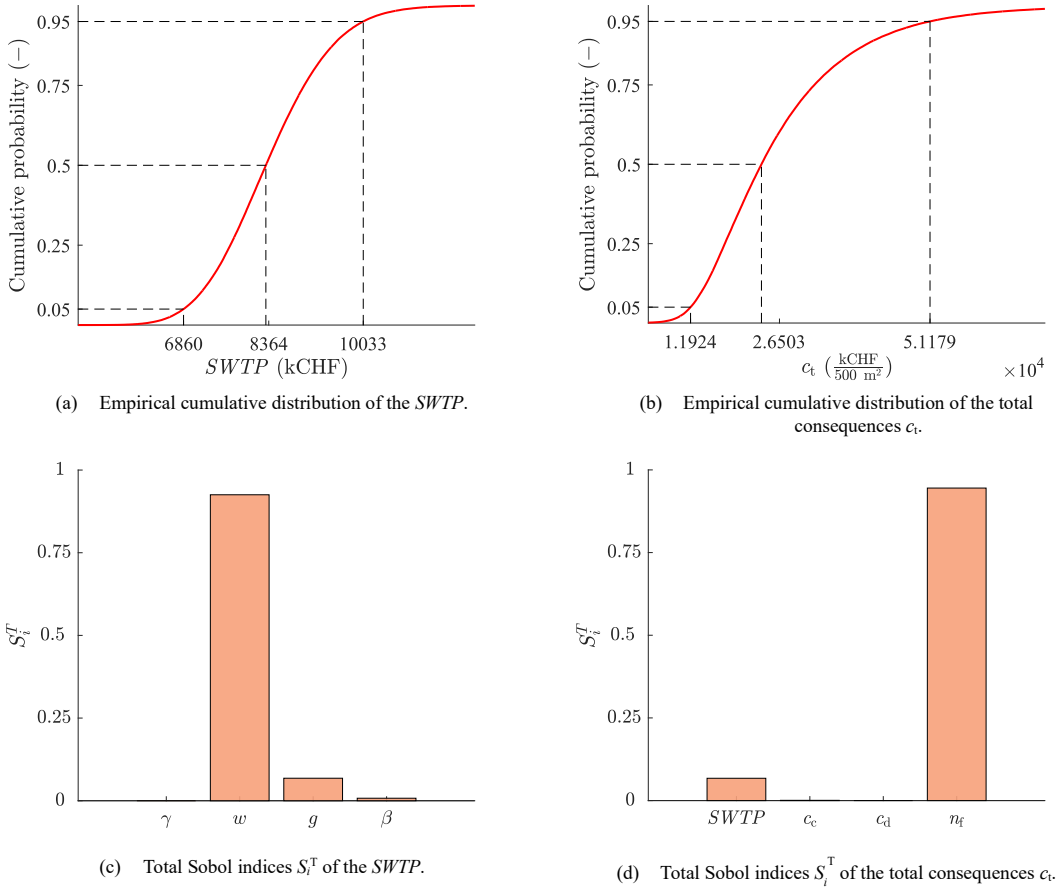

(a) Empirical cumulative distribution of the *SWTP*.

(b) Empirical cumulative distribution of the total consequences c_t.

(c) Total Sobol indices S_i^T of the *SWTP*.

(d) Total Sobol indices S_i^T of the total consequences c_t.

Figure 2. Empirical cumulative distributions and the total Sobol indices S_i^T of the *SWTP* and the total consequences c_t per 500 m^2.

The results from the sensitivity analysis on the *SWTP* are shown in Figure 2a and Figure 2c. With the assumed probabilistic parameters in Table 1, the mean *SWTP* was 8 364 kCHF in 2022, with a lower 5-percentile value of 6 860 kCHF and an upper 95-percentile value of 10 033 kCHF. The coefficient of variation *cov* of the *SWTP* was 11.5%. The *SWTP* in Table 2 is reasonable when compared with the results from the sensitivity study and the aforementioned literature. Figure 2c shows the Sobol indices S_i^T of the *SWTP*. The most important parameter was the work-leisure balance *w*. For a certain discounting rate γ, the most important parameters for the *SWTP* were the work-leisure balance *w* and the gross national product *g*.

4.3. Consequence estimation

Table 3 shows the consequences of the damage scenarios D_i in Figure 1. When comparing the indirect material consequences $c_{m,id}$ with the assumed direct consequences c_d of the damage scenarios D_i, the direct consequences c_d are inconsequential. Even if the assumed direct consequences c_d are increased tenfold, the direct consequences c_d will only amount to between 2.9 and 5.9% of the indirect material consequences $c_{m,id}$. The comparison becomes starker if the direct consequences c_d or the indirect material consequences $c_{m,id}$ are compared with the

societal consequences c_s. The societal consequences c_s are in the order of 20 times larger than the indirect material consequences $c_{m,id}$. Although there are large uncertainties associated with the societal consequences c_s, the consequences attributed to the loss of life dwarf the material consequences. This is also reflected in the manner many media outlets portray building collapses, where a collapse is subjectively portrayed as more severe if loss of life is incurred.

The damage conditional robustness index $I_{Rob}|D_i$ is presented in Table 3 for the various damage scenarios D_i and is between 0.106×10^{-3} and 0.253×10^{-3}, depending on the damage scenario and the discount rate γ. Using the conditional robustness index $I_{Rob}|D_i$, the building is the least robust for the ground-floor single-column damage scenario x01-y01-z00 in Figure 1a as it has the lowest conditional robustness index $I_{Rob}|D_i$. Even if the collapsed area A_c is larger for the ground-floor double-column damage scenario x01/02-y01-z00 in Figure 1e, the direct consequences c_d are assumed to be higher. Therefore, the resulting conditional robustness index $I_{Rob}|D_i$ is lower for the double-column than for the single-column damage scenario D_i.

The aggregated robustness index I_{Rob} of the entire building is the sum of all the conditional robustness indices $I_{Rob}|D_i$ [7]. As a very rough estimation, it is assumed that the conditional robustness indices $I_{Rob}|D_i$ of other damage scenarios can be inferred from the damage scenarios D_i in Figure 1. Here, only the single-column damage scenarios D_i are considered. By assuming that the mean conditional robustness index $I_{Rob}|D_i$ of all the single-column damage scenarios D_i is the mean of the conditional robustness indices $I_{Rob}|D_i$, the aggregated robustness index can be determined from $I_{Rob}=\Sigma_i(I_{Rob}|D_i)$. From this, the aggregated robustness index I_{Rob} is in the range between 0.021 and 0.026 for single-column damage scenarios D_i.

Figure 2b and Figure 2d show the sensitivity analysis on the total costs c_t for a collapsed floor area A_c of 500 m^2. With the probabilistic distribution parameters in Table 1, the mean of the total consequences c_t per 500 m^2 was 26 503 kCHF, with a lower 5-percentile of 11 924 kCHF and an upper 95-percentile of 51 179 kCHF. The range of the 90% confidence interval is very large with a coefficient of variation *cov* of 48.3% and can be attributed to the large uncertainties of the number of fatalities n_f. This is also clear from Figure 2d, which shows that the most important parameter is the number of fatalities n_f followed by the *SWTP*. The Sobol indices S_i^T in Figure 2d also supports that the material consequences stemming from the construction costs c_c and the direct consequences c_d attributed to the initial damage scenario D_i are insignificant compared to the societal consequences c_s. Therefore, the total consequences c_t can be estimated from the societal consequences c_s alone.

5. CONCLUSION

In this paper, the robustness of a five-storey timber frame was assessed by subjecting it to single- and multi-column damage scenarios. To assess its robustness and the total costs attributed to the damage scenarios, a state-of-the-art modelling framework for simulating the progressive collapse of timber buildings was used. The modelling framework was used to determine the final collapsed state of the buildings to infer the collapsed floor area. In addition, the societal willingness-to-pay based on the life quality index and an empirical model for estimating the number of fatalities were used to quantify the societal consequences attributed

to the loss of life. To quantify the uncertainties of the societal willingness-to-pay and the total consequences, sensitivity analyses were conducted.

The results from the progressive collapse simulations showed that the building was unable to develop catenary action and that the collapse duration could infer the extent of damage. The 90% confidence interval of the societal willingness-to-pay in 2022 was between 6 860 and 10 033 kCHF and is reasonable when compared with other literature for Switzerland. The most important parameter for the societal willingness-to-pay was the work-leisure balance. For the total consequences of the various damage scenarios, it was shown that the direct and indirect material consequences were inconsequential in comparison with the societal consequences, which could be used directly to estimate the total consequences. The most important parameter for the total consequences was the number of fatalities.

Further research is needed to reduce the uncertainties related to the total consequences and to expand the results to a wider geographical area. Future analyses should include the assessment of more damage scenarios, which should be appropriate surrogates of plausible hazards. The modelling framework for progressive collapse should be improved upon to include a larger variety of connections and building materials. This may enable the quantification of the robustness of timber buildings and other buildings using a risk-based approach, which may pave the way for cost-efficient robustness guidelines for practice.

ACKNOWLEDGEMENTS

This article has been written in the framework of the project *Robustness of tall timber buildings* at ETH Zurich. The project is funded by the Albert-Lück Stiftung, and the authors are grateful for their financial support. The authors would like to thank Aurélien Clerc and former master students Lukas Esser, Ben Glarner, Lukas Esser, and Silvan Ullmann for their contributions.

REFERENCES

[1] Newman R, Noy I. The global costs of extreme weather that are attributable to climate change. Nat Commun 2023;14. https://doi.org/10.1038/s41467-023-41888-1.

[2] Global Terrorism Database 1970 - 2020. START (National Consortium for the Study of Terrorism and Responses to Terrorism) 2022. https://www.start.umd.edu/gtd (accessed March 14, 2024).

[3] Starossek U, Haberland M. Disproportionate Collapse: Terminology and Procedures. Journal of Performance of Constructed Facilities 2010;24:519–28. https://doi.org/10.1061/(asce)cf.1943-5509.0000138.

[4] Elkady N, Augusthus Nelson L, Weekes L, Makoond N, Buitrago M. Progressive collapse: Past, present, future and beyond. Structures 2024;62:106131. https://doi.org/10.1016/J.ISTRUC.2024.106131.

[5] Mpidi Bita H, Huber JAJ, Palma P, Tannert T. Prevention of Disproportionate Collapse for Multistory Mass Timber Buildings: Review of Current Practices and Recent Research. Journal of Structural Engineering 2022;148. https://doi.org/10.1061/(asce)st.1943-541x.0003377.

[6] Caredda G, Makoond N, Buitrago M, Sagaseta J, Chryssanthopoulos M, Adam JM. Learning from the progressive collapse of buildings. Developments in the Built Environment 2023;15:100194. https://doi.org/10.1016/J.DIBE.2023.100194.

[7] Baker JW, Schubert M, Faber MH. On the assessment of robustness. Structural Safety 2008;30:253–67. https://doi.org/10.1016/j.strusafe.2006.11.004.

[8] Voulpiotis K, Schär S, Frangi A. Quantifying robustness in tall timber buildings: A case study. Eng Struct 2022;265:114427. https://doi.org/10.1016/J.ENGSTRUCT.2022.114427.

[9] European Committee for Standardization. EN 1990:2002. Eurocode - Basis of structural design. Brussels, Belgium: 2002.

[10] European Committee for Standardization. EN 1995-1-1:2004. Eurocode 5: Design of timber structures - Part 1-1: General - Common rules and rules for buildings. Brussels, Belgium: 2004.

[11] European Committee for Standardization. EN 1991-1-4:2005. Eurocode 1: Actions on structures - Part 1-4: General actions - Wind actions. Brussels, Belgium: 2005.

[12] International Organization for Standardization. ISO 10137:2007. Bases for design of structures - Serviceability of buildings and walkways against vibrations. Geneva, Switzerland: 2007.

[13] Cao AS, Esser L, Frangi A. Modelling progressive collapse of timber buildings. Structures 2024;62:106279. https://doi.org/10.1016/J.ISTRUC.2024.106279.

[14] Nathwani J, Lind N, Pandey M. Affordable Safety By Choice: The Life Quality Method. Waterloo, Ontario, Canada: Institute for Risk Research; 1997.

[15] Hingorani R, Tanner P, Prieto M, Lara C. Consequence classes and associated models for predicting loss of life in collapse of building structures. Structural Safety 2020;85:101910. https://doi.org/10.1016/J.STRUSAFE.2019.101910.

[16] Marelli S, Sudret B. UQLAB: a framework for Uncertainty Quantification in MATLAB. The 2nd International Conference on Vulnerability and Risk Analysis and Management (ICVRAM 2014), Liverpool, United Kingdom: American Society of Civil Engineers; 2014, p. 2554–63. https://doi.org/10.1061/9780784413609.257.

[17] Cao AS, Palma P, Frangi A. Column removal analyses of timber structures - Framework to assess dynamic amplification factors for simplified structural design methods. World Conference on Timber Engineering 2021, WCTE 2021, Santiago, Chile: 2021, p. 1717–24.

[18] Cao AS, Esser L, Glarner B, Frangi A. A nonlinear dynamic model for collapse investigations in tall timber buildings - Preliminary results. World Conference on Timber Engineering 2023, WCTE 2023, Oslo, Norway: 2023, p. 2268–77. https://doi.org/10.52202/069179-0301.

[19] Cao AS, Frangi A. Dynamic strength increase of glued laminated timber beams subjected to impact loading. In: Görlacher R, editor. International Network on Timber Engineering Research, INTER: Proceedings, Meeting 56, 21-24 August 2023, Biel, Switzerland, Karlsruhe, Germany: Timber Scientific Publishing, KIT Holzbau und Baukonstruktionen; 2023, p. 1–17.

[20] Cao AS, Houen M, Frangi A. Impact loading of glued laminated timber beams without finger-joints. Comput Struct 2024;296:107278. https://doi.org/10.1016/j.compstruc.2024.107278.

[21] Cao AS, Frangi A. The influence of damping on progressive collapse analysis. In: Papadrakakis M, Fragiadakis M, editors. 9th ECCOMAS Thematic Conference on

Computational Methods in Structural Dynamics and Earthquake Engineering (COMPDYN 2023), Athens: 2023, p. 1–16. https://doi.org/10.3929/ethz-b-000619272.

[22] Cao AS, Palma P, Frangi A. Multi-scale hysteretic model of laterally loaded timber connections with dowel-type fasteners. In: Silva Gomes JF, editor. 20th International Conference on Experimental Mechanics (ICEM20), Porto, Portugal: INEGI-FEUP; 2023, p. 915–26. https://doi.org/10.3929/ethz-b-000619274.

[23] McKenna F, Scott MH, Fenves GL. Nonlinear Finite-Element Analysis Software Architecture Using Object Composition. Journal of Computing in Civil Engineering 2010;24:95–107. https://doi.org/10.1061/(asce)cp.1943-5487.0000002.

[24] Havik K, Mc Morrow K, Orlandi F, Planas C, Raciborski R, Röger W, et al. The Production Function Methodology for Calculating Potential Growth Rates & Output Gaps. Brussels, Belgium: 2014. https://doi.org/10.2765/71437.

[25] Pandey MD, Nathwani JS, Lind NC. The derivation and calibration of the life-quality index (LQI) from economic principles. Structural Safety 2006;28:341–60. https://doi.org/10.1016/J.STRUSAFE.2005.10.001.

[26] Rackwitz R. The effect of discounting, different mortality reduction schemes and predictive cohort life tables on risk acceptability criteria. Reliab Eng Syst Saf 2006;91:469–84. https://doi.org/10.1016/J.RESS.2005.03.015.

[27] Fischer K, Virguez E, Sánchez-Silva M, Faber MH. On the assessment of marginal life saving costs for risk acceptance criteria. Structural Safety 2013;44:37–46. https://doi.org/10.1016/J.STRUSAFE.2013.05.001.

[28] European Committee for Standardization. EN 14080:2013 Timber structures - Glued laminated timber and glued solid timber - Requirements. Brussels, Belgium: 2013.

[29] Schilling S, Palma P, Steiger R, Frangi A. Probabilistic description of the mechanical properties of glued laminated timber made from softwood. In: Görlacher R, editor. International Network on Timber Engineering Research, INTER: Proceedings, Meeting 54, 16-19 August 2021, Online, Timber Scientific Publishing, KIT Holzbau und Baukonstruktionen; 2021, p. 1–16.

[30] Lignum - Holzwirtschaft Schweiz. Was kostet ein Holzbau? Zurich, Switzerland: 2021.

[31] Sudret B. Global sensitivity analysis using polynomial chaos expansions. Reliab Eng Syst Saf 2008;93:964–79. https://doi.org/10.1016/j.ress.2007.04.002.

[32] Cao AS, Grönquist P, Frangi A. Catenary action in strip-reinforced wood and timber beams. Constr Build Mater 2023. https://doi.org/10.1016/j.conbuildmat.2023.131422.

[33] Hürzeler C, Leuba J, Balmer M. Externe Kosten und Nutzen des Verkehrs in der Schweiz. Bern, Switzerland: 2023.

[34] OECD. Mortality Risk Valuation in Environment, Health and Transport Policies. 2012. https://doi.org/10.1787/10.1787/9789264130807-en.

[35] Schweizerische Ingenieur- und Architektverein. SIA 269:2011. Grundlagen der Erhaltung von Tragwerken. Zurich, Switzerland: 2011.

[36] Schweizerische Ingenieur- und Architektverein. SIA 269/8:2017. Erhaltung von Tragwerken - Erdbeben. Zurich, Switzerland: 2017.

[37] Kägi W, Lobsiger M, Liechti D, Neumann R, Schläpfer F, Rheinberger C, et al. Monetary valuation of a statistical life in road traffic. 2015.

[38] Fischer K. Societal decision-making for optimal fire safety. Doctoral thesis. ETH Zurich, 2014.

[39] Schweizerische Bundesamt für Statistik. Ständige Wohnbevölkerung nach Geschlecht und Altersklasse, definitive Jahresergebnisse, 2015-2022. Bestand Und Entwicklung Der Bevölkerung Der Schweiz Im Jahr 2022: Definitive Ergebnisse 2023. https://www.bfs.admin.ch/bfs/de/home/statistiken/kataloge-datenbanken.assetdetail.26565274.html (accessed March 6, 2024).

[40] World Health Organisation (WHO). Life tables by country - Switzerland. Global Health Observatory Data Repository n.d. https://apps.who.int/gho/data/view.main.LT62230?lang=en (accessed March 6, 2024).

[41] Hermelink AH, De Jager D. Evaluating our future-The crucial role of discount rates in European Commission energy system modelling. Stockholm, Sweden: 2015. https://doi.org/10.13140/RG.2.2.20152.65285.

[42] Schäublin JJ. Swiss pension funds: funding ratio, discount rate, and asset allocation. Swiss J Econ Stat 2022;158. https://doi.org/10.1186/s41937-022-00092-6.

[43] Schweizerische Bundesamt für Statistik. Bruttoinlandprodukt pro Kopf. Volkswirtschaftliche Gesamtrechnung Der Schweiz Im Jahr 2022 2023. https://www.bfs.admin.ch/bfs/de/home/statistiken/volkswirtschaft.assetdetail.27065029.html (accessed March 6, 2024).

[44] OECD. Average annual hours actually worked per worker 2023. https://stats.oecd.org/index.aspx?DataSetCode=ANHRS (accessed March 6, 2024).

[45] Schweizerische Bundesamt für Statistik. Erwerbstätige Pendler/innen (Arbeitspendler/innen) nach Länge und Zeitbedarf für den Arbeitsweg. Pendlermobilität Im Jahr 2022 2024. https://www.bfs.admin.ch/bfs/de/home/statistiken/mobilitaet-verkehr/personenverkehr/pendlermobilitaet.assetdetail.30148656.html (accessed March 6, 2024).

[46] Schweizerische Bundesamt für Statistik. Lebenserwartung, 2000-2022. Demographische Indikatoren Im Jahr 2022 2023. https://www.bfs.admin.ch/bfs/de/home/statistiken/bevoelkerung/geburten-todesfaelle/lebenserwartung.assetdetail.27225455.html (accessed March 6, 2024).

[47] Schweizerische Bundesamt für Statistik. Durchschnittliches Alter beim Austritt aus dem Arbeitsmarkt nach Geschlecht und Erwerbsstatus. Schweizerische Arbeitskräfteerhebung Im 4 Quartal 2022: Arbeitsangebot 2023. https://www.bfs.admin.ch/bfs/de/home/statistiken/arbeit-erwerb/erwerbstaetigkeit-arbeitszeit/alter-generationen-pensionierung-gesundheit/erwerbstaetigkeit-pensionierung.assetdetail.24186245.html (accessed March 6, 2024).

[48] OECD. Pensions at a glance: Country profiles - Switzerland. 2023.

[49] United Nations Department of Economic and Social Affairs. Labour share of GDP, comprising wages and social protection transfers, %. Statistics, SDG Indicators Database n.d. https://unstats.un.org/sdgs/dataportal/countryprofiles/che (accessed March 6, 2024).

EXPERIMENTAL STUDY ON PROGRESSIVE COLLAPSE BEHAVIOR FOR BEAM-COLUMN SUBSTRUCTURE OF MODULAR STEEL BUILDING

Yumei Zhang[1], Junshan Liu[2], Bo Yang[3] and Kang Chen[4]

[1] Ph.D. Candidate, School of Civil Engineering, Chongqing University, 83 Shabeijie, Chongqing, China, 400045. Email: Yumei__Zhang@163.com.

[2] Postgraduate student, School of Civil Engineering, Chongqing University, 83 Shabeijie, Chongqing, China, 400045. Email: ljs_449161866@163.com.

[3] Professor, School of Civil Engineering, Chongqing University, 83 Shabeijie, Chongqing, China, 400045, Email: yang0206@cqu.edu.cn.

[4] Assistant Professor, Dept. of Civil Engineering, Xi'an Jiaotong-Liverpool University, 111 Ren'ai Road, Suzhou Industrial Park, Suzhou, Jiangsu, China, 215123. Email: kang.chen@xjtlu.edu.cn

Corresponding Author: Bo Yang, Professor.

School of Civil Engineering, Chongqing University, 83 Shabeijie, Chongqing, China, 400045

Email: yang0206@cqu.edu.cn

ABSTRACT

Modular building, referred to prefabricate room units in factory and then transport to site for installation in a Lego-like manner, is an innovative and game-changing technology in building industry. That is exactly what is known as the Prefabricated Prefinished Volumetric Construction (PPVC) in Singapore. Modular steel building (MSB) offers many advantages of especially high industrialization, green energy-saving and being environmental-friendly. However, unlike the conventional onsite building structures, the resisting progressive collapse behavior under extreme events for MSB should be paid special attention due to its discontinuity in the structural frame and diaphragms. This paper focuses on the progressive collapse behavior of the MSB beam-column substructure. First a typical bolt connection with cover plate for interior joint, mentioned in historical literature, has been considered to conduct experimental study. An appropriate experimental method was developed to perform a vertical loading test in order to explore the failure modes and mechanisms of resisting progressive collapse under an interior cluster-column loss scenario. The test results, including failure modes/sequence, load–deformation responses and strain development, are reported in detail, and a thorough analysis of the load transfer mechanism over the entire loading process is conducted.

Keywords: *Modular steel building (MSB), Beam-column substructure, Progressive collapse behavior, Experimental study, Resistance mechanism.*

1. INTRODUCTION

Modular building, referred to prefabricate room units in factory and then transport to site for installation in a Lego-like manner, is an innovative and game-changing technology in building industry [1]. That is exactly the Prefabricated Prefinished Volumetric Construction (PPVC) in Singapore [2]. It has gained popularity due to its significant advantages of high speed of construction and quality control. The inherent high strength-to-weight ratio and simpler connecting characteristics of steel makes it the preferred choice for modular structures. Modular steel building (MSB) can maximize the level of building assembly and construction efficiency, offering advantages of especially green energy-saving and being environmental-friendly, which even probably to be more economical than precast concrete structures.

Over the last 20 years, several countries have constructed many low- and high-rise MSB engineering applications [3,4], such as hotels, apartments, residences and offices. However, the literature indicates that research on this new building structure still lags behind. In the limited researches, structural systems, connections, seismic and wind behavior attract more attention, whereas little research has been done on collapse behavior under extreme loading scenario. Ensuring the safety of the structure is always the most fundamental and crucial task, as if a collapse happened, it certainly will cause serious loss of life and economy. As depicted in Fig.1(a), adjacent module units are connected at corners to allow multiple module units form an overall structure of a certain scale. Consequently, MSB structures possess essential differences from the conventional steel frame structures, making them have poor overall integrity and be more prone to collapse under extreme events. Therefore, special attention should be paid to the resistance against progressive collapse of MSB.

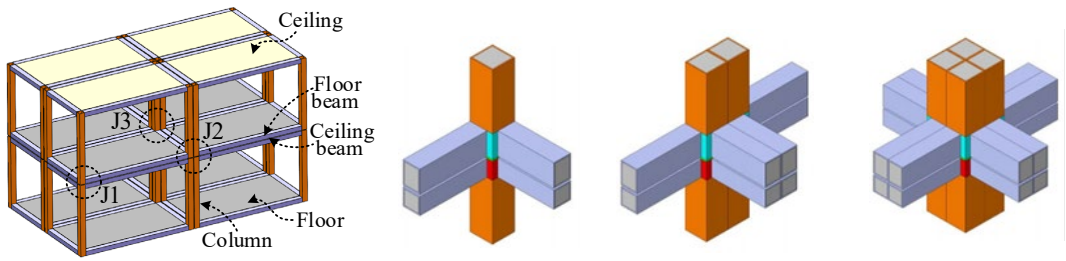

(a) Inter-modular connections (b) J1-corner joint (c) J2-side joint (d) J3-interior joint

Figure 1. The composition of corner supported MSB structure.

Previous studies on the progressive collapse behavior of conventional steel frame structures [5,6,7] have demonstrated that the beam-column substructure plays a significant role in transmitting forces for residual structures, and joints often determine the ultimate failure mode and ultimate capacity of structures. However, MSB structures involve multi-column and double-beam at the joints (see in Fig.1(b-d)), introducing more components, which could make the load transfer mechanism more complicated. Existing conclusions drawn from studies on beam-column substructures of steel frames may not be directly applicable to MSB structures. Therefore, it is extremely necessary to carry out specialized studies on progressive collapse behavior of the beam-column substructure for MSB.

A typical connection for interior joint was selected from the literature, then an experimental test

on MSB beam-column substructure under the interior cluster-column loss scenario was conducted based on the alternate load path (ALP) method. The resisting progressive collapse response and the resistance mechanism are highly concerned in this study.

2. TEST PROGRAMME

2.1 Test specimen

Based on the inflection point assumption, a half-span length beam-column substructure at the interior joint was extracted from the prototype structure under the scenario of interior cluster-column loss at the first floor, as illustrated in Fig.2(b). This substructure connects eight columns and sixteen beams together at the joint. For the collapse resistance analysis, merely the beam-column substructure in the short span direction (Y-direction) with greater stiffness as well as force, was considered to simplify the test. Due to its high symmetry, the substructure can be further simplified, as shown in Fig. 2(d), for experimental test.

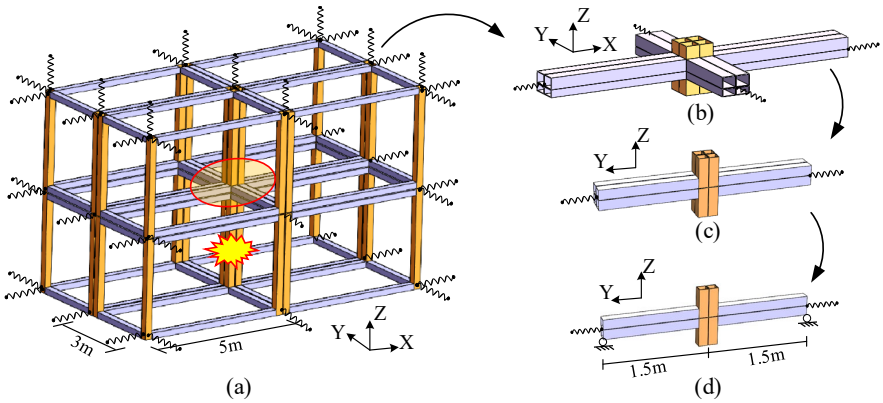

Figure 2. Test beam-column substructure extracted from prototype structure.

Hollow steel sections are commonly used for the module columns and beams due to their efficiency in compression and torsion. The column and beam sections listed in Table 1 are the most economical sections that can meet the design load as determined through structural design analysis using MIDAS/GEN. The connection proposed by Xiang [8] was adopted, as shown in Fig.3, which is a typical type of connection -- bolt connection with cover plate. Several similar connections for MSB can be found in Refs. [9,10,11]. The test specimen comprised columns, floor beams, ceiling beams, bolts, cover plates, and connecting plate. The connections of beams to columns and the hollow sections to cover plates were welded. The detailed dimensions of the other elements were determined by the component sections, and the most unfavorable internal force of a joint calculated by MIDAS/GEN.

Table 1. Section information and material properties.

Component	Material	Section size / [mm]	Young's modulus / [Gpa]	Yield strength / [Mpa]	Ultimate strength / [Mpa]
Modular column	Q355B	160×160×6	199.4	432.6	562.7
Floor beam	Q355B	180×100×6	195.0	415.7	537.0
Ceiling beam	Q355B	100×100×6	202.7	502.8	558.2

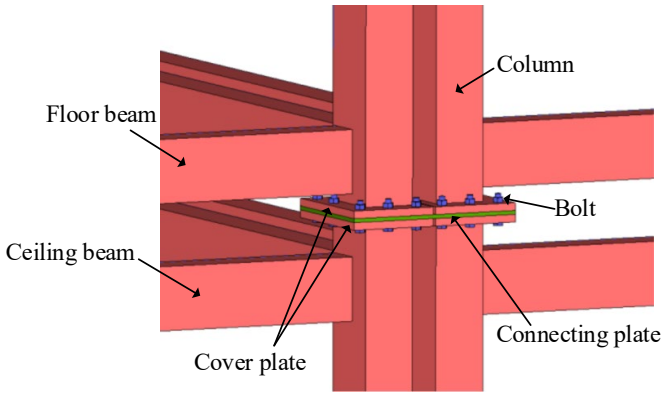

Figure 3. The bolt connection with cover plate [8].

2.2 Loading program and measurement

The test was conducted at the Structural Laboratory of Chongqing University, and the specimen loading configuration is depicted in Fig. 4. In this test, the specimen was inverted, and it was loaded by the jack fixed on the strong floor with a push-up method. There was no connection between the loading beam and column-end. The double-beam was connected to the hinge end through rollers. It corresponds to the boundary condition of inflection point, and allows the independent rotation of the floor beams and ceiling beams. An additional lateral support system, composed by four steel columns and pulleys, was arranged on both sides of the specimen to prevent any out-of-plane deflection during loading. Those pulleys were fixed on the double-beam of the specimen, enabling smooth sliding on the steel column without affecting the up-/down-ward movement of the specimen. The measurement scheme and corresponding labels are shown in Fig. 5. The strain gauges were labeled as FB/CB-W1/W2/E1/E2-1/2/3/4/5/6, where the FB represents the floor beam and CB represents the ceiling beam, W1/W2/E1/E2 denote the specified section, and 1/2/3/4/5/6 correspond the positions shown in Fig. 5.

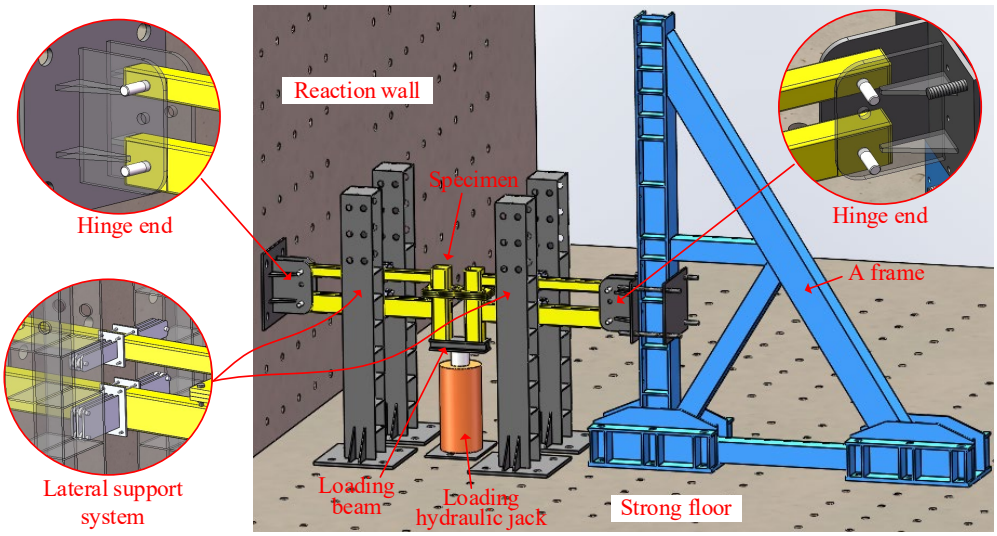

Figure 4. Test setup.

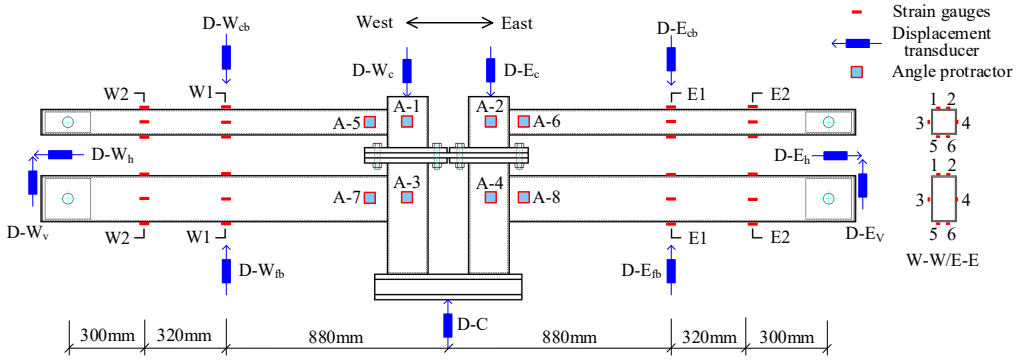

Figure 5. Overall layout of instrumentation.

3. EXPERIMENTAL RESULTS AND ANALYSIS

3.1 General behavior and failure mode

Fig. 6 exhibits the failure mode of the specimen after loading, with cracks appearing in the area of all beam-column connections but not in the weld seams, and the rest of the specimen remained intact. The relationship of applied force (F) and vertical displacement of jack measured from D-C (Δ) is plotted in Fig. 7, where marks the damage phenomena associated to the critical points during the test. The red Roman numerals on these figures represent the sequence of cracking. It can be observed that the connections of floor beam-column were damaged first, resulting in two abrupt drops in load, but the specimen did not lose its carrying capacity. Subsequently, the load recovered and continued to rise until the connections of ceiling beam-column cracked, causing another two sharp drops in load again. The test was then terminated with the load exceeding the prior peak load eventually.

Four photographs corresponding to the positions a, b, c, and d in F-Δ curve are displayed in Fig. 8 to show the general deformation pattern of the specimen. It can be observed that all the columns rotated from the beginning due to each column was subjected to force unilaterally. However, the loading columns had a slight recovery while the removal columns rotated more after the cracking of floor beam-column connections. Additionally, the connecting plate displayed noticeable in-plane bending deformation.

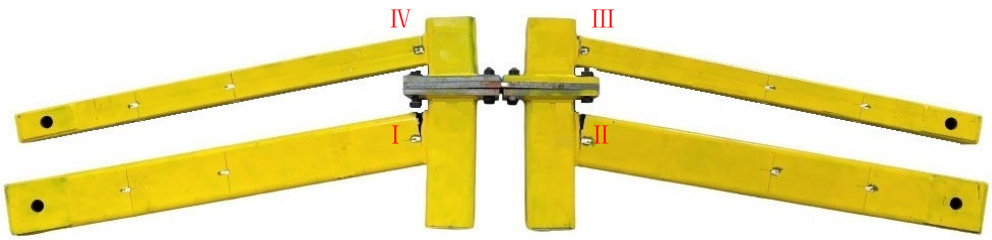

Figure 6. Failure mode.

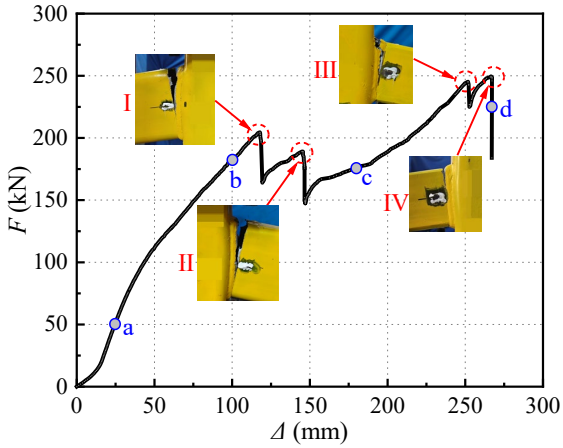

Figure 7. Load-displacement relationship.

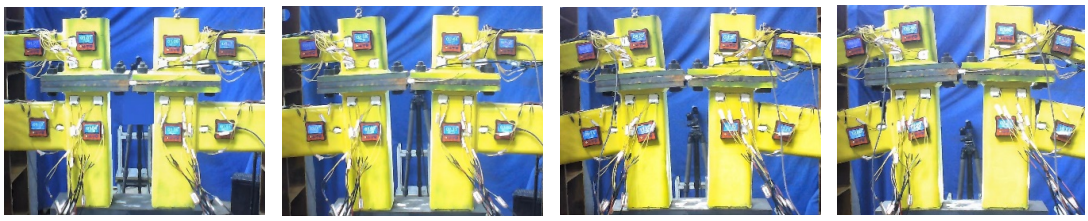

a. b. c. d.

Figure 8. Specimen general deformation pattern.

3.2 Displacement

Fig. 9 presents the displacement profiles of the specimen at different Δ, revealing that the whole specimen deflected like simply-supported beams. The displacement profile of both ceiling beams and floor beams exhibited a typical flexural pattern, approximated by straight lines. In the early stage (Δ=50mm), the deflection of ceiling beams and floor beams completely overlapped and vertical displacements of removal columns (i.e., D-W_C / D-E_C) are consistent with that of loading columns (i.e., D-C). As the deflection increased, the deviations in the deflection of ceiling beams and floor beams became apparent, and the displacements of D-W_C and D-E_C were gradually smaller than that of D-C due to the column rotations. Fig. 10 illustrates that the significant deviation in double-beam deflection resulted from the fracture of floor beam-column connection, which also indicates that the double-beam always deforms in concert.

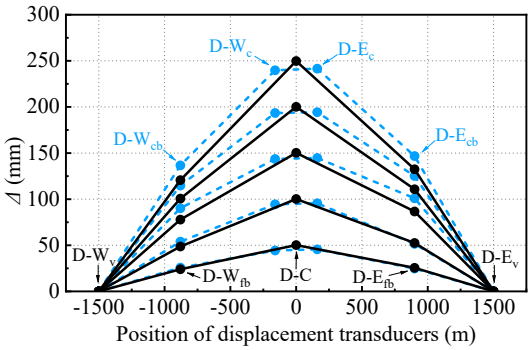

Figure 9. Deflection shape.

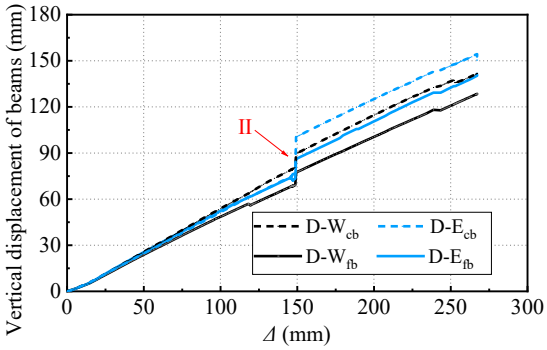

Figure 10. Deflection of double-beam.

3.3 Strain

The strain development of double-beam at different *F*, measured form section W2, is presented in Fig.11, which shows that the strain distribution of the double-beam was discontinuous and the neutral axes of the two beams were located at their own centroid axes of cross-section, respectively. Therefore, there was almost no composite effect and the beams resisted load independently. The strain distribution of both beams exhibited bending characteristics with upper in tension and lower in compression. However, the positions of neutral axes moved constantly, which indicated that in addition to bending, the beams were also subjected to axial tension/compression. The axial force development of beams, converted from the strain measurements of section W2 and E2, is plotted in Fig. 12. It can be noticed that the floor beams initially developed tension, and the tensile forces decreased a lot and then stabilized after the floor beam-column connections cracked. In contrast, the ceiling beams underwent compression initially until the floor beam-column connections cracked, after which the internal forces of ceiling beams rapidly transformed from compression to tension. Since then, the tension forces of ceiling beams grew up until two drops at the moments of ceiling beam-column connections cracking.

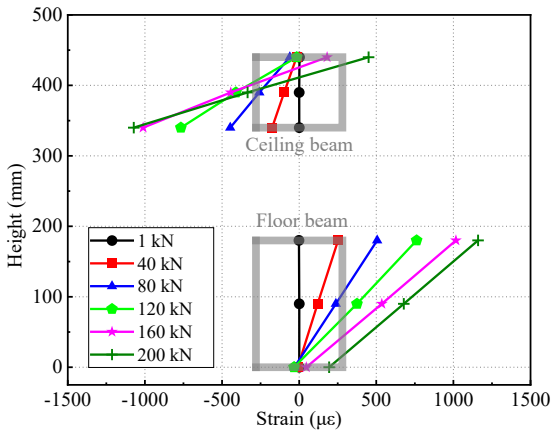

Figure 11. Strain development of double-beam.

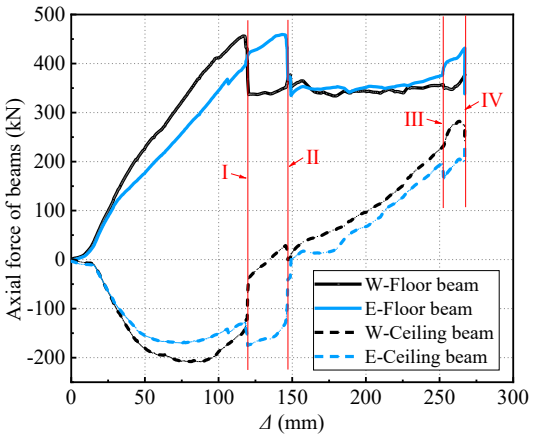

Figure 12. Axial force development of beams.

3.4 Development of resistance mechanism

As discussed above, it can be considered to superimpose the internal force of each beam directly since there was almost no composite effect. As a result, the load resisted by catenary action (CA) can be obtained by superimposing the vertical components of the axial forces of the four beams, and the residual load can be considered to be resisted by flexural action (FA). The resistance mechanism development of specimen is presented in Fig. 13, from which there are four distinctive stages: flexure-dominated stage (before I), flexure catenary transitional stage (I~II), catenary-dominated stage (II~III), and full-catenary stage (III~IV). The FA resistance significantly decreased after the cracking of the west and east side floor beam-column connections. The moment approaching the cracking of the east side ceiling beam-column connection may be regarded as an absolute ultimate limit state of the specimen in a flexural condition. Afterwards, the load resisted by FA decreased to be negative, indicating that the FA started to play a negative role in the vertical resistance. Combination with Fig. 12, it can be

found that the main reason for load rising in the later period was the development of CA in the ceiling beams.

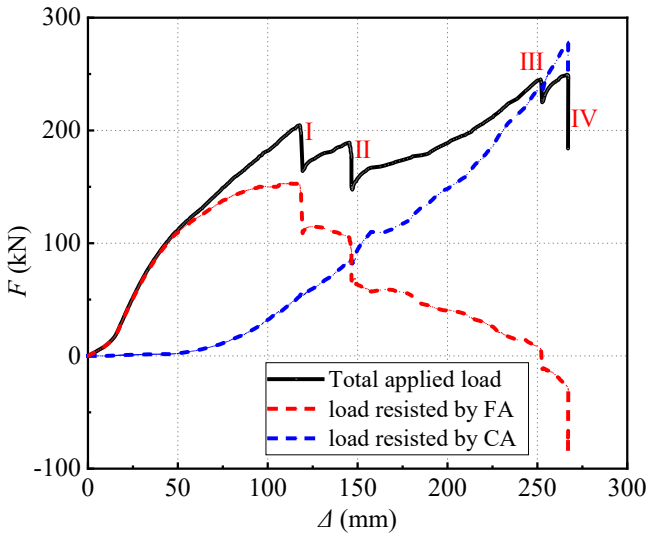

Figure 13. Resistance mechanism development of specimen.

4. CONCLUSIONS

This paper conducted an experimental study on MSB beam-column substructure using bolt connection with cover plate, under the scenario of interior cluster-column loss. The main conclusions can be drawn as follows:

(1) The test results demonstrated that during the process of resisting vertical load, the floor beam-column connections of specimen failed first, while the ceiling beam-column connections can continue to carry load and eventually exceeded the prior peak load. It indicates that the specimen owns a relative high redundancy that allowing multiple beam-column connections to fail without loss of its carrying capacity.

(2) In this specimen, the strain distribution of double-beam was discontinuous, hence there was almost no composite effect and each beam resisted load independently. Furthermore, the double-beam always deforms in concert.

(3) The development of internal force in the beams indicates that the ceiling beams were subjected to significant compression at first, which cannot be ignored. This is quite different from the conventional steel beam-column substructure. It may remind the engineering designers to pay attention not only to the tension of floor beams but also to the compression of ceiling beams, to avoid the MSB failure or even collapse due to insufficient compressive capacity of the ceiling beams.

(4) The resistance of the specimen was dominated by the flexural mechanism in the early stage, and the beam catenary mechanism in the later stage. In this case, the flexural resistance was primarily contributed by the floor beams, and a supply of catenary action from the ceiling beams can be regarded as a second defense.

REFERENCES

[1] Lawson, R.M., Ogden, R., & Goodier, C. (2014). Design in Modular Construction. CRC Press, Boca Raton, FL, USA.

[2] Pang, S.D., Liew, J.Y.R., Dai, Z., & Wang, Y. (2016). Prefabricated prefinished volumetric construction joining techniques review. Modular and Offsite Construction (MOC) Summit Proceedings (pp. 249-256). Edmonton, Alberta, Canada.

[3] Hough, M.J., & Lawson, R.M. (2019). Design and construction of high-rise modular buildings based on recent projects. Proceedings of the institution of civil engineers - civil engineering, 172(6), 37-44.

[4] Gunawardena, T., & Mendis, P. (2020). Steel modular construction and its applicability to the building industry in China. Steel construction (Chinese & English), 35(2), 66-73.

[5] Yang, B., & Tan, K.H. (2013). Experimental tests of different types of bolted steel beam–column joints under a central-column-removal scenario. Engineering Structures, 54, 112-130.

[6] Wang, W., Fang, C., Qin, X., Chen, Y., & Li, L. (2016). Performance of practical beam-to-SHS column connections against progressive collapse. Engineering Structures, 106, 332-347.

[7] Lin, S., Qiao, H., Wang, J., Shi, J., & Chen, Y. (2021). Anti-collapse performance of steel frames with RWS connections under a column removal scenario. Engineering Structures, 227, 111495.

[8] Xiang P. (2017). Experimental research on joint of fabricated modular buildings (Master thesis). Harbin Institute of Technology, Harbin, China.

[9] Gunawardena, T., Ngo, T., Mendis, P., & Alfano, J. (2016). Innovative flexible structural system using prefabricated modules. Journal of Architectural Engineering, 22(4), 05016003.

[10] Lacey, A.W., Chen, W., Hao, H., & Bi, K. (2019). New interlocking inter-module connection for modular steel buildings: Experimental and numerical studies. Engineering Structures, 198, 109465.

[11] Sendanayake, S.V., Thambiratnam, D.P., Perera, N.J., Chan, T.H.T., & Aghdamy, S. (2021). Enhancing the lateral performance of modular buildings through innovative inter-modular connections. Structures, 29, 167-184.

PERFORMANCE AND MECHANISM OF PRESTRESSED FABRICATED CONCRETE FRAME TO RESIST PROGRESSIVE COLLAPSE WITH A SIDE COLUMN FAILURE

Manrong SONG[1,2], Xiaolong CHEN[1,2], Jiaxuan HE[3,2], Jingfeng WANG[1,2], Ruixue CAO[4], Yuwei JIN[1,2], Shenjiang HUANG[1,2], Bingkang LIU[1,2].

[1] College of Civil Engineering, Hefei University of Technology, Hefei, 230009, China.

[2] Anhui Key Laboratory of Civil Engineering Structure and Materials, Hefei, 230009, China.

[3] School of Civil Engineering, Southeast University, Nanjing, 211189, China.

[4] The Construction Engineering Company of CTCE Group, Hefei, 230022, China.

Corresponding Author: Manrong SONG, PhD, Associate Professor.

Hefei, Anhui, China, 230009

Email: songmanrong@hfut.edu.cn

ABSTRACT

In order to explore the crack development, deformation capacity, failure mode and progressive collapse mechanism of the frame under the failure of the bottom side column, a progressive collapse test and theoretical analysis were conducted on a two-story two-span precast prestressed concrete frame. The results show that the structural loading stages include the beam mechanism stage and the collapse stage during the failure of the side column. In the small deformation stage, the structure follows the beam mechanism and exhibits compression arch effect and vierendeel action. In the large deformation collapse stage, the structure does not follow the catenary mechanism and the unbalanced load can be resisted by the bending mechanism and vierendeel action. Concrete cracking and failure were concentrated at the beam-column nodes on both sides of the frame beams adjacent to the failed side column, and the damage to the beam-column nodes of the bottom frame was more serious. The other columns and the beams away from the failed columns were basically intact. Then according to the control section of structural failure and the critical collapse state of the specimen, the computation methods of the collapse resistance and the critical displacement were proposed, respectively.

Keywords: *Precast Prestressed Concrete Frame, Progressive Collapse, Side Column Removal, Experimental Investigation, Theoretical Analysis.*

1 INTRODUCTION

Progressive collapse is defined as the spread of an initial local failure from element to element, eventually resulting in the collapse of an entire structure or a disproportionately large part of it [1]. The collapse accident of Ronan Point apartment caused by a gas explosion accident in the United Kingdom in 1968 first attracted international attention to the problem of progressive collapse [2]. The collapse of the Murrah Federal Building in the United States in 1995 [3] and the World Trade Center in New York in 2001 [4] brought the study of structural progressive collapse to a climax. To prevent such disasters, scholars at home and abroad have done a lot of work in experimental research, numerical analysis, and theoretical research for different types of construction and have obtained abundant achievements.

Sasani and Sagiroglu [5] studied the progressive collapse of RC frame structures, which were mainly designed based on different levels of wind and seismic loads. The results indicated that the vulnerability of frame structures to progressive collapses caused by artificial disasters depends largely on their resistance to natural disasters. Adam et al. [6] conducted a test on a full-scale, two-story, two-span RC frame with a specially designed corner steel column used for sudden column removal. The results indicated that the load initially carried by the removed column was redistributed to the entire building system through flexural and vierendeel action. Orton et al. [7] conducted a collapse test on a one-quarter scale, 2-bay, 2-story RC frame under a middle-column-removal scenario and found that the catenary action (CA) occurred in the beam when the load was 42% of the design value. Pham et al. [8,9] confirmed that distributed loading tests showed less development of CA against progressive collapse through the collapse experiments of beam-column substructures under concentrated loads and distributed loads. Qian et al. [10] carried out a quasi-static pushdown test on the beam-column substructures with different forms of reinforcement, and the results identified that using anti-seismic reinforcement can significantly improve the progressive collapse resistance of RC frame structures. Yi et al. [11] performed a progressive collapse test of a three-story, four-span reinforced concrete plane frame. Li et al. [12] proved that calculating progressive collapse resistance demand under the catenary mechanism is the key to designing progressive collapse resistance of RC frame structures in the large deformation stage.

Scholars have conducted much experimental research and theoretical analysis on PC frames with different connection methods. Nimse et al. [13] studied the progressive collapse performance of three different one-third scaled wet precast beam-column connections and found that load carrying capacity and ductility of precast connections are more than that of monolithic connections. Al-Salloum et al. [14] studied the progressive collapse performance of precast beam-column connections with bolted steel plates under a middle-column-loss scenario. The influence of different steel plate parameters on the test frame in the case of middle column loss was further analyzed. Ravasini et al. [15] used nonlinear dynamic finite element analysis method to study the progressive collapse resistance and

beam-column connection strength of precast concrete frame structures. Liu et al. [16,17] carried out experimental research on prefabricated concrete frames with different connection forms and analyzed the collapse resistance of prestressed splicing structures under wet connection and dry connection. Qian et al. [18,19] conducted a collapse test on the post-tensioned prestressed reinforced concrete beam-column substructure. It was found that the prestressed reinforcement provided a more significant suspension effect in the large deformation stage, which could significantly improve the ultimate bearing capacity of the frame and changed the failure mode of the specimen. Jin et al. [20] studied the progressive collapse resistance of post-tensioned unbonded prestressed beam-column substructures with two different steel strand arrangements after the failure of the middle column through experiments.

There are few studies involving prestress in the field of progressive collapse resistance of PC frame structures, and most of them were unbonded prestressed structures. The progressive collapse resistance of posttensioned bonded prestressed PC structures is insufficient. Compared with unbonded prestressed technology, the bending resistance, crack width, and ultimate strength of concrete structures with bonded prestressed technology are better than those of unbonded prestressed concrete structures. We proposed a prestressed fabricated PC structure with posttensioned bonded strands for connection. A number of seismic tests have been carried out, and the tests have shown good seismic performance. [21-24] In this paper, a static collapse experiment on a two-story, two-span prestressed fabricated concrete frame structure with a side-column-removal scenario was carried out, and the progressive collapse resistance is investigated by evaluating the crack development, damage mode, deformation performance, and resistance mechanism.

2 EXPERIMENT PROGRAM

2.1 Test specimen

To study the progressive collapse performance of the prestressed fabricated concrete frame under a side column failure, a specimen was designed as shown in **Fig. 1**. The specimen consisted of four identical notched beams, two complete columns with corbels, and one side column with the removed bottom layer. The specimen was designed in accordance with the Chinese code for the design of concrete structures [25] and for the Anti-collapse Design of Building Structures [26]. Due to the limited lab space, a factor of 1/2 was used to scale down geometry. As illustrated in **Fig. 1(a)**, The prestressed steel strand is tensioned at one end, and the tension control stress $\sigma_{con} = 0.75f_{pt}$. Rubber gaskets were used at the interface between posttensioned strands and beam-column nodes to avoid concrete crushing damage.

C40-grade concrete with an average compressive strength of 37.1 MPa, measured from the standard cube tests, was used to cast the specimen. The detailed diagram of reinforcement is shown in **Fig. 1(b)** to **Fig. 1(d)**. The prestressed tendons adopted low-relaxation steel strands. According to the standard[27], the mechanical tensile tests of steel strands and steel bars of various specifications were carried out. The results are shown in Table 1.

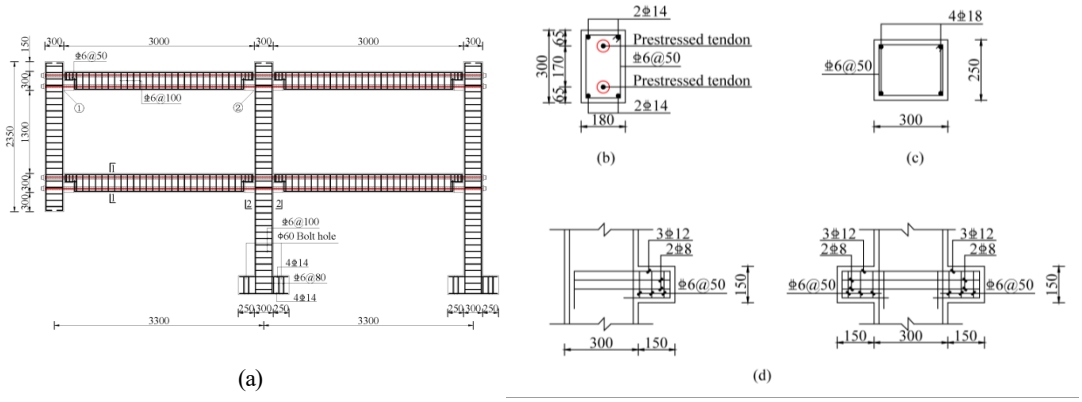

Fig. 1. Geometry and reinforcement detailing of the specimen (unit: mm): (a) The prestressed fabricated concrete frame; (b) section 1-1; (c) section 2-2; (d) local amplification.

Table 1. Material properties

Type	Nominal diameter (mm)	Yield strength (MPa)	Ultimate strength (MPa)	Elastic modulus (MPa)
C6	6	439.2	636.6	2.0×105
C8	8	461.7	622.7	2.0×105
C12	12	445.2	624.5	2.0×105
C14	14	487.1	617.1	2.0×105
C18	18	451.9	628.8	2.0×105
Strands	15.2	1833.3	1960	1.95×105

2.2 Test setup

Fig. 2 displays the test setup of the specimen. The column bottoms were fixed vertically to the solid floor by four high-strength anchor bolts, and then the screw thread steel and tool beam were fixed horizontally along the bottom of the specimen. A jack was installed under the failure column to recreate the column-removal scenario and prevent safety hazards caused by sudden collapse during subsequent loading. An axial pressure ratio of 0.3 was applied on the top of the middle column and the right-hand side column through the upper jacks. Four lateral constraints were specially made to provide the specimen with out-of-plane restraint to prevent potential out-of-plane failure. To simulate a sudden column removal, the jack under the damaged column was unloaded before loading. Exerting static load through the MTS actuator on the top of the failure column, until the specimen deformation exceeded 500 mm or a total collapse occurred, with incremental steps of 1mm, 2mm, 5mm, and 10mm.

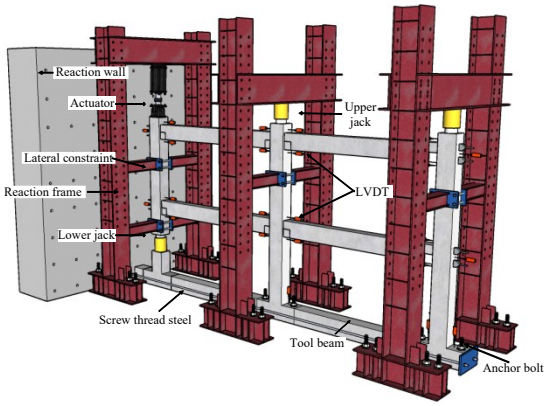

Fig. 2. Test setup.

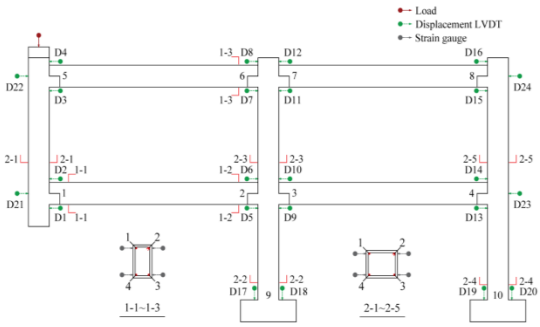

Fig. 3. Test measuring points layout.

2.3 Instrumentation

The layout of nodes and measuring points in the specimen is displayed in **Fig. 3**. 1-8 and 9-10 are the corresponding numbers of the beam ends and column feet, respectively. Strains of the rebars at the beam ends were measured by strain gauges arranged in the beam end sections of 1-1--1-3(1-1 to 1-3), and measurement points were placed 25 mm away from the beam ends at the nodes. Strains of the longitudinal rebars in columns were estimated by strain gauges set in sections 2-1--2-5(2-1 to 2-5). The interlayer displacement and beam-column rotation angle were gauged by linear variable displacement transducers (LVDTs) numbered D1-D24.

3 TEST RESULTS

3.1 General behavior and failure modes

The load-displacement curve, the failure mode of the test frame, and the damage patterns of the specimen are shown in **Fig. 4**, **Fig. 5**, and **Fig. 6**, respectively.

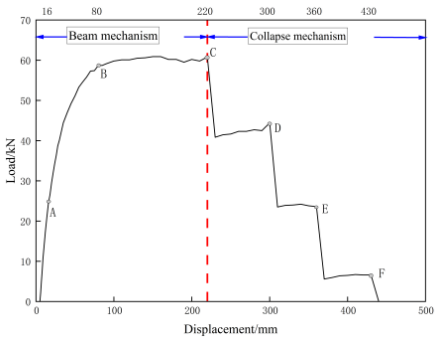

Fig. 4. Load-displacement curves.

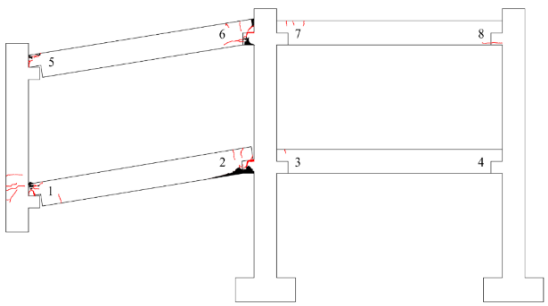

Fig. 5. Failure mode of the test frame

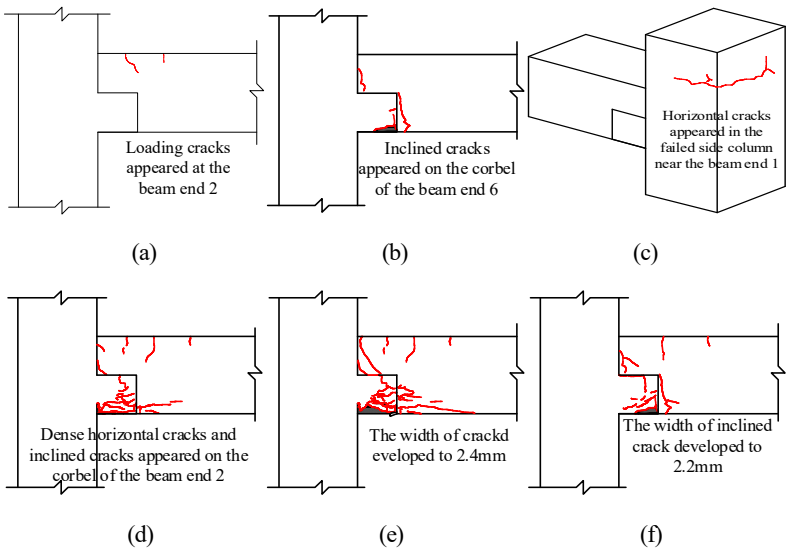

Fig. 6. Concrete cracks development: (a) The beam end 2 (16 mm); (b) the beam end 6 (24 mm); (c) the beam end 1(40 mm); (d) the beam end 2 (80 mm); (e) the beam end 2 (150 mm); (f) the beam end 6 (150 mm).

The OA segment of the load-displacement curve of the test varies roughly linearly, and no apparent cracks were observed, indicating that the specimen was in the elastic stage. When the displacement was loaded to 16 mm (A), the first crack appeared in the tension zone of the concrete at the top of the beam end 2, as described in **Fig. 6(a)**.

From A to B, the slope of the load-displacement curve of the test gradually decreased, the specimen was in the elastoplastic stage, and more cracks appeared at the beam end. Tensile cracks appeared at the top of beam end 6 when the displacement was increased to 20 mm; when loaded to 24 mm, the tensile crack at the top of beam end 6 extended further to 1/3 beam height, and a diagonal crack appeared in the tension zone of the corbel, as illustrated in **Fig. 6(b)**.

When the displacement was set to 40 mm, horizontal cracks appeared near the beam ends 1 and 5 sequentially due to the effect of compressive arch action (CAA), as shown in **Fig. 6(c)**. When the displacement was increased to 80 mm (B), the tensile crack of concrete at beam end 2 extended close to the center of the beam, and the tension zone of the corbel appeared to have dense horizontal cracks and oblique cracks, as depicted in **Fig. 6(d)**. The specimen entered the yield phase after point B.

When the displacement was placed to 150 mm, the width of the tensile crack at the beam end 2 increased to 2.4 mm, concrete spalling in the pressure zone, as illustrated in **Fig. 6(e)**. Besides, the width of the diagonal crack at the corbel of the beam end 6 developed to 2.2 mm, as shown in **Fig. 6(f)**. The concrete of the beam ends 2, 6, 5, and 1 successively reached the ultimate pressure strain, and the tensile prestressed tendons yielded. The specimen transitioned from the beam mechanism stage to the collapse stage when the displacement was applied to 220 mm (C). Concrete in the compression

zone of beam ends 2 and 6 was crushed, which caused the load to drop suddenly. The concrete at the beam ends 5 and 1 was crushed when the load was applied to 300 mm (D) and 360 mm (E), respectively. When the load was applied to 430 mm (F), the steel strand at the far end of the beam in the adjacent area of the failed column fractured, and the specimen lost its bearing capacity.

3.2 Lateral displacement of the specimen

Fig. 7 depicts the interlayer displacement and loading displacement curves. The horizontal displacement at the bottom layer of the specimen is illustrated in **Fig. 7(a)**. It can be observed that the horizontal displacement at the bottom layer of the right-hand side column (D23) was approximately zero, indicating that the collapse of the failed side column has less impact on the right-hand side column. The broken column was continuously pushed outward as the loading displacement grew because of the CAA. This is shown in **Fig. 7(a)** as the horizontal displacement (D21) increases towards a negative value. When the displacement was increased to 220 mm (C), the horizontal displacement at the bottom layer of the specimen reached a maximum of 2.86 mm, which was moved outward. After point C, the axial pressure in beams steadily dropped, the failed column shifted inward, and the specimen changed from the beam mechanism stage to the collapse stage. The horizontal displacement of the damaged column was essentially negligible at point E. After this point, the specimen continued to slide inward, revealing that the state of the beams shifted from the axial pressure to the axial tension.

Fig. 7(b) shows the interlayer displacement of the second layer of the specimen. The second layer of the failed column shifted inward when the loading displacement was small with the effect of vierendeel action. When the displacement was applied to 190 mm, the interlayer displacement reached the maximum extrapolated value of 2.12 mm. After that, the value increased in the positive direction, the specimen entered the adduction stage, and the second layer of the specimen reached a maximum adduction displacement of 3.1 mm near the point E.

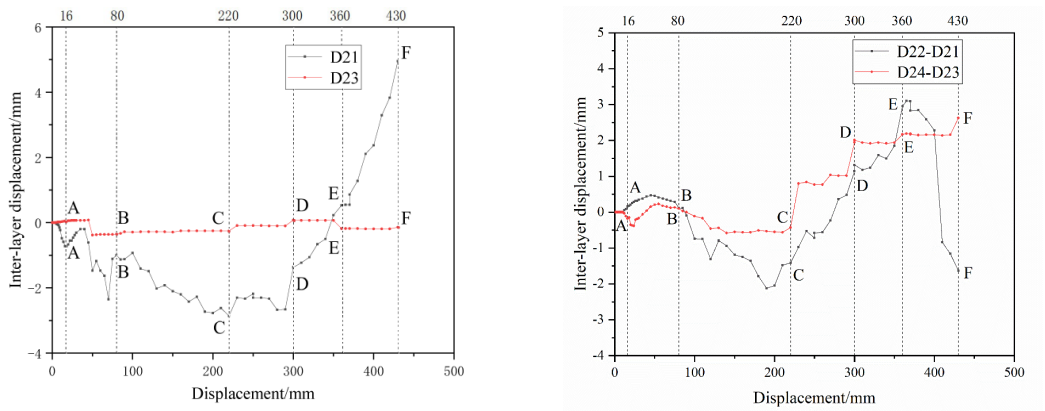

(a) (b)

Fig. 7. Interlayer displacement-vertical displacement curves: (a) The bottom layer; (b) the second layer.

3.3 Rebar stress

Fig. 8 shows the curves of the rebar stress at the beam end, and the vertical displacement with tension is positive and compression is negative. The rebar number is demonstrated in **Fig. 3**.

Fig. 8(a) depicts the rebar stress of section 1-1 at the beam end. At point B, a pull-off crack developed in the tensile zone of the beam end at the failed side column. As a result, the stress on the pull-off side of the tensile longitudinal rebar (1-1-3) stopped increasing, while the stress on the other side (1-1-4) continued to rise slowly, reaching a peak stress of 149 MPa. After point B, concrete in the compressive zone of beam end 1 reached the ultimate pressure strain, and the compressive longitudinal rebars (1-1-1, 1-1-2) reached a peak stress of 193 MPa. The stress of the longitudinal rebars at the beam end 1 was reduced to zero at point D (there was still tensile stress of the longitudinal rebar at the local adhesion side of the corbel surface in the tension area), indicating that it was in the critical state of full-section tension.

Fig. 8(b) depicts the rebar stress of section 1-2 at beam end 2. When the displacement was 35 mm, the turning point appeared at the curve, the tensile stress and compressive stress were 216 MP and 91 MP, respectively, and horizontal microcracks appeared at the bottom of the beam end 2. The tensile stress increased gradually, reaching a maximum of 285 MPa, yet the rebars did not yield due to the bonding between the beam end and the column. The longitudinal rebars at the beam end 2 were under tensile stress at point E, and the entire section was under tension.

The rebar stress of section 1-3 at the beam end is shown in **Fig. 8(c)**. The peak tensile stress and compressive stress of the rebars at the beam end 6 were 188 MPa and 140 MPa, respectively, when the damaged column displacement was 40 mm. The concrete at points C and D developed penetration cracks on both sides of the compression area, causing damage to the strain gauge of the compression longitudinal rebar 1-3-3, 1-3-4, and abnormal behavior to be visible. Up to point F, the longitudinal rebars 1-3-1 and 1-3-2 were tensile.

Fig. 9 displays curves of the rebar stress at the column bottom, and the vertical displacement with tension is positive and compression is negative. The rebar number is shown in **Fig. 3**. The rebars of sections 2-2--2-5 were exposed to compressive stress when no load was supplied because the axial pressure was applied above the middle column and the right-side column, and the rebar stress at section 2-1 was zero, as illustrated **in Fig. 9**.

Before point C, the compressive stresses of the left longitudinal rebars at the bottom of the second layer of the failed column (2-1-1, 2-1-4) (**Fig. 9(a)**), the longitudinal rebars on the right side at the bottom of the second layer of the middle column (2-3-2, 2-3-3) (**Fig. 9(c)**), the longitudinal rebars on the right side at the bottom of the two layers of the right-hand side column (2-4-2, 2-4-3, 2-5-2, 2-5-3) (**Fig. 9(d)** and **Fig. 9(e)**) are roughly negatively correlated with the growth in failure column

displacement; the compressive stresses of the remaining rebars in the bottom section of the column is approximately positively associated with the rise in failure column displacement. It indicates that the specimen was subjected to CAA at this stage, the bottom layer of the specimen showed an extrapolation trend, and the specimen was in the beam mechanism stage.

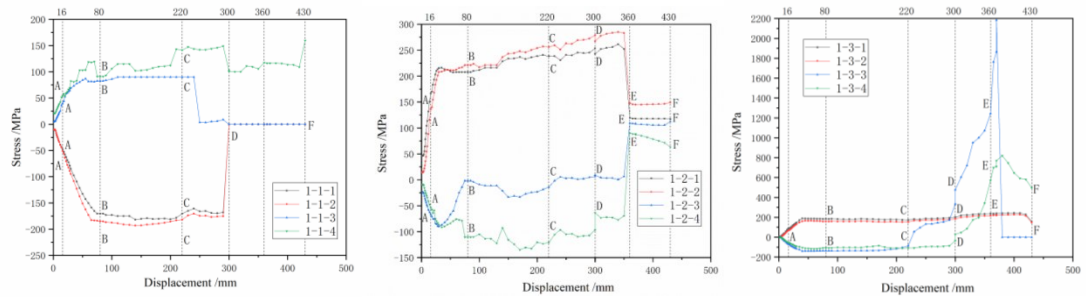

(a) (b) (c)

Fig. 8. Curves of the rebar stress at the beam end and the vertical displacement: (a) 1-1 section; (b) 1-2 section; (c) 1-3 section.

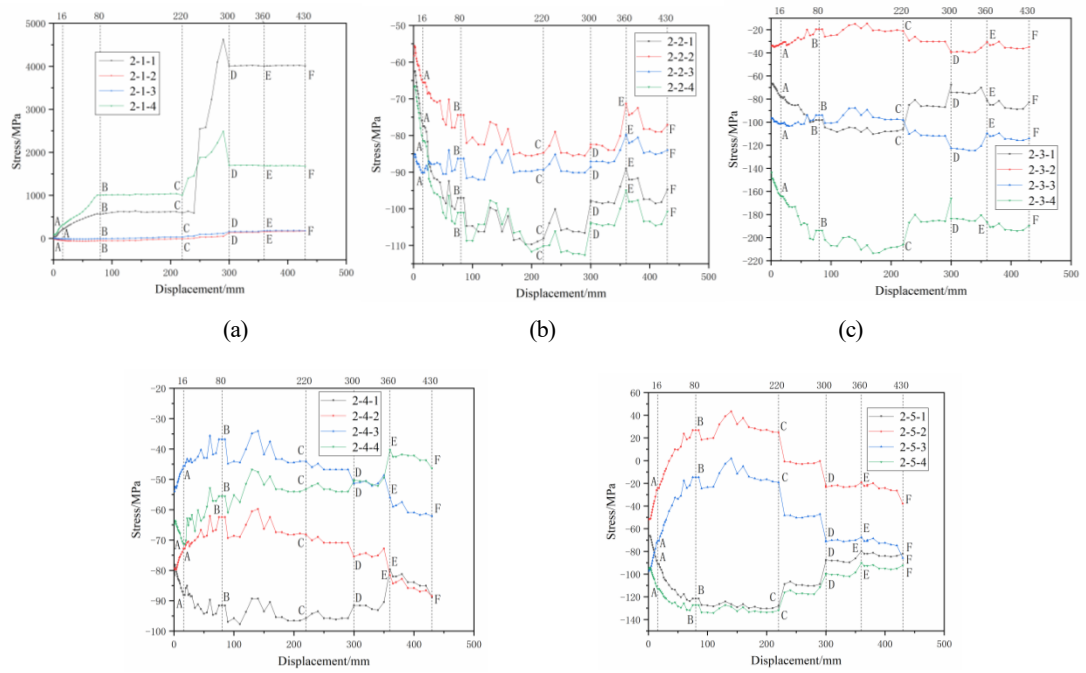

(a) (b) (c)

(d) (e)

Fig. 9. Curves of the rebar stress at the column bottom and the vertical displacement: (a) 2-1 section; (b) 2-2 section; (c) 2-3 section; (d) 2-4 section; (e) 2-5 section.

4 THEORETICAL ANALYSIS

4.1 Collapse resistance

The above results reveal that the structure deformation before reaching the ultimate bearing capacity was primarily caused by the plastic hinge rotation at sections of the beam ends 2 and 6, and the damage to the structure at this time was mainly controlled by portions of the beam ends 2 and 6. Therefore, this paper proposes a computational model, as shown in **Fig. 10**, where P is the bearing capacity of the structure and l_n is the net span length of the beam. The computational model uses the following assumptions: (1) Ignore the influence of axial force on bearing capacity and the axial deformation of the beam; (2) Ignore the beam shear deformation; (3) The destruction section occurs on the beam, not on the beam-column node and the side column; (4) The compressive stress-strain relations of concrete satisfy the Code for design of concrete structures [26], and the tensile strength of concrete is not considered; (5) The constitutive model of the tensile reinforcement is based on the Chang-Mander model, as shown in **Fig. 11**. E_{sh} is the tangent stiffness of the reinforcement after entering the reinforcement stage.

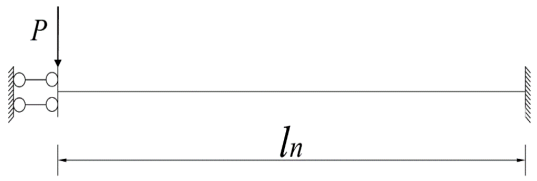

Fig. 10. Simplified computational model.

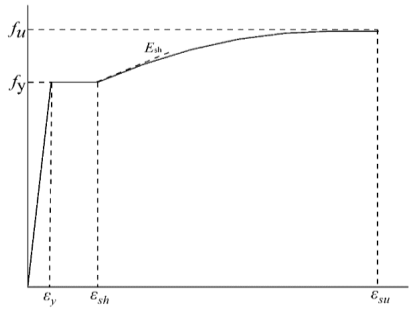

Fig. 11. Constitutive model of the tensile reinforcement.

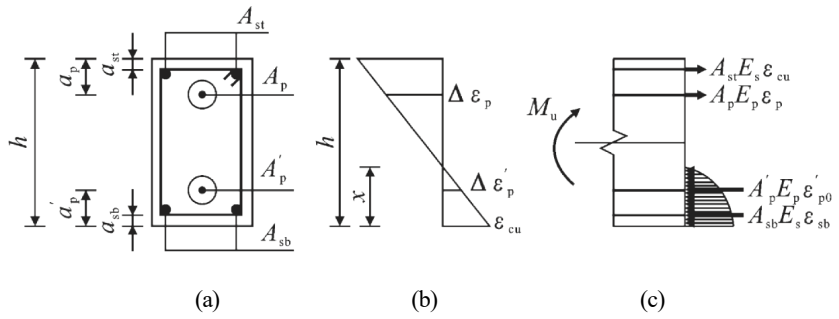

Fig. 12. Strain distribution of the beam section: (a) Cross-sectional form; (b) strain distribution; (c) stress state.

The ultimate bending moment of the flexural element can be calculated with the plane-section assumption, and the strains on the prestressed tendons after the concrete stress relief from its location also conform to this assumption. **Fig. 12** displays the strain distribution of the beam section. According to the strain coordination, Eq. (1) and Eq. (2) can be obtained.

$$\Delta \varepsilon_{p} \varepsilon_{cu} = h - a_{p} - x_{x} \quad (1)$$

$$\Delta \varepsilon_{p}' \varepsilon_{cu} = x - a_{p}' x \quad (2)$$

where ε_{cu} is the concrete strain at the edge of the compression zone; $\triangle\varepsilon_{p}$, $\triangle\varepsilon'_{p}$ are the strains of the upper and lower prestressed tendons after the concrete stress relief from the position of the prestressed tendon, respectively; a'_{p} and a_{p} are distances from the upper and lower prestressed tendons to the concrete edge, respectively; h is the beam height; x is the height of the concrete compression zone. The height of the concrete compression zone x and the strain of the prestressed tendon $\triangle\varepsilon'_{p}$ can be obtained from Eq. (1) and Eq. (2). The bending bearing capacity M_{u} of the beam section can be obtained from Eq. (3).

$$M_{u} = \alpha_{1} f_{c} bx \left(h_{0} - \frac{x}{2}\right) + \varepsilon_{sb} E_{s} A_{sb} \left(h_{0} - a_{st} - a_{sb}\right) + \Delta \varepsilon_{p}' E_{p} A_{p}' \left(\frac{x}{2} - \varepsilon_{p0}' E_{p} A_{p}' \left(a_{p}' - a_{st}\right)\right) \quad (3)$$

where α_1 is the equivalent rectangular stress coefficient; f_c is the axial compressive strength of concrete; b is beam width; h_0 is the distance from the combined force point of the prestressed tendons and the rebar in the tensile area to the edge of the concrete compression area; ε_{sb} is the strain of the compressive rebar; ε_p is the strain of the upper prestressed strand; ε'_{p0} is the peak strain of the lower prestressed strand; E_s and E_p are the elastic modulus of the rebars and the prestressed strands, respectively; A_{sb} is the cross-sectional area of the compressive rebar; a_{sb} and a_{st} are distances from the core of the compressive and tensile rebars to the edge of the concrete, respectively; A'_p and A_p are the cross-sectional areas of the lower prestressed strands and the upper prestressed strands, respectively. The collapse resistance P can be obtained from Eq. (4).

$$P = 4 M_{u} l_{n} \quad (4)$$

where l_n is the net span of the beam. It can be obtained that P=69.3 kN from Eq. (4). As shown in **Fig. 4**, the maximum vertical load of the curve between B and C is 60.9 kN, so the relative inaccuracy is 13.8%.

4.2 Critical collapse displacement

The critical collapse displacement, which reflects the final deformation capacity of the structure, is the critical displacement of the structure from the collapse state to the damage state. According to the test results, the compression zone at the top portions of the beam ends 1 and 5 and the lower portions of the beam ends 2 and 6 were severely damaged. When the specimen was on the verge of collapsing, the frame beam was a tensile member. Only the deformation of the steel strands in the tension zone was considered since the tension zone primarily carried the frame deformation at the beam end, and the steel strands mainly bore the bearing capacity in the collapse stage. The frame deformation

corresponding to the critical collapse displacement is displayed in **Fig. 13 (a)**. **Fig. 13(b)** illustrates the simplified computational model. where ln is the net span of the beam; δ_m is critical collapse displacement; l_i is the oblique length of the longitudinal rebar within the net span of the beam; $\triangle l_1$ and $\triangle l_2$ are the local elongations of the prestressed tendons near the beam hinge; h is the height of the beam; c is the distance from the prestressed tendon to the edge of the concrete.

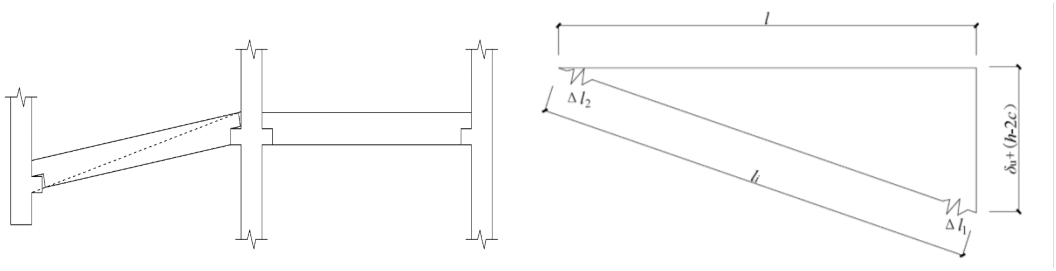

(a) (b)

Fig. 13. Critical collapse state: (a) Frame deformation at the critical collapse displacement; (b) schematic diagram of the simplified computational model.

The local elongations of the prestressed tendon near the beam hinge at the critical collapse displacement can be obtained from Eq. (5) and Eq. (6).

$$\Delta l_1 = s_1 \times \varphi_a = s_1 \times 0.4 \times \varphi \quad (5)$$

$$\Delta l_2 = s_2 \times \varphi_a = s_2 \times 0.4 \times \varphi \quad (6)$$

where s_1 and s_2 are the lengths of the prestressed tendon in the plastic hinges area of the tensile zone, and can be taken as 3/4 and 1/2 of the beam height, respectively; φ is the ultimate elongation of the prestressed tendon; φ_a is the uniform elongation of the prestressed tendon, take $\varphi_a = 0.4\varphi$. The diagonal length l_1 between the beam's upper and lower steel strand can be obtained from Eq. (7).

$$l_1 = \sqrt{l_n^2 + (h - 2c)^2} \quad (7)$$

The diagonal length l_2 of the prestressed tendon after loading can be obtained from Eq. (8).

$$l_2 = l_1 + \Delta l_1 + \Delta l_2 \quad (8)$$

Critical collapse displacement can be obtained from Eq. (9).

$$\delta_u = \sqrt{l_2^2 - l_n^2} - (h - 2c) \quad (9)$$

Thus, δu=429.24mm. The measured and calculated values of the critical collapse displacement were 430 mm and 429.24 mm, respectively, with a relative error of 0.1%.

5 CONCLUSION

This study conducted the collapse test of a two-story, two-span prestressed fabricated concrete frame to investigate the crack development, deformation capacity, progressive collapse resisting mechanisms, and failure mode of the frame under the bottom side column removal scenario. The deformation and resistance of the frame in progressive collapse were analyzed and calculated theoretically. The following conclusions are drawn:

(1) The collapse process can be divided into the beam mechanism stage and the collapse stage, and the mechanism transition displacement is 220 mm (C). In the beam mechanism stage, the frame column tended to extrapolate due to the CAA. In addition, the damaged side column developed transverse cracks close to the beam end, and the concrete cracks were primarily found in the compression zone at the beam ends. At the end of the test, the concrete in the compression zone at the beam end had been severely crushed and spalled. The adjacent span of the failure column had entirely collapsed, and the span far away from the broken column was almost intact.

(2) After point B, the tensioned prestressed tendons entered the yield phase. The structural deformation before the peak load (60.9 KN) was primarily brought on by the plastic hinge rotation of the sections at the beam ends 2 and 6, which served as the control sections of the structural failure. The structure lost its bearing capacity when the prestressed tendon fractured at point F, causing an ultimate collapse displacement of 430 mm.

(3) Simplified computational models of the progressive collapse resistance and the critical collapse displacement were proposed based on the control section of the structural failure and the critical collapse state of the specimen. Furthermore, the computational methods of the resistance and displacement against progressive collapse were derived. The results indicate that the calculated values agree well with the test values.

ACKNOWLEDGMENTS

The authors gratefully acknowledge the financial support provided by the National Natural Science Foundation of China under Grant No. 51608159.

REFERENCES

[1] ASCE/SEI 7-16. Minimum Design Loads and Associated Criteria for Buildings and Other Structures. Reston: American Society of Civil Engineers, 2016.5.

[2] Pearson C, Delatte N. Ronan (2005) Point Apartment Tower collapse and its effect on building codes. *Journal of Performance of Constructed Facilities*, 19(2): 172-177.

[3] Sozen MA, Thornton CH, Corley WG, Mlakar Sr PF. (1998) The Oklahoma City Bombing: Structure and mechanisms of the Murrah Building. *Journal of Performance of Constructed Facilities*, 12(3): 120–36.

[4] Omika Y, Fukuzawa K, Koshika N, Morikawa H, Fukuda R. (2005) Structural responses of World Trade Center under aircraft attacks. *Journal of Structural Engineering,* 131(1): 6–15.

[5] Sasani M, Sagiroglu S. (2008) Progressive collapse of reinforced concrete structures: a multihazard perspective. *ACI Structural Journal,* 105(1): 96–103.

[6] Adam J M， Buitrago M， Bertolesi E, Sagaseta J, Moragues J J． (2020) Dynamic performance of a real-scale reinforced concrete building test under a corner-column failure scenario. *Engineering Structures,* 210: 110414．

[7] Orton S L, Kirby J E. (2014) Dynamic response of a RC frame under column removal. *Journal of Performance of Constructed Facilities,* 28(4): 04014010.

[8] Pham A T, Tan K H. (2017) Experimental study on dynamic responses of reinforced concrete frames under sudden column removal applying concentrated loading. *Engineering Structure,* 139: 31-45．

[9] Pham A T, Tan K H. (2019) Static and dynamic responses of reinforced concrete structures under sudden column removal scenario subjected to distributed loading. *Journal of Structural Engineering,* 145(1): 04018235．

[10] .Qian K, Li B. (2012) Experimental and analytical assessment on RC interior beam-column subassemblages for progressive collapse. *Journal of Performance of constructed facilities,* 26(5): 576-589

[11] Yi W J, He Q F, Xiao Y, Kunnath S K. (2008) Experimental study on progressive collapse-resistant behavior of reinforced concrete frame structures. *ACI Structural Journal,* 105(4): 433–439.

[12] Li Y, Lu X Z, Guan H, Ye L P. (2011) An improved tie force method for progressive collapse resistance design of reinforced concrete frame structures. *Engineering Structures,* 33(10): 2931-2942.

[13] Nimse R B, Joshi D D, Oatel P V. (2014) Behavior of wet precast beam column connections under progressive collapse scenario: an experimental study. *International Journal of Advanced Structural Engineering,* 6(4): 149-59．

[14] Al-Salloum Y A, Alrubaidim A, Elsanadedy H M, Almusallam T H, Iqbal R A. (2018) Strengthening of precast RC beam-column connections for progressive collapse mitigation using bolted steel plates. *Engineering Structures,* 161: 146-160.

[15] Ravasini S, Belletti B, Brunesi E, Nascimbene R, Parisi F. (2021) Nonlinear dynamic response of a precast concrete building to sudden column removal. *Applied Sciences,* 11(2): 599.

[16] Yilin L, Zidong Z, Xiaowei C, et al. (2022) Experimental and numerical investigation of the progressive collapse of precast reinforced concrete frame substructures with wet connections. *Engineering Structures,* 256.

[17] Zidong Z, Xiaowei C, Yi L, et al. (2023) Progressive collapse analysis of precast reinforced concrete beam-column assemblies with different dry connections. *Engineering Structures,* 287.

[18] Qian K, Li B. (2018) Performance of precast concrete substructures with dry connections to resist progressive collapse. *Journal of Performance of Constructed Facilities,* 32(2): 04018005.

[19] Qian K, Liu Y, Yang T, Li B. (2018) Progressive collapse resistance of posttensioned concrete beam-column subassemblages with unbonded posttensioned strands. *Journal of Structural Engineering,* 144(1): 04018005.

[20] Jin Liu, Lan Dong-chyou, Deng Xiaofang, et al. (2023) Study on the mechanism of bondless prestressed beam-column structure against continuous collapse. *Journal of Building Structures,* 44(01): 68-79. (in Chinese)

[21] Liu Bingkang, Huang Shenjiang, Song Manrong, et al. (2010) Pseudo-dynamic Research on Post-Tensioned Precast Prestressed Concrete Frame. *Earthquake Engineering and Engineering Dynamics*, 30(5): 65-71. (in Chinese)

[22] Liu Bingkang, Huang Shenjiang, Song Manrong, et al. (2011) *Earthquake Engineering and Engineering Dynamics* Experimental Study of Seismic Performance of Prestressed Fabricated PC Frames. *China Civil Engineering Journal,* 44(11): 1-8. (in Chinese)

[23] Liu Bingkang, Song Manrong, Jiang Yaqiong, et al. (2011) Experimental Study on Seismic Performance of Post-Tensioned Precast Prestressed Concrete Frame. *Journal of Building Structures* .32(02): 24-32. (in Chinese)

[24] Liu Bingkang, Song Manrong, Huang Shenjiang, et al. (2011) Experimental Study on Seismic Performance of Three Story Post-Tensioned Precast RC Frame. *Journal of Building Structures,* 32(09):99-106. (in Chinese)

[25] GB50010-2010. Code for design of concrete structures. Beijing: China Architecture & Building Press, 2011.

[26] T/CECS 392:2021, Code for anti-collapse design of building structures. Beijing: China Planning Press, 2021.

[27] GB/T 2975-2018, Steel and steel products—Location and preparation of samples and test pieces for mechanical testing. Beijing: China Planning Press, 2018.

PROTECT 2024
Singapore
Aug 14-16, 2024

APPLICATION OF HEADED BARS IN PRECAST CONCRETE WET JOINTS UNDER ACCIDENTAL LOADS: EXPERIMENTAL AND NUMERICAL INVESTIGATIONS

Van Hung Nguyen[1,2], Xuan Dat Pham[1], Kang Hai Tan[2]

[1]Faculty of Building and Industrial Construction, Hanoi Univ. of Civil Engineering, Hanoi, Vietnam.

[2] School of Civil and Environmental Engineering, Nanyang Technological University, Singapore 639798, Singapore

Corresponding Author: Van Hung Nguyen

E-mail: hungnv4@huce.edu.vn

ABSTRACT

This study presents experimental and numerical investigations on behaviour of interior precast concrete (PC) joints under progressive collapse. Two types of joints, namely Type H and Type A, were studied, with Type H with a narrow wet connection utilising headed bars instead of hooked bars and Type A with a wide wet connection incorporating an additional headed bar layer (ABL) in the beam-joint region. The experimental results revealed that interior PC joints exhibited effective resistance against progressive collapse, characterised by four distinct stages: flexural, compressive arch action, transition, and catenary action stages. The usage of headed bars effectively prevented premature pull-out failure compared to conventional joints with hooked bars. Furthermore, including ABL in Type A joint yielded significant improvements in progressive collapse resistance and enhanced the integrity of the wet connections. It effectively prevented zero-applied load occurrence during the transition stage, as observed in Type H joint. A component-based joint model was developed and validated against the experimental results with satisfactory accuracy. Parametric studies using the validated model revealed positive impacts of horizontal restraint and the ABL ratio on enhancing the collapse resistance of PC joints. Designing PC structures with the strong-column-weak-beam concept and a proper balance between column and beam stiffness is recommended. These measures help facilitate the desired load transfer mechanisms and mitigate the risk of progressive collapse in PC joints.

Keywords: *Column removal scenario, Headed bars, Additional bar layer, Component-based joint mode*

1. INTRODUCTION

In recent years, precast concrete (PC) structures have become increasingly popular in the construction industry, offering numerous advantages such as assured structural performance, enhanced architectural features, improved site productivity, and cost efficiency. In Singapore, wet and dry connections are the two main types of PC connections used. Wet connections offer advantages in terms of ductility, durability, and fire resistance compared to dry connections. However, reinforcement tying and concrete casting in the joint region pose challenges for wet connections, making them more susceptible to progressive collapse.

To date, most previous research on progressive collapse behaviour has focused on cast in-situ reinforced concrete (RC) structures [1-3], with limited studies conducted on PC structures. PC structures with dry connections have been found to exhibit lower collapse resistance compared to those with wet connections or conventional cast in-situ RC structures, primarily due to brittle failure of welding or bolting connections [4-6]. However, some exceptions existed where PC structures with specialised dry connections and post-tensioning tendons have demonstrated improved collapse resistance, albeit with complex and costly construction processes [7].

The challenges specific to PC structures with wet connections, particularly in the joint region, have prompted further investigation into their progressive collapse behaviour and the development of strategies to enhance their collapse resistance. Previous studies have highlighted issues such as premature failure of welding and lap splicing of bars, inadequate lap lengths, and restrictions on welding methods [8, 9]. To address these issues, one potential solution is to use headed bars instead of hooked bars, as headed bars require only 75% of the anchorage length required for hooked bars [10, 11]. Furthermore, experimental tests on RC exterior joints subjected to seismic loading [12-14] have shown that headed bars provide significantly greater joint shear resistance, with failure mode governed by flexure in adjoining beams. However, there has been a lack of reported tests on beam-column joint specimens using headed bars as longitudinal reinforcement under progressive collapse.

This research aims to address these limitations and contribute to understanding progressive collapse behaviour of PC structures with wet connections. To achieve this goal, the study explored the potential benefits of incorporating headed bars as an alternative to reduce congestion in the beam-column joint region and prevent pull-out failure. In this regard, two interior PC joint specimens were tested under a middle column removal scenario (MCRS) (Section 3). One specimen employed headed bars instead of hooked bars, while the other incorporated an additional layer of headed bars (ABL) in the beam. Furthermore, by comparing the collapse behaviour of these two joints, the benefits of placing ABL on enhancing collapse resistance of PC joints were also highlighted. Moroever, to analyse the collapse behaviour of PC joints with headed bars, a component-based joint model (CBM) was proposed (Section 4). The model was validated against experimental test results and subsequently extended to investigate the effects of horizontal restraint and ratios of the ABL on the collapse behaviour of interior PC joints. It is important to note that although a significant amount of test data from the two specimens had been published previously [15], the additional data presented in this study are equally vital and directly pertinent to the discussion.

2. EXPERIMENTAL INVESTIGATION

2.1 DESIGN OF TEST SPECIMENS

Interior joint specimens were extracted from contra-flexural points of bending moments in a prototype 2D frame under a middle column removal scenario. Due to physical constraints of the laboratory facility, the specimens were scaled down to one-half while maintaining almost the same reinforcement ratios as the prototype structure. They were fabricated as PC members and assembled with wet connections. Subsequently, they were subjected to progressive loading at the middle joint until complete failure.

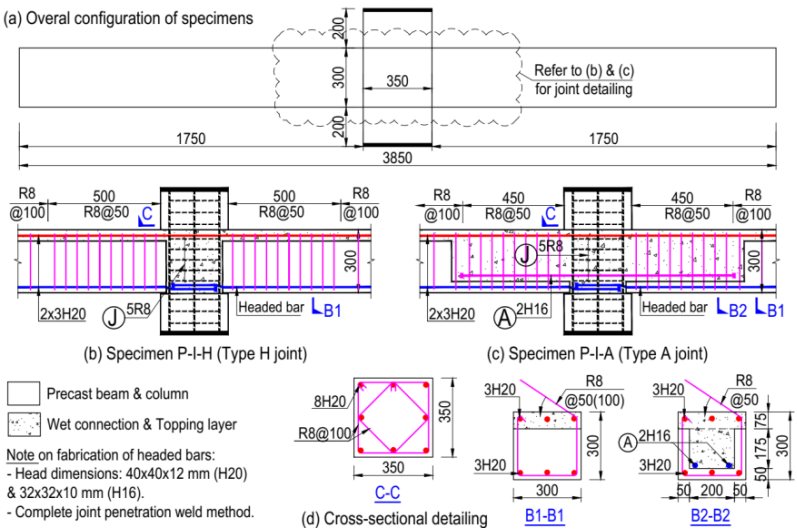

Figure 1. Design of test specimens

Figure 1 (a) illustrates overall configuration of the two joint specimens. Detailing features of Type H (specimens P-I-H) and Type A (specimen P-I-A) joints are shown in Figure 1 (b) and Figure 1 (c), respectively. Their cross-sectional detailing is shown in Figure 1 (d). Both specimens utilised headed bars instead of hooked bars to ensure adequate anchorage length for reinforcement and minimise congestion in the joint region. Additionally, specimen P-I-A featured placement of ABL in the joint region with a wide connection, which enhanced flexural resistance locally and strengthened the integrity of the wet connection.

Each specimen consisted of a lower and upper PC column stub measuring 200 mm in height, along with two PC beams measuring 1750 mm in length. The PC members were assembled using a wet connection and a 75 mm thick topping layer. In P-I-A, a prefabricated hollow U-shaped cross-section was incorporated at one end of the PC beam to facilitate bar splicing in the connection region. The extension length of the ABL was designed to be 450 mm, exceeding the required anchorage length for headed bars with a diameter of 16 mm, as specified in ACI 318-19 [11]. Transverse reinforcement in 8 mm diameter with a 135° hook was designed as two-legged and four-legged hoops for beam and column stirrups, respectively. In highly stressed regions, they were positioned with a spacing of 50 mm, whereas in the remaining regions, they were placed at a spacing of 100 mm.

2.2 TEST SETUP AND INSTRUMENTATION

Figure 2 (a) shows a typical test setup for an interior joint subjected to a MCRS. To ensure sufficient clearance height beneath the middle column stub and prevent contact with the strong floor during the experiment, vertical supports at the two beam ends were simulated using roller connections (denoted as ①) fixed to concrete blocks attached to the strong floor. A pair of horizontal pinned tie rods (denoted as ②) were utilised on both sides of the beam to represent horizontal restraints provided by adjacent bays. A hydraulic jack (denoted as ③) applied a vertical displacement-controlled loading to the middle joint by reacting against a portal steel frame. This loading simulated the downward movement resulting from the sudden removal of the column due to gravity loads.

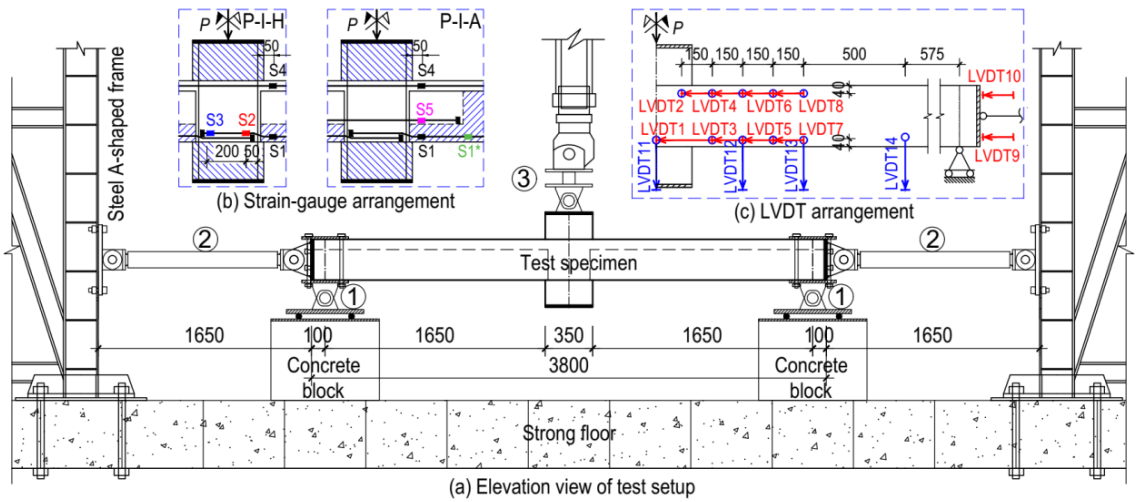

Figure 2. Elevation view of test setup

During the test, load cells or load pins were used to measure applied load, horizontal and vertical reactions. To get valuable insights into the distribution and transfer of forces within the joints, strain gauges were attached to reinforcing bars in these regions, as shown in Figure 2 (b). Apart from using traditional LVDTs (Linear Variable Differential Transformers) (Figure 2 (c)), the study also employed 2D digital image correlation (DIC) measurement, utilising GOM Correlate Professional 2021 [15-17]. DIC provided detailed information on displacement, crack pattern, crack width, and failure mode at each load increment.

3. EXPERIMENTAL RESULTS

3.1 MATERIAL TESTS

Tensile tests for reinforcing bars and compressive tests for concrete cylinders were conducted following ASTM specifications [18-20]. Table 1 shows material properties of reinforcing bars and concrete.

Table 1 Material properties of reinforcing bars and concrete

Material type		Yield strength (MPa)	Ultimate strength (MPa)	Ultimate strain (%)
Longitudinal reinforcement	Straight bar H16	544	626	11.6
	Straight bar H20	527	636	10.3
	Headed bar H16	560	602	6.5
	Headed bar H20	565	597	5.6
Stirrup	R6	332	429	13.9
	R8	345	423	14.3
Concrete: (diameter) (height)	150 mm & 300 mm	Compressive strength: 41.9 MPa Modulus of elasticity: 32.4 GPa		

3.2 OBSERVED CRACK PATTERNS AND BEAM DEFLECTION

Crack patterns and beam deflection observed in both specimens, P-I-H and P-I-A, exhibited similar behaviour. Therefore, specimen P-I-A was chosen to illustrate the progression of crack patterns and the beam deflection at critical stages, as shown in Figure 3 and Figure 4, respectively.

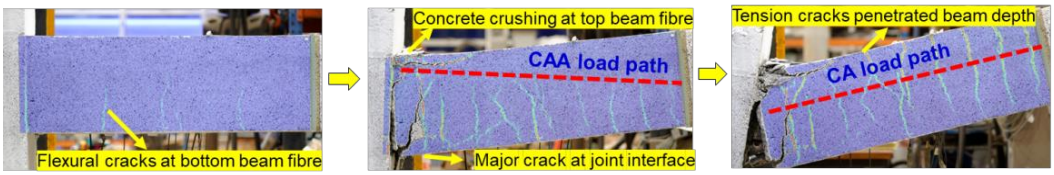

(a) Flexural stage (b) Compressive arch action stage (c) Catenary action stage

Figure 3. Development of crack pattern throughout loading of P-I-A

Figure 3 (a) shows that initial flexural cracks originated at the bottom beam fibre near the joint region, resulting from a sagging moment upon loading. These cracks gradually extended upwards with increasing middle joint displacement (MJD), leading to crushing of concrete at the top beam fibre adjacent to the joint. By connecting the tips of these flexural cracks, a compressive load path from the joint interface to the beam end support, indicating compressive arch action stage (CAA), was observed (Figure 3 (b)). Notably, high flexural demand and geometric discontinuity were the main contributing factors that resulted in the concentration of major cracks and fractures of the bottom bar in the beam near the joint interface. As catenary action (CA) was mobilised, tension cracks formed at the top beam fibre along the beam length, evenly distributed and aligned with locations of the beam stirrups, ultimately penetrating the

full beam depth at the end of CA (Figure 3 (c)). Failure mode was characterised by the fracture of the top bar in the beam for both specimens P-I-H and P-I-A.

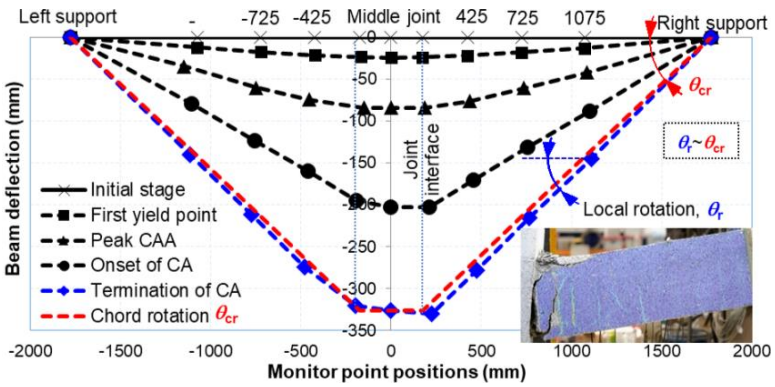

Figure 4. Overall deflection curves of P-I-A

From Figure 4, the deflection curves of the interior joints exhibited a relatively symmetric behaviour until the bottom bar fractured at the beginning of CA. These curves were predominantly straight, connecting the beam end to the middle joint interface, indicating the presence of a single major crack at the joint interface. According to UFC4-023-03 [21], for CA to be considered, the chord rotation θ_{cr} of a PC member must exceed 11.3 degrees. Specimens P-I-H and P-I-A had rotational capacities of 11.75 and 11.51 degrees, respectively, satisfying this requirement.

3.3 BAR STRAIN DEVELOPMENT

Detailed analysis of bar strain development provides insights into force transfer mechanisms of the joint during loading. The analysis focuses on P-I-H, with a comparison to P-I-A to highlight the differences.

In P-I-H (Figure 5 (a)), the bottom bar experienced significant tension strain (gauge S1, solid black curve), while the top bar near the joint interface underwent compression strain (gauge S4, dashed black curve) due to sagging moment. Yield penetration was observed, as indicated by peak strain in gauge S2 (red curve), surpassing yield strain ε_y at the capacity of the CAA stage. Furthermore, near the bar head (gauge S3, blue curve), the peak strain reached approximately $0.6\varepsilon_y$ during the CAA stage. It indicated that tensile force in the bottom bar was effectively transferred via the concrete bonding and head-bearing mechanism. After the fracture of the bottom bar, residual strains were recorded, and the strain in the top bar (S4) shifted to tension during the transition stage, increasing significantly with the occurrence of CA until failure.

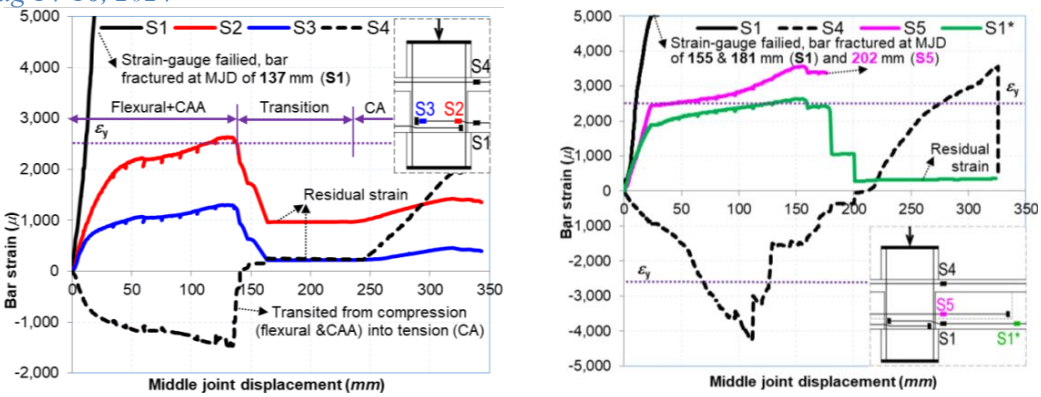

(a) P-I-H (b) P-I-A

Figure 5. Bar strain development

In P-I-A (Figure 5 (b)), the strain in the ABL (gauge S5, pink curve) was smaller than in the bottom bar layer (gauge S1, solid black curve) due to its smaller lever arm. The strain in the bottom bar layer near the joint interface (S1) was greater than that at the curtailment point of ABL (gauge S1*, green curve), indicating concentrated plastic deformation at the joint interface in P-I-A. The ABL at the bottom beam fibre resulted in a higher tension-compression bar ratio than P-I-H, leading to increased compression strain in the top bar near the joint interface (S4).

3.4 OVERALL QUASI-STATIC BEHAVIOUR

Structural behaviour is assessed by examining the relationship between vertical applied load and horizontal reaction versus MJD, as illustrated in Figure 6 (a) and Figure 6 (b) for specimens P-I-H and P-I-A, respectively. It is noted that the development of beam axial force (N), where positive values indicate tension, was approximately determined based on the average value of measured horizontal reaction force (H) in the beam tie rods.

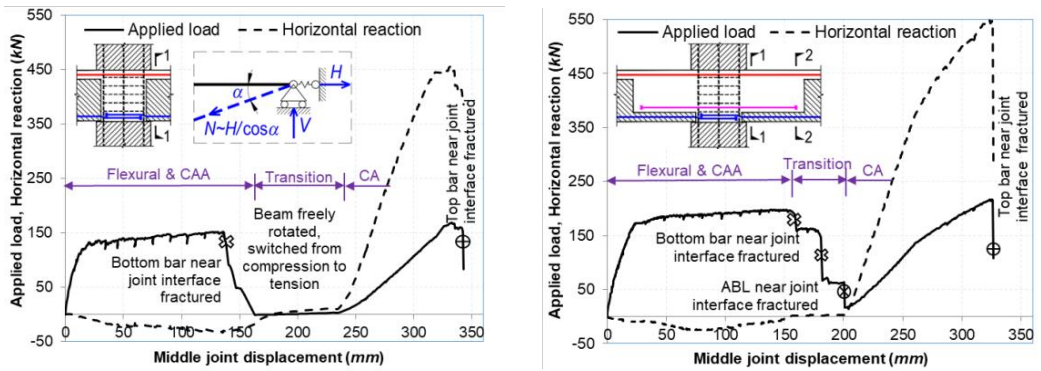

(a) P-I-H (b) P-I-A

Figure 6. Progressive collapse behaviour

From Figure 6, both specimens generally exhibited ductile behaviour against collapse. In contrast to the load-carrying mechanism observed in double-span beams, which generally consists of three stages (flexural, CAA and CA stages) [3], the interior joints displayed an additional transition stage. The applied load rapidly increased upon loading until reaching the

first peak load. Subsequently, it gradually increased until the end of the CAA stage, with a MJD of approximately one-half of the beam depth, which was accompanied by fracture of the bottom bar layer in P-I-H or sequential fractures of the bottom and ABL in P-I-A. Following the CAA stage, the joints experienced a transition stage characterised by a shift in the axial force of the beam from compression to tension. This was followed by the mobilisation of CA stage, resulting in a notable increase in axial tension force within the beam and load resistance of the joints. Eventually, failure occurred at a MJD of about one beam depth. Table 2 summarises the joint responses at critical stages.

Table 2 Joint responses at critical stages

Specimen	**Critical displacement** (mm)				**Critical load capacity** (kN)					
	1st peak load	End of CA	End of CA, δ_u	Predicted strength, P_n	At yield stage, P_y	At CAA stage, P_{CAA}	At CA stage, P_{CA}	$\frac{P_y}{P_n}$	$\frac{P_{CAA\_P\text{-}I\text{-}A}}{P_{CAA\_P\text{-}I\text{-}H}}$	$\frac{P_{CA\_P\text{-}I\text{-}A}}{P_{CA\_P\text{-}I\text{-}H}}$
P-I-H	22.5	135.6	332.8	117.7	127.4	150.1	169.0	1.08	-	-
P-I-A	23.4	150.0	325.8	162.9	170.7	188.3	216.5	1.05	1.25	1.28

Note: P_n is determined by cross-sectional analysis assuming symmetrical flexural yielding at critical beam sections and negligible horizontal reactions until reaching flexural capacity. P_y is defined as the load causing the yielding of steel bars.

Table 2 demonstrates that P_n was slightly lower than P_y in both specimens due to uncertainties in material properties. However, the actual load-carrying capacities surpassed the first peak load as a result of the significant mobilisation of CAA and CA stages, along with strain-hardening of reinforcing bars. Furthermore, the inclusion of ABL greatly improved collapse resistance of P-I-A compared to P-I-H, with ratios of $P_{CAA\_P\text{-}I\text{-}A}/P_{CAA\_P\text{-}I\text{-}H}$ and $P_{CA\_P\text{-}I\text{-}A}/P_{CA\_P\text{-}I\text{-}H}$ ranging from 1.25 to 1.28. Additionally, it is worth noting that in double-span beams, the MJDs typically fall within the range of one to twice the beam depth at the termination of CAA and CA stages [3]. Since the interior joint specimens were extracted from a typical double-span beam at contra-flexural points, the experimental findings on their MJDs aligned with this pattern. Specifically, the respective MJDs of the interior joint specimens varied between one-half and one beam depth.

Development of CAA in interior joints against collapse

Compression deformation in the PC beam is minimal and highly influenced by the presence of physical gaps in the horizontal tie rods. While axial restraint plays a critical role in activating CAA mechanism, it is recommended to provide rotational restraint at the ends of the beam to effectively mobilise CAA [22]. In the tested interior joint specimens, only axial restraint was provided through horizontal tie rods (Figure 2). As a result, although CAA was triggered, its significance was not as pronounced as in double-span beams that had both axial and rotational restraints [3]. This was evident from the relatively small beam axial force in compression observed throughout loading, indicated by the dashed black curves in Figure 6.

Effect of ABL

In specimen P-I-H, which had a narrow connection without strengthening bars, the bottom bar near the middle joint experienced a complete fracture at the end of CAA stage. This led to a loss of sagging moment resistance in the beam, causing the applied load to drop to zero.

Consequently, the beam attained rotational freedom, and the beam end freely moved inward towards the loading point. As the MJD increased, the beam's inward movement filled the gap in the tie rods. Subsequently, the applied load began to increase again as the top bar layer of the beam contributed to the load-resisting mechanism, leading to pure CA against collapse.

4. NUMERICAL INVESTIGATION

4.1. COMPONENT-BASED JOINT MODELLING APPROACH

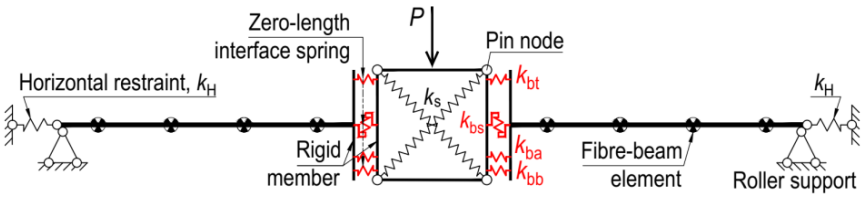

Figure 7. Overall configuration of proposed component-based model

Accurately representing PC joints can be achieved by employing explicit modelling techniques that involve using 3D solid elements to capture behaviour of the entire joint. However, this approach is computationally demanding and may not be feasible for large-scale progressive collapse simulations. As an alternative, a component-based model (CBM) is widely adopted, where critical components are represented by zero-length springs [23-25]. As seen in Figure 7, fibre-beam elements were used to model beam components. To capture the transfer of flexural and axial forces in the critical beam section, bar force-slip springs k_{bt} & k_{bb} were utilised at the joint interfaces in specimens P-I-H and P-I-A. Additionally, additional bar springs k_{ba} were introduced to account for contribution of ABL in specimen P-I-A. In addition, interface shear behaviour was simulated using very high-stiffness elastic linear springs k_{bs} to ensure sufficient shear capacity in the joint. Joint shear distortion, on the other hand, was modelled using diagonal springs k_s, which were also assumed to be elastic linear springs with very high stiffness. This was because interface shear failure and diagonal cracks in the joint core were not observed in both specimens.

Constitutive models of force-slip springs for non-headed deformed bars have been established by previous researchers [23, 24, 26]. However, for headed bars under a MCRS, no specific model exists. Therefore, the models developed by Yu and Tan (2014) [23] and Nguyen *et al.* (2022) [26] were adapted and improved for headed bars under tension and compression, respectively. In the proposed model, the headed bar was simplified as a straight bar with an equivalent length l_{eq} calculated as $l_{emb} + 5d_b$, where l_{emb} is the straight embedment length, and d_b is the bar diameter. Average bond stress values proposed by Lowes and Altoontash (2003) were adopted in this study.

The model considered slip induced by extension of bars between flexural cracks near the critical interfaces. DIC analysis revealed that a significant flexural crack located 100 mm from the joint interface in specimens P-I-H and P-I-A contributed approximately 5 mm to the total slip observed in the k_{bb} force-slip springs at the joint interface. The properties of the bar force-slip

springs are shown in Figure 8 (a). Furthermore, a linear regression analysis on average values of horizontal reactions and movements from left and right beam tie rods in the test yielded the horizontal stiffness and initial gaps, as shown in Figure 8 (b).

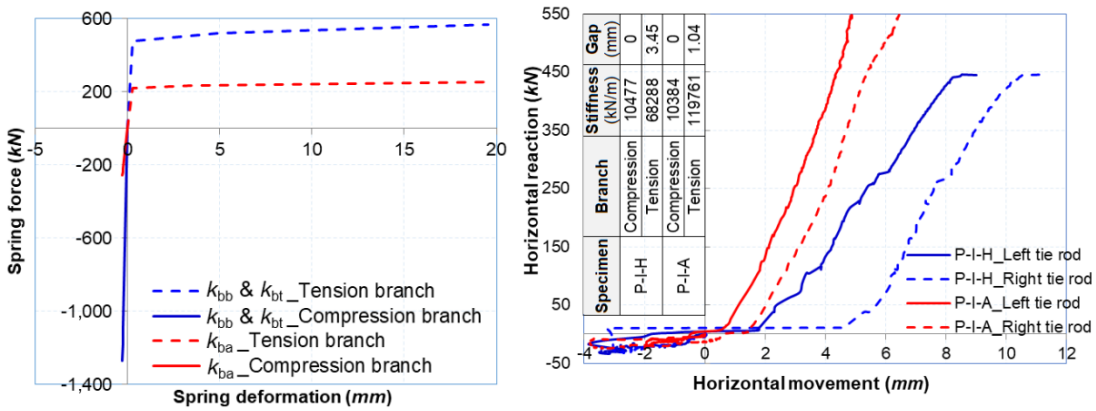

Specimen	Branch	Stiffness (kN/m)	Gap (mm)
P-I-H	Compression	10477	0
	Tension	68288	3.45
P-I-A	Compression	10384	0
	Tension	119761	1.04

(a) Springs k_{bb}, k_{bt} & k_{ba} (b) Horizontal restraint properties

Figure 8. Constitutive model of bar force-slip springs and horizontal restraint properties

4.2. MODEL VALIDATION

Interior PC joints under progressive collapse were simulated using the Engineer's Studio software, which incorporates fibre-beam elements and zero-length springs. The numerical results were compared with the test results, as shown in Figure 9. The comparison between numerical predictions and test results demonstrated good agreement in terms of the applied load versus MJD. Additionally, the sequence of spring failure observed in the numerical simulations aligned with the observed bar fractures in both specimens. It is important to note that while the reinforcing bars in the test specimens fractured sequentially and the failure mode was asymmetric, the numerical analyses showed an almost simultaneous fracture of the bar springs on both sides. Consequently, the CBM either slightly underestimated or overestimated the collapse resistance of the joint compared to the test results.

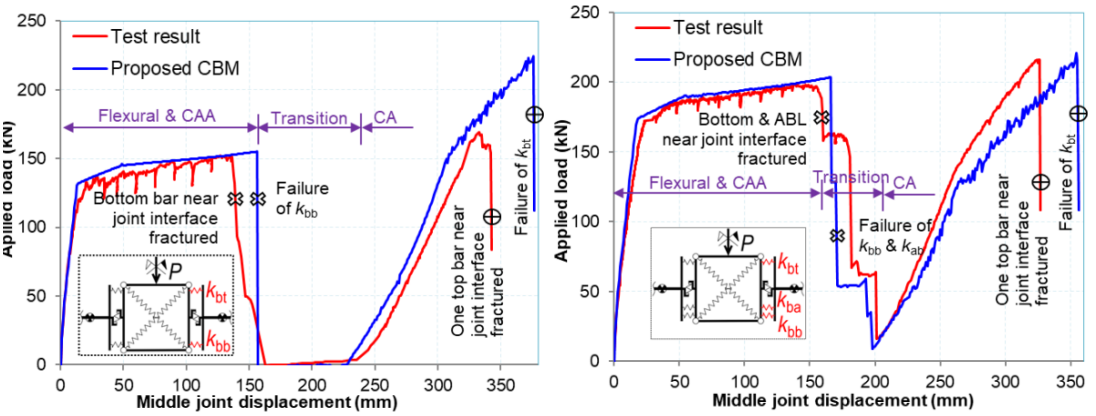

(a) P-I-H (b) P-I-A

Figure 9. Validation of proposed CBM

4.2. PARAMETRIC STUDY

Due to the high cost of the experimental program, the validated CBM was utilised to investigate the impact of various factors on the collapse behaviour of interior PC joints. Specifically, the study focused on examining the effects of horizontal restraint and ratios of ABL. Specimen P-I-A was selected as the control specimen. All design parameters were kept the same as those in P-I-A except for investigated parameters.

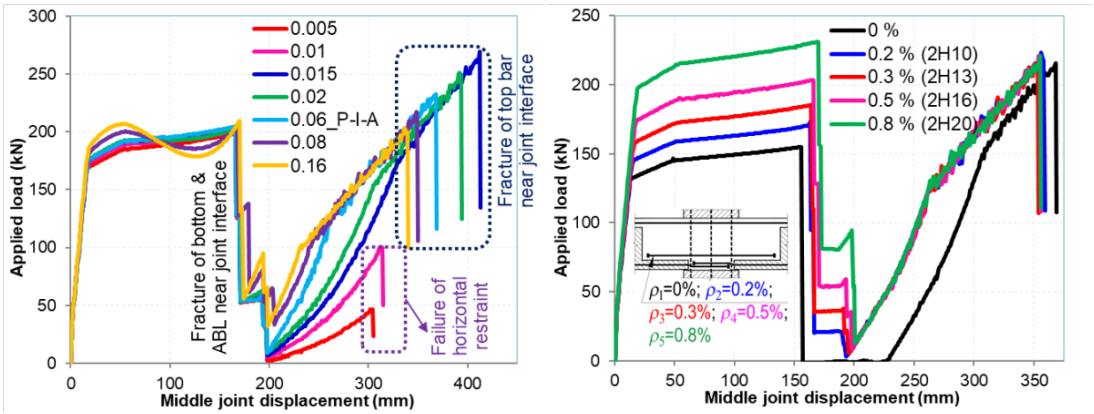

(a) Effect of horizontal restraint (b) Effect of ratios of ABL

Figure 10. Effect of horizontal restraint and ratios of ABL

Effect of horizontal restraint

In a 2D frame under a penultimate column removal scenario, flexural stiffness of the supporting exterior column is indeed a key factor considered in determining the horizontal restraint of the bridging beam. To investigate effect of horizontal restraint, a normalised stiffness coefficient was introduced as $k=k_H l/(E_c A_c+E_s A_s)$, where k_H is horizontal stiffness provided by the exterior column, l is the length of the single-span beam, A_c and A_s are the total cross-sectional areas of concrete and steel bar in the beam section, respectively, E_c and E_s are the elastic modulus of concrete and steel bar, respectively.

In the control specimen P-I-A, the coefficient k was found to be 0.06, considering the actual horizontal restraint stiffness measured in the test (Figure 8 (b)). For the parametric study, six additional values of k were selected, ranging from 0.005 to 0.16. It should be noted that the value of k = 0.005 represents a case with relatively small stiffness of horizontal restraints, considering exterior columns in a cross-section of 250 mm x 250 mm. On the other hand, the value of k = 0.16 represents a scenario with a very large stiffness of horizontal restraint, considering exterior columns in a cross-section of 600 mm x 600 mm. Load-displacement curves in Figure 10 (a) highlight the importance of horizontal restraints in triggering CAA and CA in PC joints.

Looking at the development of CAA, a higher k led to a higher CAA capacity at a smaller MJD with a more pronounced descending phase of applied load right after the CAA capacity (Figure

10 (a)). This was attributed to a greater compression force induced in the beam under a larger axial restraint. In contrast, weak horizontal restraint (say $k < 0.015$, corresponding to exterior columns in a cross-section smaller than 350 mm x 350 mm) led to failure of the horizontal restraint, hindering significant CA mobilisation (see the red and pink curves in Figure 10 (a)). In contrast, the CA could be effectively mobilised. Moreover, at k=0.015, a transition state in CA mobilisation occurred (see the blue curve in Figure 10 (a)). Prior to this point, P_{CA} and δ_{CA} exhibited a significant increase with increasing k. However, beyond k=0.015, further increases in k reduced horizontal movement at the beam ends, diminishing rotational capacity and resulting in lower P_{CA} and δ_{CA}. In addition, fracture of the steel bar in the beam near the joint interface rather than failure of the horizontal restraint dominated the joint behaviour.

Hence, it is crucial to achieve a balance between column and beam stiffness to prevent structural failures. A significantly weaker exterior column may experience tension-induced failure during the CA stage, while an excessively strong column restricts horizontal displacement and reduces rotational capacity under large deformations.

Effect of ratio of ABL

According to ACI 318-2019 [11], to ensure the ductile failure of the beam, it is required to limit the maximum reinforcement ratio to $\rho_{bmax}=0.75b_1(0.85f_c'/f_y)[600/(600+f_y)]$, where b_1=0.783 for concrete compressive strength f_c'=40 MPa and yield strength of reinforcing bar f_y=500 MPa. Taking this into consideration, five values of the ratio of ABL ρ ranging from 0% to 0.8%, were selected. It should be noted that the control specimen P-I-A had ρ=0.5%. Load-displacement relationships plotted in Figure 10 (b) demonstrated the beneficial effects of the ratio of ABL on the collapse resistance of PC joints.

It is seen in Figure 10 (b) that increasing ρ from zero to 0.8% led to steady growth in peak load-carrying capacity at CAA stage but not at CA stage. It could be explained by the increase in the sagging moment resistance of the beam section near the middle joint provided by the ABL. Meanwhile, CA stage was dominated by the top steel bars, which were the same in all investigated specimens.

5. CONCLUSIONS

In conclusion, this study investigated the behaviour of emulative interior precast wet joints under progressive collapse, specifically focusing on Type H joint with headed bars replacing hooked bars and Type A joint incorporating ABL in the beam-joint region. Experimental tests were conducted to validate the performance of these joints, followed by the development and validation of advanced CBM.

The findings of this study can be summarised as follows:

a) The usage of headed bars and the placement of ABL in the beam-joint region proved effective in compensating for negative effects of geometric and reinforcement discontinuity

at the joint interface. This resulted in the prevention of pull-out failure, which was observed in conventional PC joints with hooked bars under a MCRS.

b) The behaviour of interior PC joints during progressive collapse was characterised by four distinct stages: flexural, CAA, transition, and CA stages. The inclusion of ABL in Type A joint with a wide connection prevented the occurrence of zero-applied load during the transition stage, which was observed in Type H joint with a narrow connection.

c) Enhancing collapse resistance of PC joints involves increasing horizontal restraint stiffness and resistance as well as optimising the ABL ratio in the beam. This can be achieved by designing exterior columns per the strong-column-weak-beam concept and ensuring a proper balance between the stiffness of columns and beams. These measures help facilitate the desired load transfer mechanisms and mitigate the risk of structural failures in PC joints.

These findings contribute to understanding of progressive collapse behaviour of interior PC joints and provide valuable insights for the design and optimisation of such joints in structures. The developed and validated component-based joint models offer a reliable tool for predicting the collapse behaviour of PC joints and can be used for further parametric studies and structural analysis.

ACKNOWLEDGMENTS

The authors gratefully acknowledge the funding provided by Changi Airport Group of Singapore for the “Precast progressive collapse testing programme” (Award No. NTU Ref: 2018-1451). The views and opinions expressed in this paper are solely those of the authors and do not necessarily reflect those of Changi Airport Group.

REFERENCES

[1] Yi W-J, He Q-F, Xiao Y, Kunnath SK. Experimental study on progressive collapse-resistant behavior of reinforced concrete frame structures. ACI Structural Journal. 2008;105:433.

[2] Su Y, Tian Y, Song X. Progressive collapse resistance of axially-restrained frame beams. ACI Structural Journal. 2009;106.

[3] Yu J, Tan KH. Structural Behavior of RC Beam-Column Subassemblages under a Middle Column Removal Scenario. Journal of Structural Engineering. 2013;139:233-50.

[4] Elsanadedy HM, Almusallam TH, Al-Salloum YA, Abbas H. Investigation of precast RC beam-column assemblies under column-loss scenario. Construction and Building Materials. 2017;142:552-71.

[5] Qian K, Li B. Performance of precast concrete substructures with dry connections to resist progressive collapse. Journal of performance of constructed facilities. 2018;32:04018005.

[6] Qian K, Li B, Liu Y. Integrity of precast concrete structures to resist progressive collapse. Geotechnical and Structural Engineering Congress 20162016. p. 1976-86.

[7] Qian K, Liang S-L, Fu F, Fang Q. Progressive collapse resistance of precast concrete beam-column sub-assemblages with high-performance dry connections. Engineering Structures. 2019;198:109552.

[8] Kang S-B. Structural behaviour of precast concrete frames subjected to column removal scenarios. PhD Thesis, Nanyang Technological University, Singapore. 2015.

[9] Nimse RB, Joshi DD, Patel PV. Behavior of wet precast beam column connections under progressive collapse scenario: an experimental study. International Journal of Advanced Structural Engineering (IJASE). 2014;6:149-59.

[10] Shao Y, Darwin D, O'Reilly M, Lequesne RD, Ghimire KP, Hano M. Anchorage of conventional and high-strength headed reinforcing bars. University of Kansas Center for Research, Inc.; 2016.

[11] ACI318-19. Building code requirements for structural concrete and commentary. American Concrete Institute; 2019.

[12] Hegger J, Sherif A, Roeser W. Nonseismic design of beam-column joints. Structural Journal. 2003;100:654-64.

[13] Kang TH-K, Ha S-S, Choi D-U. Bar Pullout Tests and Seismic Tests of Small-Headed Bars in Beam-Column Joints. ACI Structural Journal. 2010;107.

[14] Nguyen VH, Tan KH. Progressive collapse behaviour of earthquake-damaged interior precast concrete joints with headed bars and plastic hinge relocation. Engineering Structures. 2024;306:117817.

[15] Nguyen VH, Tan KH. Progressive collapse behaviour of advanced precast reinforced concrete joints with headed bars and plastic hinge relocation. Engineering Structures. 2023;293:116603.

[16] 2021 GCP. GOM Suite, (https://www.gom.com/en/products/gom-suite/gom-correlate-pro).

[17] Pan B, Qian K, Xie H, Asundi A. Two-dimensional digital image correlation for in-plane displacement and strain measurement: a review. Measurement science and technology. 2009;20:062001.

[18] A995/A995M-19. Standard Specification for Deformed and Plain Stainless Steel Bars for Concrete Reinforcement. ASTM International; 2019.

[19] ASTM-A970/A970M-09. Standard Test Method for Headed Steel Bars for Concrete Reinforcement. ASTM International; 2019.

[20] ASTM-C39/C39M-01. Standard Test Method for Compressive Strength of Cylindrical Concrete Specimens. ASTM International; 2014.

[21] UFC4-023-03. Design of structures to resist progressive collapse. DoD (Department of Defense), United States; 2016.

[22] Yu J, Tan KH. Analytical model for the capacity of compressive arch action of reinforced concrete sub-assemblages. Magazine of Concrete Research. 2014;66:109-26.

[23] Yu J, Tan KH. Numerical analysis with joint model on RC assemblages subjected to progressive collapse. Magazine of Concrete Research. 2014;66:1201-18.

[24] Lowes LN, Altoontash A. Modeling reinforced-concrete beam-column joints subjected to cyclic loading. Journal of Structural Engineering. 2003;129:1686-97.

[25] Nguyen VH, Tan KH. Bond-slip model of headed bar and its application to component-based model for precast concrete joints under accidental loads. Engineering Structures. 2024;293:116603.

[26] Nguyen VH, Yu J, Tan KH. Component-based joint model for RC frames with conventional and special detailing against progressive collapse. Structures: Elsevier; 2022. p. 820-37.

PROTECT 2024
Singapore
Aug 14-16, 2024

EXPERIMENTAL STUDY ON THE COLLAPSE RESPONSE OF REINFORCED CONCRETE FLAT SLAB STRUCTURES WITH COLUMN CAPITALS

Xuan Dat Pham[1], Trung Hieu Nguyen[1], Ngoc Tan Nguyen[1], Kim Anh Do[1], Anh Tuan Pham[2], Quoc Cuong Tran[1], Truong Thang Nguyen[1], Van Hung Nguyen[1]

[1]Faculty of Building and Industrial Construction, Hanoi Univ. of Civil Engineering, Hanoi, Vietnam.

[2]Vietnam Institute for Building Science and Technology, 81 Tran Cung Street, Hanoi, Vietnam.

Corresponding Author: Van Hung Nguyen

E-mail: hungnv4@huce.edu.vn

ABSTRACT

This research investigates the collapse behaviour of flat slab structures with column capitals through experimental analysis. Two 1/3-scaled specimens were subjected to complete collapse by uniformly distributed loads simulated by eight separate piles of concrete cubes. Accidental scenarios involving a loss of vertical support at mid-span or penultimate column locations were examined. The experimental observations yield several key findings:

- Flat slab structures exhibit significant ductility, with vertical deflections reaching approximately 9% of a single span length. Collapse loads exceeded corresponding yield-line predictions by 26% and 11% for specimens with column capitals, indicating substantial mobilization of tensile membrane action.
- Column capitals play a vital role in enhancing collapse behaviour by strengthening the structure and delaying or even preventing punching shear failure on the top of Columns C-1 to C-5. This enhancement allows for increased deflection capacity and the ability to carry greater applied loads.
- At large deformations, nonlinear load redistribution among columns surrounding affected slab panels is observed, with the majority of applied load redistributed to the three columns nearest to the column experiencing local failure.

Overall, this study underscores the importance of column capitals in mitigating progressive collapse in flat slab structures and provides valuable insights into their collapse behaviour under various loading conditions.

Keywords: *progressive collapse, reinforced concrete flat slab, column capital.*

1. INTRODUCTION

The structural response of flat slab structures following the initial punching shear failure is widely acknowledged as highly complex, with the potential for progressive collapse hinging primarily on two factors. Firstly, the ability of the surrounding slab structure to establish an alternative load path, redistributing gravity loads to neighboring columns, plays a pivotal role. This redistribution mechanism operates either through flexural mode, where the affected slab deflects insignificantly, or tension mode, where the slab acts as a hanging net under considerable deformations. Secondly, the capacity of existing slab-column connections to withstand the combined forces of bending, shear, and tension is critical. Despite reinforced concrete (RC) flat slabs being favored for office and residential buildings due to their rapid and straightforward construction process and optimal clear story height, their reserved shear strength in slab-column connections is often notably low, presenting a significant drawback in mitigating progressive collapse [1-4].

This research endeavors to address these two pivotal factors concerning flat slab systems with column capitals. It utilizes test data from two RC flat slab specimens extracted and scaled down from an actual building structure at a ratio of 1/3, which were subsequently subjected to uniformly distributed loading conditions. Recorded data at each loading step include load-displacement curves, strain gauge readings, and final failure modes of the test specimens, providing valuable insights into the collapse behavior of flat slabs. It is noteworthy that while a substantial portion of the test data from the two specimens has been previously presented elsewhere [5-7], the remaining data presented herein are equally crucial and directly relevant to the aforementioned discussion.

Previous experimental studies in this field have predominantly focused on either the collapse response of individual column capitals subjected to combined bending-tension and shear actions [8, 9], or the response of flat slabs without column capitals [10-13]. Unfortunately, there is a notable absence of information regarding the collapse response of flat slabs with column capitals. This research seeks to fill this gap, driven by the inadequacy of existing studies in addressing this specific aspect.

2. EXPERIMENTAL INVESTIGATION

2.1 DESIGN OF TEST SPECIMENS

Figure 1 shows the typical structural layout of the prototype building chosen for this investigation. The span length of the prototype building in both the x- and y-directions was 6.0 m, with the flat slab measuring 240 mm in thickness and the column capital 360 mm. Typical columns had cross-sectional dimensions of 600 mm by 600 mm. The structure's design live load and imposed dead load were 4.0 kN/m² and 3.0 kN/m², respectively.

Forensic investigations into actual building collapse events have yielded two significant conclusions. Firstly, the loss of vertical support resulting from punching shear failure of a slab-column connection or column removal due to an explosion can trigger a building collapse. Secondly, gravity loads acting on the building structures during collapse stages typically exhibit uniformly distributed patterns. In this study, two scenarios of column loss, i.e., at the Mid-span Column location (MC Scenario) (case (a) in Figure 1) or the Penultimate Column location (PC

Scenario) (case (b) in Figure 1) have been selected. These scenarios are examined using two flat slab specimens, named MC and PC, respectively. Each specimen comprises two slab panels positioned just above the local failure and slab extensions to simulate the effects of adjacent panels.

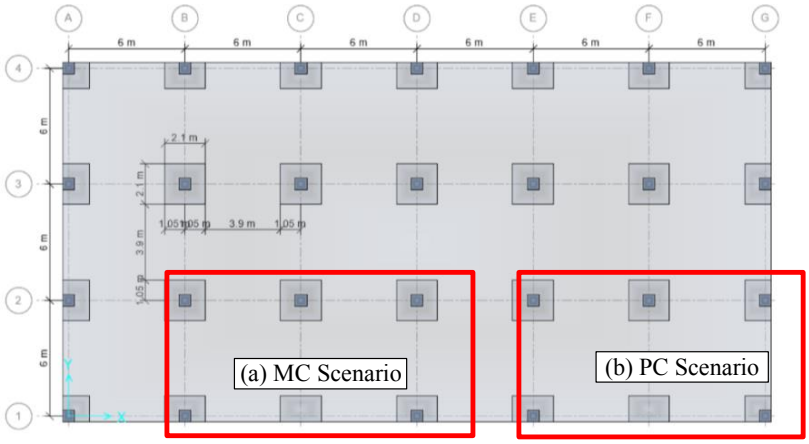

Figure 1: Structural layout of the Prototype building and two investigated accidental scenarios

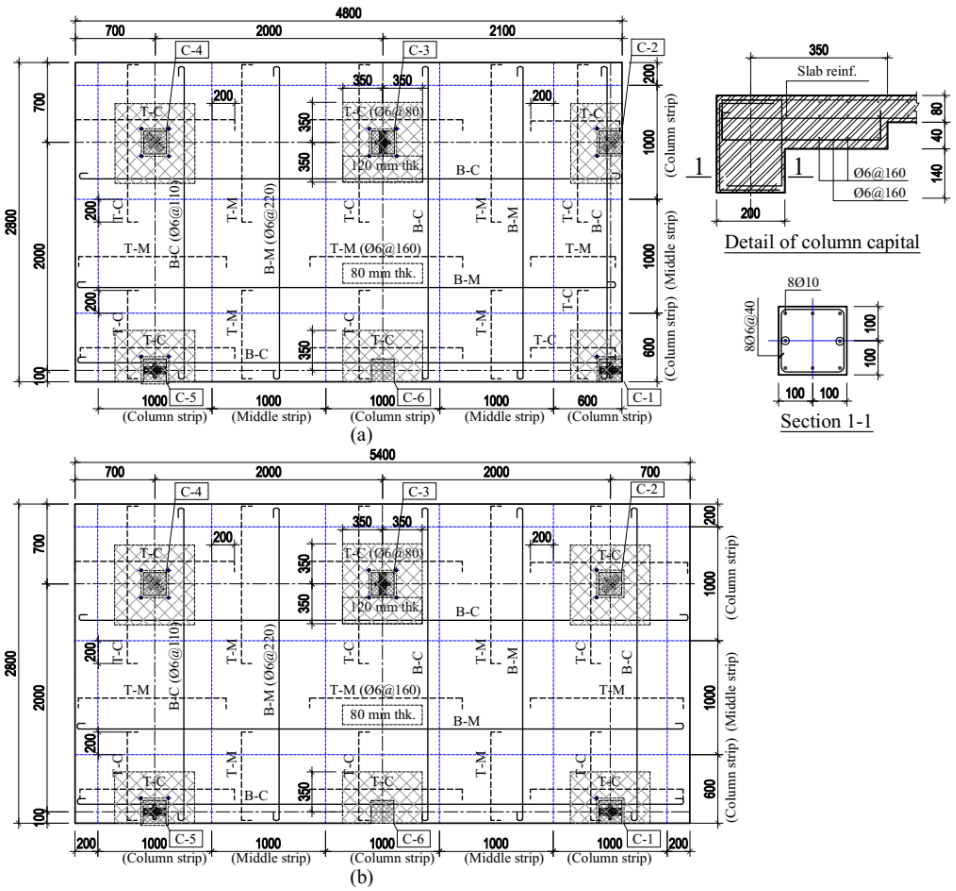

Figure 2: Detailed layout of test specimens: (a) Specimen MC; (b) Specimen PC

Due to the lab constraint, the specimens were scaled down one-third while maintaining the same reinforcement detailing and ratios as the prototype structure. The overall dimensions of the test structures were 2800 x 5400 x 80 (120) mm for the MC specimen and 2800 x 4800 x 80 (120)

mm for the PC specimen. Each specimen was supported by five columns, denoted as C-1 to C-5, in the counter-clockwise direction. To simulate adjacent slab panels, 700-mm wide slab extensions were added to three sides of the tested area of the MC specimen and two sides of the PC specimen.

It should be emphasized that horizontal constraints play an important role in mobilising tensile membrane action (TMA) in affected slabs under progressive collapse scenarios. However, in the scenario involving a Penultimate Column location (Specimen PC), the slab is allowed to move freely in the horizontal direction. Therefore, there was no need to provide horizontal restraint for Specimen PC. In contrast, for the Mid-span Column location (Specimen MC), the specimen could potentially be restrained horizontally by the adjacent beam-slab system. However, due to the limitations of the lab facilities, horizontal restraints could not be provided for this specimen. It is important to highlight that the absence of horizontal constraints would result in more conservative estimates of progressive collapse resistance of RC slabs.

Details of the two specimens are shown in Figure 2. In addition, their main design configuration and reinforcement detailing are summarised in Table 1. Moreover, before conducting the experiment, concrete and steel bars were tested to obtain mechanical properties of materials. Specifically, the concrete had an average compressive strength of 20.1 MPa, determined from six cylinders (three samples per assemblage) tested at 180 days (six months). The yield strength and ultimate strength of reinforcing bars were 380 MPa and 410 MPa, respectively.

Table 1. Design of test specimens

Specimen	Overall Dimensions (L_x x L_y x d)	Column strips		Middle strips	
		Top reinforcement	Bottom reinforcement	Top reinforcement	Bottom reinforcement
MC	2800x4800x80 (120)	Φ6@80	Φ6@110	Φ6@160	Φ6@220
PC	2800x4800x80 (120)	(ρ_{top} = 0.47%)	(ρ_{top} = 0.47%)	(ρ_{top} = 0.23%)	(ρ_{bot} = 0.17%)

Note: All dimensions are in mm

2.2 LOADING PROCEDURE AND INSTRUMENTATION

In this investigation, both specimens were subjected to static loading until failure using uniformly distributed loads applied through eight separate piles of concrete cubes. Figure 3(a) depicts a photograph of the loading process conducted on the PC specimen. The concrete cubes, sourced from multiple concrete batches, measured precisely 150 x 150 x 150 mm and weighed 0.08 kN each. Each pile's horizontal dimensions were 750 mm x 750 mm, allowing for 25 cubes per layer and resulting in a uniform load of 2 kN/m². Each pile transferred the load to its designated slab area through its three legs arranged uniformly in a triangular configuration, resulting in 24 loading points across the entire test area, denoted as P1 to P24, as depicted in Figure 3(b). To account for the effect of adjacent slab panels, two layers of concrete cubes were placed on top of the slab extension strips.

a) A photo of loading process on PC specimen

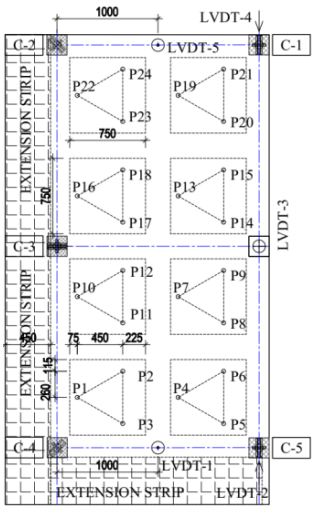

b) Loading scheme

Figure 3: Loading configuration and instrumentation

Initially, a distributed load of 4.14 kN/m² was applied to the slab extension areas, followed by a step-by-step loading procedure for the two testing slab panels. At each loading step, a set of 12 concrete cubes (equivalent to approximately half of one layer) was placed on each pile, resulting in a load increase of 1.0 kN/m².

The deflection of the testing specimens was measured using three Linear Variable Differential Transducers (LVDTs). LVDT-1 and LVDT-5 were positioned at the mid-span between columns C-4 and C-5, and columns C-1 and C-2, respectively, while LVDT-3 was vertically placed at the location of column C-6 removal. The readings recorded by LVDT-3 were utilized in this study to plot the load-displacement curves for the two tested specimens. Additionally, two other transducers, LVDT-2 and LVDT-4, were employed to measure the horizontal displacements of Columns C-1 and C-5. These horizontal displacements were utilized to detect possible failure modes of the specimens, such as inward movement of the slab-column connection under tensile membrane forces in the slabs. A three-dimensional schematic view of the LVDT arrangement is presented in Figure 4.

To observe the load redistribution at large deformation stage, the bodies of five columns C-1 to C-5 were constructed using 168.3 mm diameter and 5 mm thick steel circular hollow sections (S355 grade), fully connected to the test specimens by four 18 mm diameter bolts passing through two 15 mm thick steel plates, and pin-connected to the laboratory strong floor. The steel hollow column body was equipped with four strain gauges positioned 250 mm away from the pin-end location. Internal forces in this section, which were later used to determine the axial forces and bending moments at the slab-column connection level, were calculated using the recorded steel strains and the cross-sectional properties of the hollow steel column, following the principle presented by Hieu *et al*. (2023) [5].

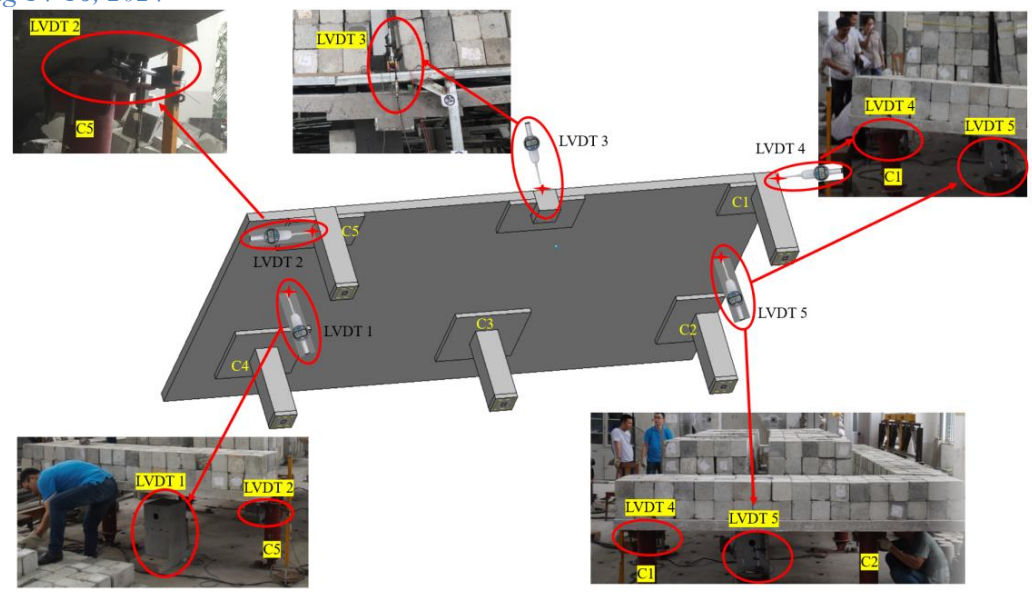

Figure 4: Three-dimensional schematic view of the LVDT arrangement [5]

2.3 BEHAVIOUR OF TEST SPECIMENS

During the test, a 5-minute interval was observed between consecutive loading steps to allow for stabilization of the specimen's deflection and observation of crack patterns. Readings from strain gauges mounted on the five hollow steel columns were automatically recorded by a data-logger TDS-530. For the MC specimen, 22 loading steps were carried out, while for the PC specimen, there were 18 loading steps. The total duration of each test was approximately 4 hours. Throughout the tests, the difference between the total applied load (on both the slab extension and testing area) and the total axial reactions from the five supporting columns was found to be less than 7%.

2.3.1. MC specimen

Crack pattern and collapse modes

Figure 5 depicts the crack pattern observed in the MC specimen, which exhibited symmetry about the line connecting Column C-3 and the C-6 position. Multi-cracks (marked as 1) on the bottom surface of the specimen initiated from the perimeter edge at a load of 6.0 kN/m² (including self-weight) and then propagated towards Columns C-2 and C-4 with increasing load. Concurrently, top cracks (marked as 2 and 3) emerged at almost the same loading step on both column capitals of Columns C-1 and C-5, as well as on the surrounding slabs. Additionally, top cracks (marked as 4) appeared at a load of 14 kN/m², subsequently delineating the boundary of the highly deflected central area as loading progressed.

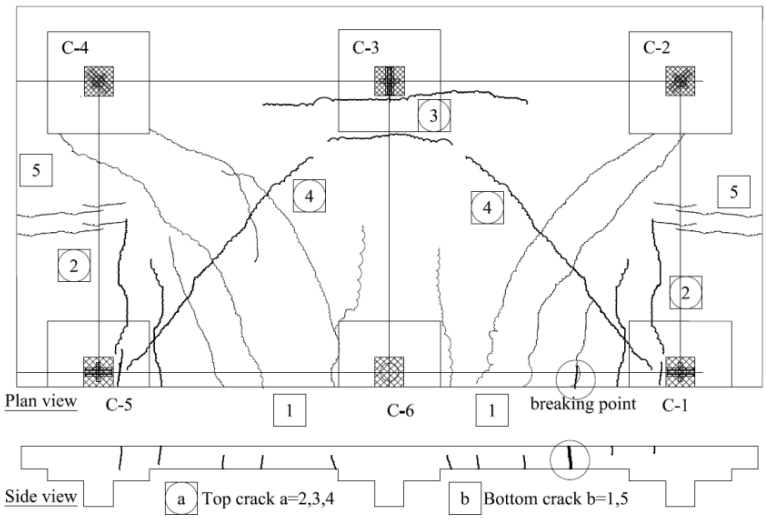

Figure 5: Crack patterns of MC specimen

At a loading step of 21.7 kN/m², the deflection of the central slab area, as measured by LVDT-3, exhibited instability, unlike at previous steps, and continuously increased, serving as a clear warning sign of imminent collapse. Eventually, the central slab area detached from the specimen at the breaking point near Column C-1, precipitated by a full-depth crack on the bottom surface of the specimen. At the moment of collapse, the vertical displacement measured at the C-6 position (by LVDT-3) reached 180 mm, equivalent to 9% of the length of a single slab panel.

Load-deflection curves

Figure 6(a) illustrates the relationship between the axial reaction forces in Columns C-1 to C-5, calculated using Equation (1) from strain gauge readings, and the vertical deflection at the C-6 position. The total concrete weight used in the MC test was approximately 184 kN (equivalent to 2300 cubes). As depicted in Figure 6(a), the highest proportion of the applied load was distributed to Column C-3, followed by Columns C-1 and C-5. In contrast, the lowest proportions were allocated to the two corner columns, C-2 and C-4. A slight discrepancy (less than 7%) between the axial reactions in Columns C-1 and C-5 was noticeable despite these values being identical due to the symmetrical loading condition and geometry of the test structure about the line connecting C-3 and C-6. This discrepancy could have resulted from the incorrect positioning of concrete piles during the test.

Figure 6(b) presents relationships between the uniform load applied to the slab panels and the vertical displacement measured in Column C-6 during the MC Test. The first curve represents the applied load obtained from actual loading steps, while the second curve depicts the applied load calculated from the obtained axial reaction forces. Both curves agree closely on several key experimental observations, including the initial appearance of cracks (marked as 1 in Figure 5) at a loading step of 6.0 kN/m², extensive cracking within the loading range of 10.0 kN/m² to 14 kN/m², and a prolonged plateau with minimal loading increase during the pre-collapse stage. The strong agreement between these two curves also demonstrates the reliability of the test

setup in simulating the complete collapse of the MC specimen, which occurred at a vertical displacement of 180 mm.

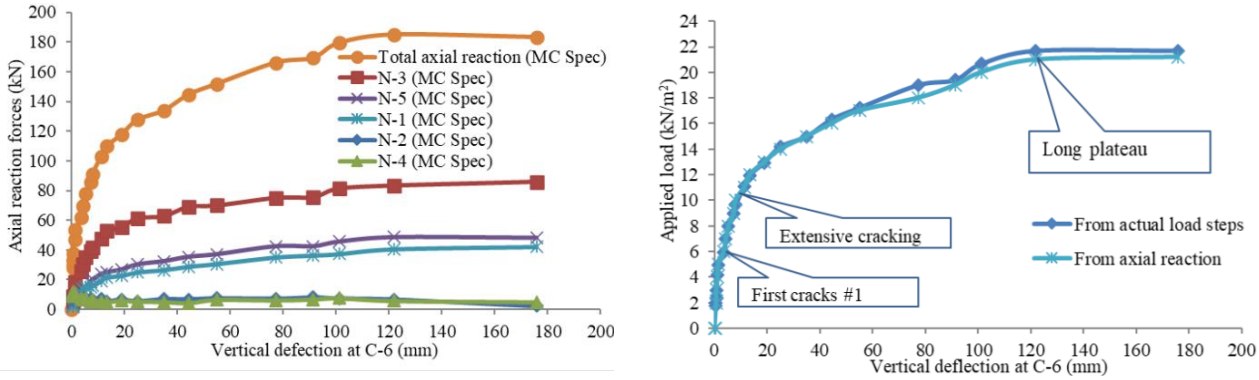

(a) Axial reaction forces in supporting columns (b) Load-vertical deflection curve (including self-weight)

Figure 6: Results of loading test on the MC specimen

2.3.2. PC specimen

Crack pattern and collapse modes

Figure 7 depicts the crack pattern and a front-view photo of the PC specimen at the final loading step of 18 kN/m² (including self-weight). The collapse of this specimen was attributed to a notable inward movement of the top of Column C-1. The vertical deflection at the C-6 position, measured just before collapse, was recorded at 175 mm, equivalent to 8.6% of the length of a single slab panel.

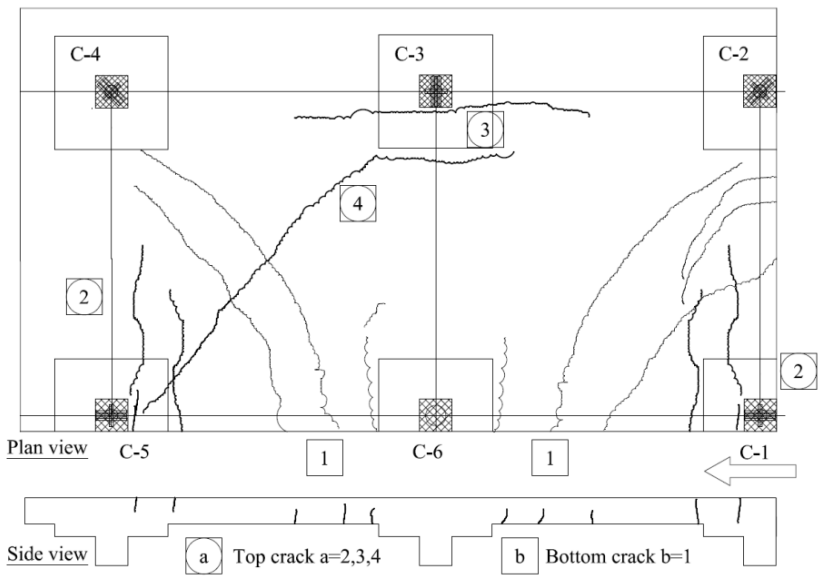

Figure 7: Crack patterns and collapsed shape of PC specimen

Load-deflection curves

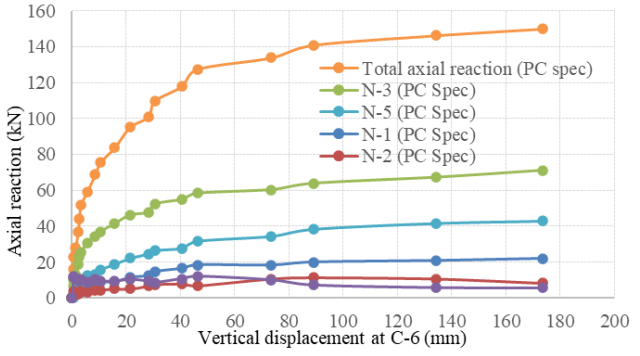

Figure 8: Varying axial force reactions in five columns in the PC specimen

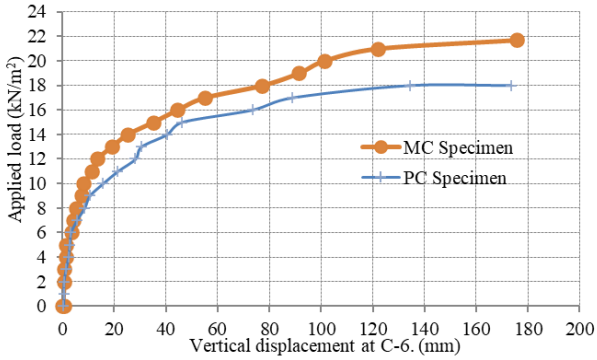

Figure 9: Load-displacement curves in two tests (including slab self-weight of 2 kN/m^2)

Figure 8 illustrates the fluctuating axial reaction forces in Columns C-1 to C-5 during the PC test. The total concrete weight in this test amounted to approximately 150 kN, with the highest proportion of applied load distributed to Column C-3 and the lowest proportions allocated to the two corner columns, C-2 and C-4. Conversely, the load proportion to Column C-5 was nearly double that of Column C-1, as depicted in Figure 8. The load-displacement curve of the PC specimen will be presented in the subsequent section.

3. DISCUSSION

3.1 STRUCTURAL BEHAVIOUR OF MC SPECIMEN COMPARED TO PC SPECIMEN

Figure 9 compares the relationship between the applied load (uniformly distributed) and vertical displacement (measured at the C-6 position) in the two tests. It is evident that the overall performance of the MC specimen surpassed that of the PC specimen in terms of both load-bearing and deformation capacities. The applied load on the MC Specimen was consistently greater than that on its counterpart at every loading step. The final values of applied load (and the corresponding deflection at C-6) for the MC specimen were 21.7 kN/m^2, approximately 120% of those for the PC Specimen. The superior performance of the MC specimen can be attributed to the slab extension along the line of columns C-1 and C-2, which provided additional flexural and in-plane lateral restraint, enabling further mobilization of flexural and tensile membrane actions in the right slab panel.

The failure mode observed in the PC specimen, characterized by the instability of Column C-1, is likely to instigate progressive collapse vertically in actual building structures, particularly when occurring at lower stories. Additionally, the presence of the slab extension played a crucial role in averting this failure mode, thereby confining the damaged area within a specific affected region, as demonstrated in the MC test (refer to Figure 5).

3.2 THE LOAD-CARRYING CAPACITY OF TEST SPECIMENS

Previous studies [2, 3, 11, 14, 15] have demonstrated that RC slabs primarily carry loads through flexural action at small vertical deflections. The flexural load-carrying capacity can be

accurately predicted using the yield-line approach, which involves positive yield lines traversing across the slabs and negative yield lines surrounding the slab edges. As deflections increase, along with a certain degree of in-plane lateral restraint of RC slabs, tensile membrane action (TMA) gradually replaces positive bending moments, resulting in a combination of flexural and tensile membrane actions to support applied loads. Consequently, the contribution of TMA to the overall load-carrying capacity of RC slabs can be estimated by comparing collapse loads with associated yield-line predictions. It should be noted that further mobilization of TMA often provides a greater load-carrying capacity, which is crucial in mitigating progressive collapse in flat slab building structures following a local punching failure.

Figure 10 illustrates two permissible yield-line mechanisms for the current test specimens. The first mechanism is associated with cracks developing from column capitals C-1 to C-5, while the second is associated with cracks extending into the column capitals. The mechanism that prevails will yield the lowest load prediction. Both mechanisms assume that all slab segments are rigid and only rotate along yield lines.

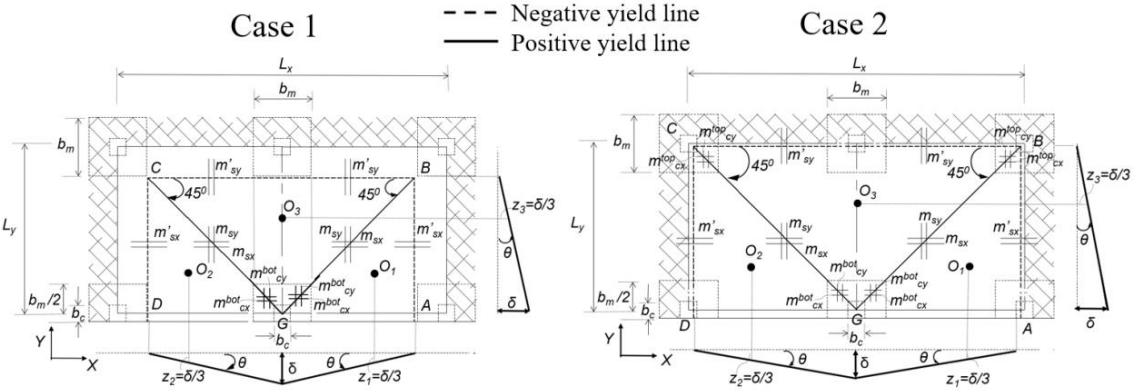

Figure 10: Admissible yield line mechanisms

The ultimate negative (positive) bending moment capacities of slabs and capital (per unit width) in the x- and y-direction are $m'_{sx}(m_{sx})$ and $m'_{sy}(m_{sy})$; $m^{top}{}_{cx}(m^{bot}{}_{cx})$ and $m^{top}{}_{cy}(m^{bot}{}_{cy})$, respectively. The overall dimensions in x- and y-direction are L_x and L_y, respectively.

The ultimate bending moment capacities per unit width of slabs, viz. m'_{sx}, m_{sx}, m'_{sy}, m_{sy} are given as:

$$m_s = A_s f_y \left(d_s - \frac{0.59 A_s f_y}{f_c^{'}} \right) \tag{1}$$

Where A_s is the tension reinforcement area per unit width of slabs, d_s is the effective depth of slabs.

The ultimate bending moment capacities per unit width of capitals, viz. $m^{top}{}_{cx}$, $m^{bot}{}_{cx}$, $m^{top}{}_{cy}$, $m^{bot}{}_{cy}$ are given as:

$$m_c = A_s f_y \left(d_c - \frac{0.59 A_c f_y}{f_c^{'}} \right) \tag{2}$$

Where A_c is the tension reinforcement area per unit width of capitals, d_c is the effective depth of capitals.

The yield-line capacity of case 1 can be determined using the virtual work approach based on the yield-line mechanism shown in Figure 8. The virtual work equation is written as:

$$\sum W_{yl}\Delta_i = \left[2m'_{sx}\left(L_y + \frac{b_c}{2} - \frac{b_m}{2}\right) + m'_{sy}\left(L_x - b_m\right) + 2m_{sx}\left(L_y - \frac{b_m}{2}\right) + m_{sy}\left(L_x - b_m\right) + \left(m_{cx}^{bot} + m_{cy}^{bot}\right)b_m\right]\theta \quad (3)$$

The left-hand side is referred to as the total external work done by the vertical load on each slab segment W_{yl} on the downward movement of its centroid Δ_i, and the right-hand side is the internal work done by positive and negative bending moments along the yield lines of the slab. Given a virtual displacement δ in the direction of loading at the removed column position, with $L_x = 2L_y = 2 \times 2.000$ mm, the external virtual work due to the uniform load W_{yl} can be calculated as follows:

$$\sum W_{yl}\Delta_i = 4w_{yl}\frac{L_x}{2}\frac{L_y}{2}\frac{\delta}{3} = \frac{w_{yl}\delta L_x L_y}{3} \quad (4)$$

Using the compatibility condition of deformation, $\theta = \frac{\delta}{L_y}$, one has

$$\frac{w_{yl}\delta L_x L_y}{3} = \left[2m'_{sx}\left(L_y + \frac{b_c}{2} - \frac{b_m}{2}\right) + m'_{sy}\left(L_x - b_m\right) + 2m_{sx}\left(L_y - \frac{b_m}{2}\right) + m_{sy}\left(L_x - b_m\right) + \left(m_{cx}^{bot} + m_{cy}^{bot}\right)b_m\right]\frac{\delta}{L_y} \quad (5)$$

Hence, the yield-line prediction is

$$w_{yl} = \frac{3\left[2m'_{sx}\left(L_y + \frac{b_c}{2} - \frac{b_m}{2}\right) + m'_{sy}\left(L_x - b_m\right) + 2m_{sx}\left(L_y - \frac{b_m}{2}\right) + m_{sy}\left(L_x - b_m\right) + \left(m_{cx}^{bot} + m_{cy}^{bot}\right)b_m\right]}{L_x L_y^2} \quad (6)$$

Similar, the yield-line capacity of case 2, is given as:

$$w_{yl} = \frac{3\left[2m'_{sx}\left(L_y + \frac{b_c}{2}\right) + m'_{sy}L_x + 2m_{sx}L_y + m_{sy}L_x + \left(m_{cx}^{top} + m_{cy}^{top} + m_{cx}^{bot} + m_{cy}^{bot}\right)b_m\right]}{L_x L_y^2} \quad (7)$$

Tables 2 and 3 present the calculated ultimate bending moments and yield loads predicted by Eqs. (6) and (7), respectively, corresponding to the two admissible mechanisms illustrated in Figure 10. The first yield line mechanism, yielding the lowest load prediction of 15.97 kN/m², is applicable to both test specimens. It is important to note that once the correct yield line mechanism is established, any other admissible yield line mechanisms with higher load predictions will not occur, as they do not satisfy the compatibility condition of deformation. Instead, tensile membrane action will occur within the slab body of the specimens.

Table 2. Ultimate bending capacity of slabs and beams of MC specimen (Eq. 1)

Case	Reinforcement Top layer (bottom layer)	A_s^{top} (A_s^{bot}) (mm²/mm)	b (mm)	$d_{s\text{-}ave}$ (mm)	f_y (N/mm²)	f'_c (N/mm²)	$m'_{sx,sy}$ ($m_{sx,sy}$) (kNm/m)
1	Φ6@80&160 (Φ6@110&220)	0.2653 (0.193)	1000	67	380	20	6.454 (4.755)

2	Φ6@80&160 (Φ6@110&220)	0.2653 (0.193)	1000	67	380	20	6.454 (4.755)

Table 3. Yield line predictions for two admissible mechanisms in Figure 8 (Eqs. 6 to 7)

Case	L_x (L_y) (m)	b_m (m)	b_c (m)	$d_{c\text{-}ave}$ (mm)	A_c^{top} (A_c^{bot}) (mm²/mm)	$m_{cx,cy}^{top}$ ($m_{cx,cy}^{bot}$) (kNm/m)	W_{yl} (kN/m²)
1	4.0 (2.0)	0.7	0.2	107	0.354 0.177	14.253 7.261	15.966
2	4.0 (2.0)	0.7	0.2	107	0.354 0.177	14.253 7.261	22.544

Table 4 compares the peak values of test loads and the corresponding yield loads of both specimens. It is evident that both specimens had progressed well into the tensile membrane stage. The contributions of TMA to the overall load-carrying capacities of the MC and PC specimens at the final loading steps were 11% and 26%, respectively.

Table 4. Comparison of the actual test loads and corresponding yield loads of test specimens

Specimen	w_{yl} (kN/m²)	w_{actual} (kN/m²)	$(w_{actual} - w_{yl})/ w_{actual}$
PC	15.97	18	11%
MC	15.97	21.7	26%

The shift of the load-carrying mechanism from flexure to combined flexure-tensile membrane action, which has been experimentally evidenced, raises the question of how much this shift affects load redistribution. Figures 11(a) and 11(b) compare the percentage of load portions redistributed to Column C-3 (denoted as N-3), to the two edge columns (N-1 + N-5), and to the two corner columns (N-2 + N-4) in the MC and PC tests, respectively.

As depicted in Figure 11(a), a significant portion of the applied load, up to 45%, was redistributed to Column C-3, indicating a possibility of the subsequent punching shear failure occurring at this column capital. The percentage of the total applied load distributed to the two edge columns remained stable at approximately 45%. A notable observation is a low percentage distributed to the two corner columns, C-2 and C-4, which is less than 10%. A similar tendency in load redistribution was observed in the PC Specimen, as shown in Figure 11(b).

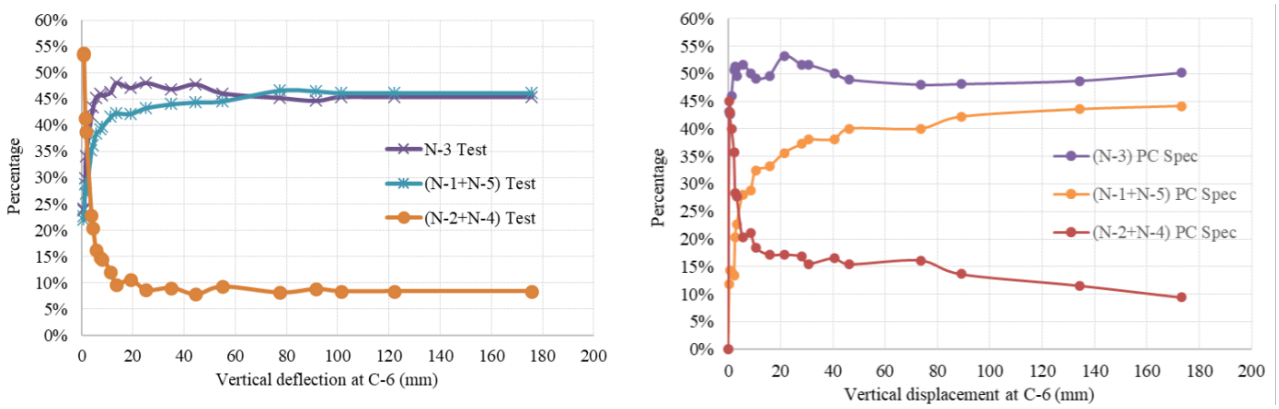

(a) MC Specimen (b) PC specimen

Figure 11: Load-redistribution to surrounding columns in MC and PC Tests

3.3 EFFECTS OF COLUMN CAPITAL ON THE COLLAPSE BEHAVIOUR OF FLAT SLAB STRUCTURES

To evaluate the effect of column capitals on the collapse behavior of flat slab structures, experimental observations of specimens MC (and PC) were compared with two others, namely SP-1 (and SP-3), which had the exact geometrical dimensions, reinforcement detailing, boundary, and testing conditions, but lacked column capitals. Complete test data of specimens SP-1 and SP-3 have been reported in Tran et al. (2018) [13]. Figures 13(a) and 13(b) present photos of Specimen SP-3 at the last loading step and SP-1 before being removed from the testing site, respectively. As observed in the images, both test specimens collapsed due to punching shear failure at Columns C-1 and C-5. In Figure 12(a), the angle of cracks that appeared on the edge of SP-3 near Column C-5 was in the opposite direction of shear cracks, indicating that the punching shear failure resulted from the combined action of shear and bending moments in both directions, rather than shear action alone. Meanwhile, in the two current tests, the extent of damage at the slab areas on top of Columns C-1 and C-5 was effectively limited due to the presence of column capitals, as shown in Figures 6(a) and 8(c).

(a) Specimen SP-3

(b) Specimen SP-1

Figure 12: Photos of two compared specimens SP-3 and SP-1

It was anticipated that the column capitals could enhance the flexural stiffness of the slab-column strips running along Columns C-1 to C-2 and C-4 to C-5. Figures 13(a) and 13(b) compare the varying vertical displacement recorded by LVDT-5 to the applied load in two specimens: MC versus SP-3 and PC versus SP-1. As depicted in Figure 13, the presented curves exhibited similar shape properties, including an almost linear pattern when the applied load was less than approximately 14 kN/m² (12 kN/m²) for MC and SP-3 (for PC and SP-1), followed by a moderately nonlinear segment, and finally, a very steep segment in the last few loading steps. However, the curves in the MC and PC tests were only slightly higher than those in the SP-3 and SP-1 tests, indicating insignificant effects of the column capitals on the flexural stiffness of the surrounding column strips.

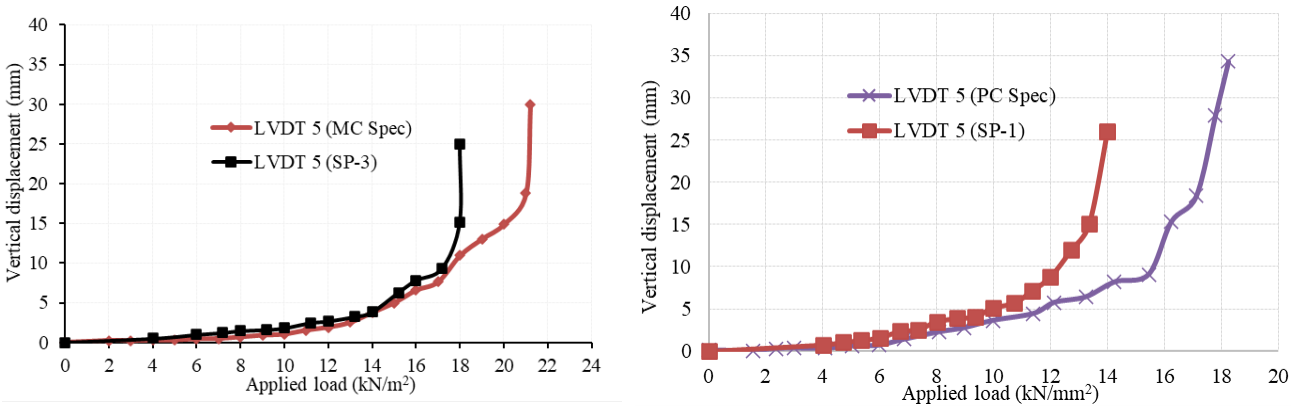

(a) (b)

Figure 13: A comparison of varying vertical displacement measured by LVDT-5

The load-displacement curves of these two pairs of specimens are also compared in Figures 14(a) and 14(b). With the presence of column capitals, the MC and PC specimens could sustain greater loads at further deflections compared to their counterparts, which prematurely collapsed due to punching shear failure. The collapse loads in the MC (PC) tests were respectively 20% (28%) higher than those in the SP-3 (SP-1) tests. Furthermore, the deformation capacities of the two specimens with column capitals were 224% (190%) higher than those without column capitals.

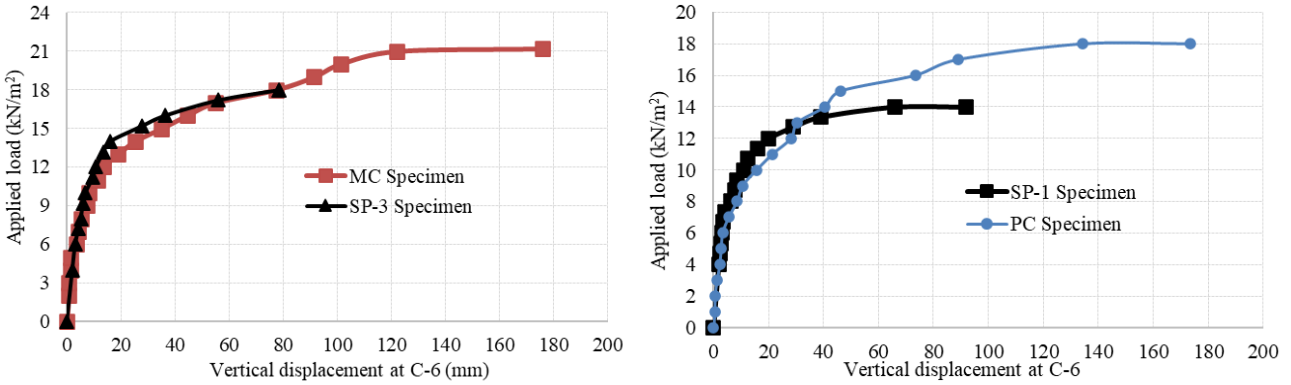

(a) (b)

Figure 14: A comparison of load-displacement curves of Specimens w/o column capital

4. CONCLUSIONS

This paper presents an experimental investigation of the collapse behavior of flat slab structures with column capitals. Two 1/3-scaled specimens were subjected to complete collapse by uniformly distributed loads simulated by eight separate piles of concrete cubes placed on the specimens. Two accidental scenarios were selected in this study: one where a loss of vertical support occurs at the mid-span column location, and the other at the penultimate column location. Based on the experimental observations, several conclusions are drawn:

- The collapse behavior of flat slab structures exhibits significant ductility. The vertical deflections of the two specimens reached approximately 9% of a single span length. The collapse loads exceeded corresponding yield-line predictions by 26% and 11% for the MC and PC specimens, respectively, indicating substantial mobilization of tensile membrane action in the affected slab panels.
- Comparing experimental results between specimens with and without column capitals reveals that column capitals play a crucial role in enhancing the collapse behavior of flat slab structures. The primary contribution of column capitals is seen in their ability to strengthen the structure, delaying or preventing punching shear failure on the top of Columns C-1 to C-5. Consequently, the structures exhibit increased capacity to deflect and carry greater applied loads.
- It is also observed that there is a nonlinear load redistribution among the columns surrounding the affected slab panels at large deformations. The majority of the applied load on the two affected panels is redistributed to the three columns nearest to the column experiencing local failure.

Acknowledgments

The study presented in this paper was financially supported by the National Foundation for Science and Technology Development (NAFOSTED), Vietnam, through Grant #107.01-2020.16. The financial supports are greatly appreciated.

REFERENCE

[1] Park TW. Inspection of collapse cause of Sampoong Department Store. Forensic science international. 2012;217:119-26.
[2] Dat PX, Tan KH. Experimental study of beam–slab substructures subjected to a penultimate-internal column loss. Engineering Structures. 2013;55:2-15.
[3] Dat PX, Tan KH. Experimental response of beam-slab substructures subject to penultimate-external column removal. Journal of Structural Engineering. 2015;141:04014170.
[4] Nguyen VH, Yu J, Tan KH. Component-based joint model for RC frames with conventional and special detailing against progressive collapse. Structures: Elsevier; 2022. p. 820-37.
[5] Hieu NT, Tan NN, Dat PX. Experimental study on the collapse response of flat slab structures with drop panels under gravity loading condition. Structures: Elsevier; 2023. p. 104855.
[6] Do AK, Nguyen TN, Tran CQ, Nguyen HT, Pham DX. Experimental and numerical investigations on the collapse behaviour of RC flat slab structures. Asian Journal of Civil Engineering. 2021;22:1143-55.
[7] Trung HN, Truong TN, Xuan DP. Effects of reinforcement discontinuity on the collapse behavior of reinforced concrete beam-slab structures subjected to column removal. Journal of Structural Engineering. 2019;145:04019132.
[8] Hawkins NM, Mitchell D. Progressive collapse of flat plate structures. Journal Proceedings1979. p. 775-808.
[9] Melo G, Regan P. Post-punching resistance of connections between flat slabs and interior columns. Magazine of Concrete Research. 1998;50:319-27.
[10] Qian K, Li B. Load-resisting mechanism to mitigate progressive collapse of flat slab structures. Magazine of Concrete Research. 2015;67:349-63.
[11] Russell J. Progressive collapse of reinforced concrete flat slab structures: University of Nottingham; 2015.
[12] Kokot S, Anthoine A, Negro P, Solomos G. Static and dynamic analysis of a reinforced concrete flat slab frame building for progressive collapse. Engineering Structures. 2012;40:205-17.
[13] Cuong TQ, Linh NN, Hung HM, Hieu NT, Dat PX. Experiments on the collapse response of flat slab structures subjected to column loss. Magazine of Concrete Research. 2019;71:228-43.
[14] Nguyen VH, Tan KH. Progressive collapse behaviour of advanced precast reinforced concrete joints with headed bars and plastic hinge relocation. Engineering Structures. 2023;293:116603.
[15] Nguyen VH, Tan KH. Progressive collapse behaviour of earthquake-damaged interior precast concrete joints with headed bars and plastic hinge relocation. Engineering Structures. 2024;306:117817.

EXPERIMENTAL INVESTIGATION OF UNBONDED AND BONDED POST-TENSIONED PRECAST CONCRETE FRAMES SUBJECT TO A PENULTIMATE COLUMN LOSS

Hai-Rong Shi[1], Chun-Lin Wang[2], Jun Yu[3], and Shaoping Meng[4]

[1] Doctoral student, Key Laboratory of Concrete and Prestressed Concrete Structures of the Ministry of Education, Southeast University, Nanjing 210096, China, 230218113@seu.edu.cn.

[2] Professor, Key Laboratory of Concrete and Prestressed Concrete Structures of the Ministry of Education, Southeast University, Nanjing 210096, China, chunlin@seu.edu.cn.

[3] Professor, Affiliation Engineering Research Center of Safety and Protection of Explosion & Impact of Ministry of Education at Southeast University, Nanjing 210096, China, junyu@seu.edu.cn.

[4] Professor, Key Laboratory of Concrete and Prestressed Concrete Structures of the Ministry of Education, Southeast University, Nanjing 210096, China, cardoso_meng@sina.com.

Corresponding Author: Hai-Rong Shi, PhD student
School of Civil Engineering, Southeast University, Nanjing, Jiangsu Province, China, 210096
Email: 230218113@seu.edu.cn

ABSTRACT

Being a critical scenario in extreme events such as blast attacks, the progressive collapse of structures is often examined through alternate load path approach. This study, ignoring the blast magnitude, conducted push-down tests on five substructures: four post-tensioned precast concrete (PC) specimens and one reinforced concrete (RC) specimen. All substructures were designed with comparable seismic resistance. The tested PC specimens comprised unbonded and bonded substructures (UPC and BPC), a bonded substructure with low effective prestress (BPCL), and an unbonded substructure with steel angles (UPCA). The findings indicated that PC specimens without angles displayed weaker beam action, reducing the first peak load compared to RC (48.7 kN). In contrast, the post-tensioned strands markedly improved structural integrity, yielding a remarkable 89.8% increase in ultimate load resistance. Compared with UPC, BPC showed a stronger beam action but notably inferior ductility, while BPCL balanced the resistance and deformation well, demonstrating the highest load capacity among them. Additionally, the steel angles proved effective in enhancing overall performance throughout the entire loading history. On this concept, an improved hybrid joint (i.e., BPC with external steel angles) was recommended to improve the robustness against progressive collapse.

Keywords: *Progressive collapse, Post-tensioned precast concrete, Bond slip relationship, Ductile beam-column joint.*

1. INTRODUCTION

The initial damage of columns caused by blast attacks, fires or other accidents may trigger disproportionate collapse of buildings, known as progressive collapse. The alternate load path (ALP) method has been utilized in several design guidelines[1, 2] to assesses the progressive collapse resistance of structures. It determines the structural resistance of damage spreading by evaluating how well the structure can sustain gravity loads in column loss scenarios.

In the context of the ALP method, a thorough and methodical exploration has been undertaken regarding the collapse resistance of reinforced concrete (RC) frame structures[3-6]. These investigations took into account a range of critical factors such as the positions of the removed column[7, 8], the effect of slab and infilled walls [9, 10], and boundary conditions[11], offering a comprehensive understanding of structural behaviour in the face of such challenges.

On the other hand, precast concrete frame structures are becoming more and more popular with the development of construction technology and environmental sustainability requirements. Among these, post-tensioned precast concrete (PC) frames have emerged as a focal point owning to the fast-track construction. The PC frame structure was proposed in the Precast Seismic Structural Systems (PRESSS) project, where precast concrete components are press-bound by unbonded post-tensioned strands [12]. Generally, additional energy dampers are typically attached at the beam-column joints to improve the energy dissipation under earthquakes [13-16]. What's more, bonded PC frames, i.e., PC frames with bonded post-tensioned strands, are proposed and widely constructed in Japan, which is in more favour of corrosive and progressive collapse resistance [17]. Such bonded PC frames have withstood multiple earthquakes with minimal structural damage [18].

Several studies were carried out to investigate the resistance of PC frames to progressive collapse. Qian et al. [19, 20] and Zhao et al. [21] conducted both quasi-static and dynamic tests on the unbonded PC beam–column assemblies and the effects of the position of the removed column and the distribution of vertical loads were also considered. Li et al. [22] carried out experimental studies on the progressive collapse of unbonded PC frames with infill walls.

However, less research has been focused on the collapse performance of bonded PC frames. Besides, a comparison in the collapse resistance between PC frames and RC frames with a similar seismic design is still required. This paper contributes to filling the research gap by investigating the collapse performance of bonded PC frames and providing a comparative analysis of collapse resistance between PC and RC frames with similar seismic designs. Except for the bonding condition of strands, the influences of externally attached steel angles and the tendon profiles were also considered.

2. EXPERIMENTAL PROGRAM

2.1. Specimen design

The prototype building is a six-storey frame with a beam span of 10.5 m and located in a fortification intensity VII area with a soil site condition of II according to Chinese seismic design code [23]. The peak ground motion is 0.1g with a 10% probability of exceedance in a

50-year period. A site class of II is corresponding to the site class C_{US} of America code [24]. The design live load and the dead load are 2.0 kPa, and 5.5 kPa, respectively.

Table 1 summarizes the five 1/3 scaled substructure specimens, including one reinforcement concrete (RC) specimen and four post-tensioned precast concrete (PC) specimens. The four PC specimens can be categorized into unbonded and bonded PC groups, which is identified with U and B, respectively. Specimen UPC and BPC have the identical reinforcement details except for the duct grouting for BPC. Different from UPC, specimen UPCA has a hybrid beam-column joint with post-tensioned tendons and external top-seat angles at the beam end. Additionally, specimen BPCL has a lower effective prestress than BPC, meanwhile the tendon profile of BPCL is properly designed to meet the serviceability and strength requirements.

Table 1. Test matrix

Specimens	Post-tensioned strand		Longitudinal reinforcement in the beam				Yield moment of the beam end	
			At the end		Mid-span			
	Nominal diameter (mm)	Effective prestress (MPa)	Top	Bottom	Top	Bottom	Hogging (kN·m)	Sagging (kN·m)
RC	-	-	4D10	2D10	2D10	2D10	28.6	14.8
UPC	15.2	1100	2D10	2D10	2D10	2D10	19.4	19.4
UPCA	12.7	1100					21.9	21.9
BPC	15.2	1100					19.4	19.4
BPCL	15.2	750					18.2	8.2

Figure 1 shows the detailing of tested specimens. Each specimen consisted of two side columns, two beams and one middle column stub. The beams had a cross section of 150 mm times 300 mm and a clear span of 3250 mm. The columns had a 250 mm square cross section. The middle column stub represented a failed penultimate column and restrained to move along its longitudinal axis, while the side column was pinned at each end to simulate the boundary conditions of an exterior column under the column-removal scenario.

As shown in **Figure 1**(a), specimen RC was reinforced with four D16 longitudinal rebars in each column and there were four D10 longitudinal rebars throughout the two-span of beam and two additional D10 longitudinal rebars at each beam end to counteract the hogging moment.

With regards to PC specimens, the columns and beams were precast and fabricated after placement. To address the interface gap between these precast components, a grouted layer with a thickness of 10mm was cast-in-site, ensuring a solid connection. All the precast columns had the same reinforcement as that of RC, and the precast beams had four D10 rebars, as shown in **Figure 1**(b). For specimens UPC and BPC, the precast members were connected by a straight D15.2 steel strand along the beam central line only. For specimen UPCA, two steel angles were attached across the joined interface and accordingly, the employed strand was 12.7 mm in the nominal diameter. Specimen BPCL had a curved tendon profile, so that the applied prestress could be lower than BPC.

In spite of the differences in the configuration, all the specimens were expected to have a similar seismic resistance, but specimen BPCL was slightly weaker. The calculated yield moment of the critical cross section for each specimen has been also provided in **Table 1**.

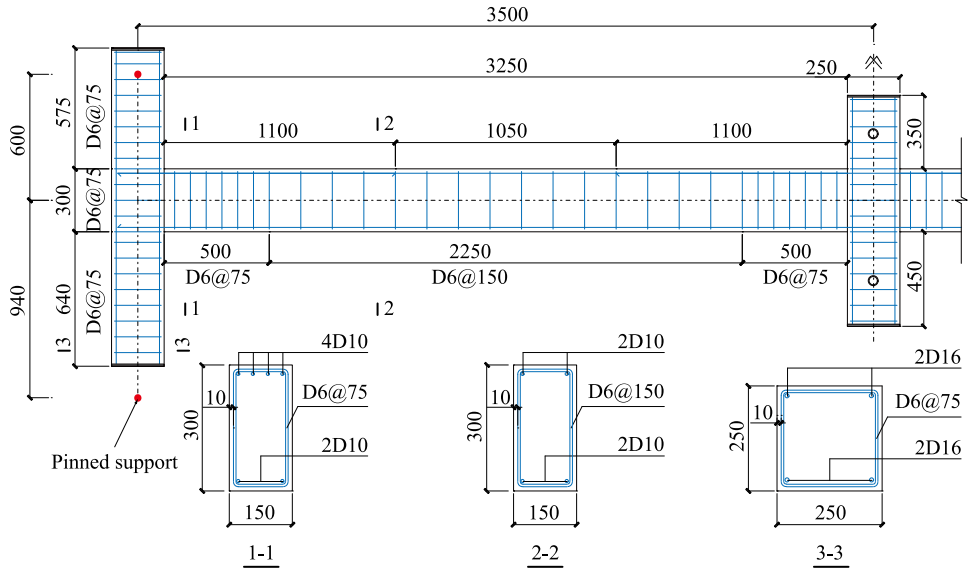

(a) Specimen RC

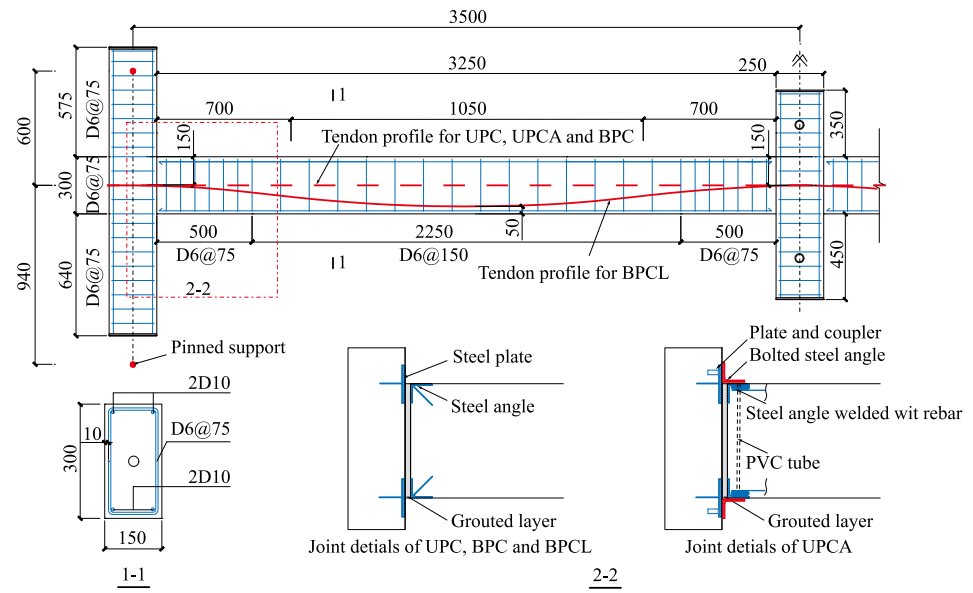

(b) PC specimens

Figure 1. Dimensions, reinforcements, and boundary conditions of the specimens (unit: mm).

2.2. Material properties

Table 2 lists the material properties of reinforcing bars and steel strands. For each type of reinforcement, the identifier is distinguished with the number following D, which refers to the nominal diameter.

As for the concrete, the mean values of compressive strength f_{cu} was characterized on three 150 × 150 × 300 mm cuboid specimens, whereas the cubic compressive strength f_c was characterized on six 150 × 150 × 150 mm cubes. The measured f_{cu} and f_c were 51.96 MPa and 38.01 MPa, respectively.

Table 2. Material properties

Type	Elastic modulus (GPa)	Yield stress (MPa)	Strain hardening strain (%)	Ultimate stress (MPa)	Ultimate strain (%)	Breaking elongation (%)
D6	200.05	511.08	-	621.30	9.03	12.11
D10	194.48	433.62	1.83	608.23	16.85	21.03
D16	204.96	411.25	1.37	615.53	18.23	24.06
D15.2	196.13	1812.13	-	2107.64	-	5.10
D12.7	198.22	1952.05	-	2352.67	-	5.86

2.3. Test setup

Figure 2 shows the test setup. The substructure specimen stood with two side columns on two pin bearings, where the shaft was a load pin. Two anti-slip plate were bolted on the upper plate to avoid the unexcepted movement of the column foot. Besides, the upper plate was connected to a reaction plate by four high-strength steel rods, so that the compressive load could be applied by a jacket on the column. The top of the side column was restrained horizontally by a threaded rod with a compressive and tensile load cell which was connected to the reaction wall or the A-frame.

The middle column was located a sufficient distance above the ground, allowing the potential drop induced by the column removal. There was a transverse and rotational restraint instrument surrounding the middle column to force it moving along its central axis. What's more, the middle column was initially hung on the restraint instrument by thread rods so that the column could be released smoothly after weights were hung beneath the beam. The total applied weight was 4600 kg. The weight-induced vertical load on the middle joint was measure by two donut load cells.

After the weight was applied and the middle column is released, the MTS actuator would further apply the vertical load on the middle column until the specimen failed or the displacement of the middle joint reached 650 mm (equals 0.2 times the clear span of the beam). The loading process was displacement controlled with a rate of 0.1 mm/s. The displacement of the middle joint was measured by two laser displacement transducers and obtained as the mean value. Furthermore, the tensile force in the strand was measured by a donut load cell at each anchorage end.

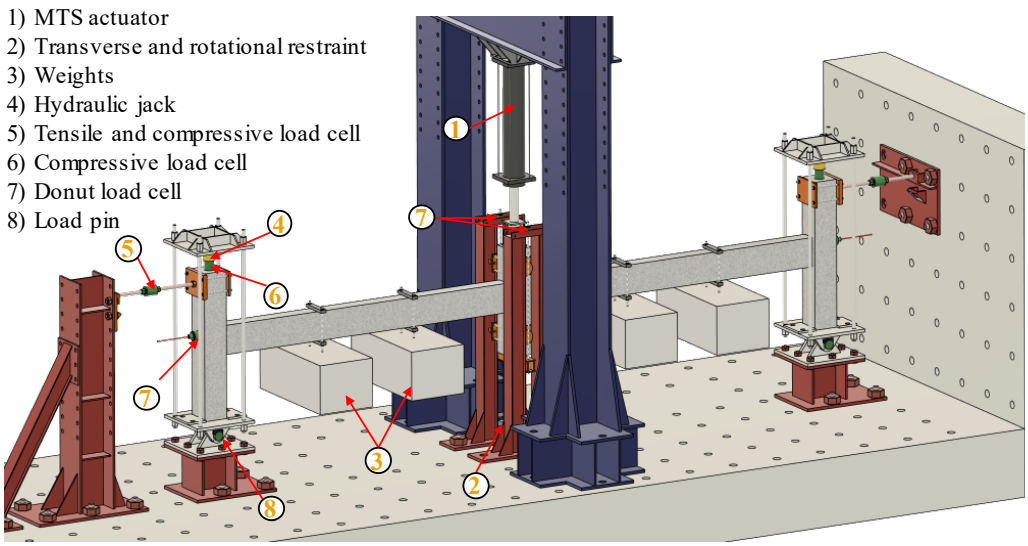

Figure 2. Test setup.

3. Test results and discussions

3.1. Failure modes

Figure 3 shows the failure modes of specimen RC. When the substructure lost the bearing capacity totally, the catenary action was the dominant resistance mechanism. The flexural cracks had occurred uniformly throughout the beam and several flexural cracks occurred at the inner side of the side column. Besides, the severe damage was concentrated on the beam-column interfaces. It was observed that all the tensioned rebars were broken near the right joint.

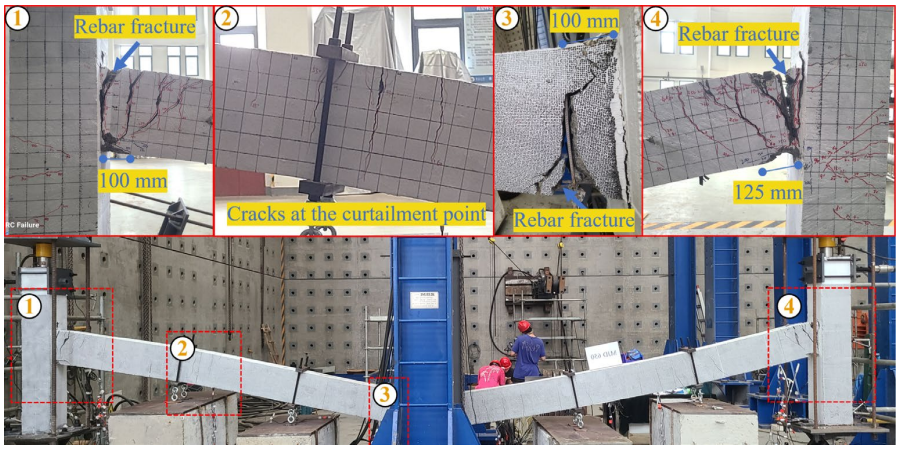

Figure 3. Failure modes of specimen RC.

Figure 4 shows the failure modes of specimens UPC and UPCA. At the compression arch action, the beam corner was compressed heavily, however the compression damage was in a moderate level owing to the strengthening of embedded steel angles. At the catenary action,

the post-tensioned strand and external steel angles transferred the tie forces efficiently, and severe flexural damages were observed at the side column. Due to the discontinuance of longitudinal rebars in UPC, the primary portion of the precast beam remained intact during the entire loading process. The tie forces relied on the unboned strand, two wires of which were broken at the middle joint displacement (MJD) of 632 mm. For specimen UPCA, the external steel angles exerted the tensile load and bending moment on the precast beam. A uniform distribution of cracks was also observed in tests. However, the over-strength of steel angles had induced unexpectedly high shear forces on high-strength bolts, resulting in the premature anchorage failures.

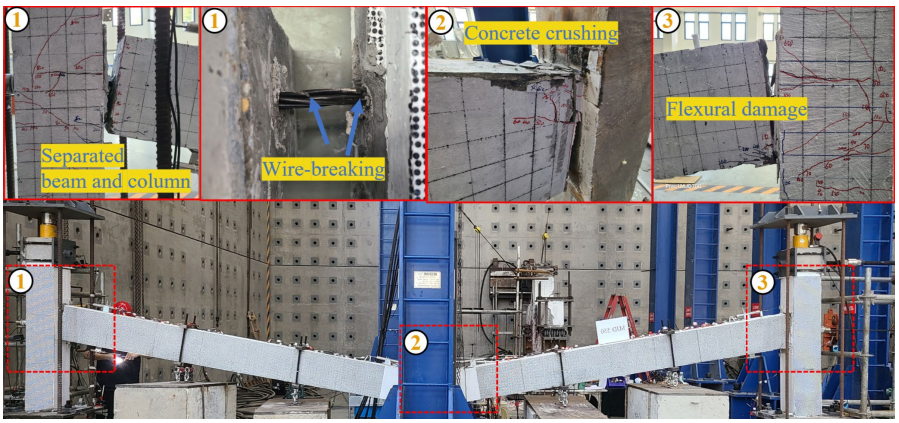

(a) UPC

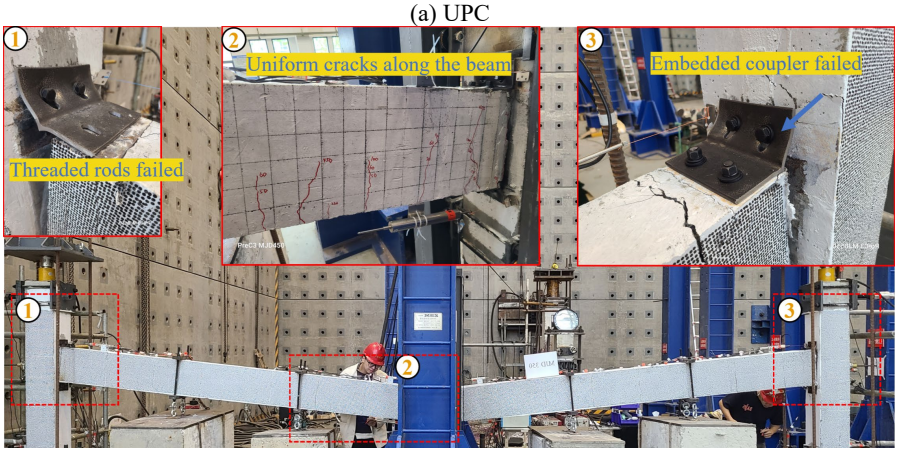

(b) UPCA

Figure 4. Failure modes of unbonded specimens.

Figure 5 shows the failure modes of specimens BPC and BPCL. The deformation of specimen BPC was quite similar to UPC except for the total failure of the left side joint. As shown in **Figure 5**(a), the gap-opening between the precast beam and column grown unstoppably. This could be caused by the bond degradation between the strand and duct after wire ruptures. However, the other portion of the substructure still remained an integrator to bear the applied load, indicating the high robustness of bonded PC frames. In **Figure 5**(b), specimen BPCL was

designed with a lower prestress in strand and the premature failure of joint was prevented successfully. The bonded strand remained reliable even at the MJD of 650 mm.

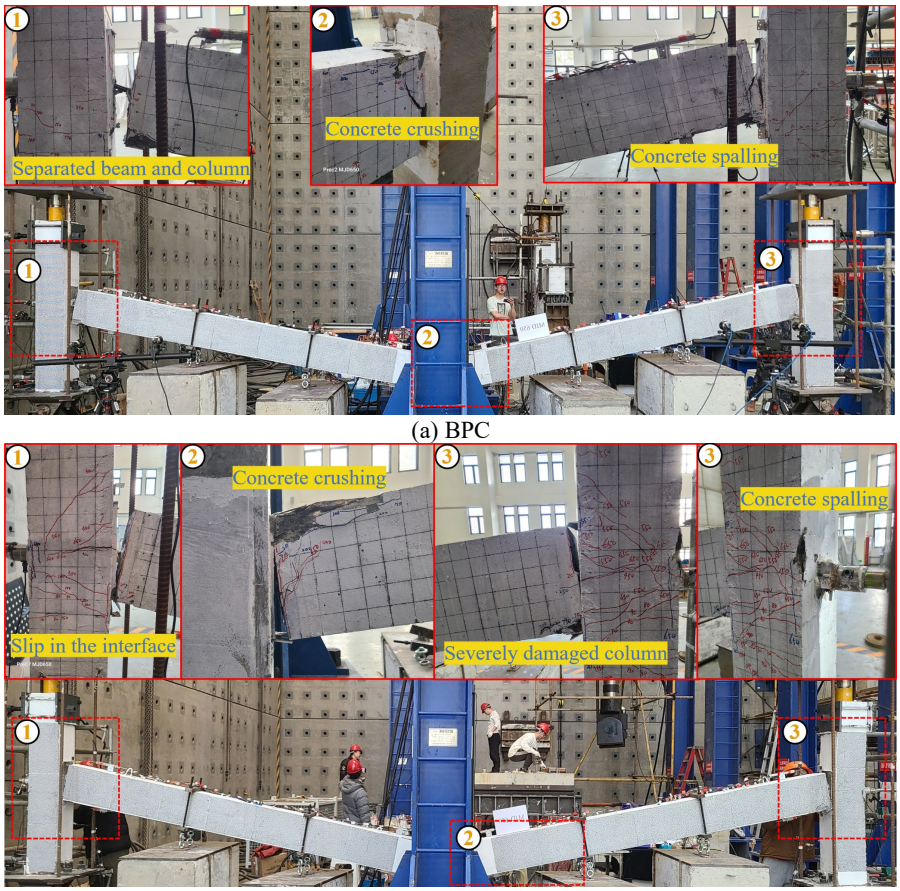

Figure 5. Failure modes of bonded specimens.

3.2. General structural behaviours

Figure 6 depicts the overall structural behaviours of all the tested specimens in terms of the vertical and horizontal resistance. **Figure 6**(a) shows the relationship between applied load on and displacement of the middle joint, which is denoted by MJF and MJD, respectively. **Figure 6**(b) shows the total horizontal reaction force, which is obtained as the sum of the measured horizontal reactions at the top and bottom of the side column.

It can be found that five specimens had a similar trend in the development of MJF, indicating the effect of beam action, compression arch action, and catenary action. The compression arch action and catenary action is characterized by the significant horizontal compression and tension reaction, respectively. MJF reached the first peak at the compression arch action, and then decreased gradually with the increase of MJD until the sufficient development of the catenary action. Further increase in MJD led to rapid growth in tension reaction, resulting in higher vertical resistance until MJF reaches the ultimate load, typically marked by rebar rupture

or wire-breakage in strands. Specimen UPCA displayed slight decreases in MJF at the MJD around 550 mm due to anchorage failure of steel angles.

Specifically, as shown in **Figure 6**(a), specimen RC had the strongest vertical resistance at the beam action and compression arch action because the RC beam was designed with a higher flexural resistance at the yield limit state. Similarly, specimen UPCA had a higher resistance than other PC specimens at the compression arch action due to the over-strength of steel angles. Conversely, specimens RC and BPC had much worse vertical resistance at the catenary action. This was caused by the total failure of rebars or strands in tension as evident from the horizontal reaction and the measured tensile force in the strand (in **Figure 7**). The other two specimens, UPC and BPCL, had the almost identical structural responses in terms of MJF and horizontal reactions.

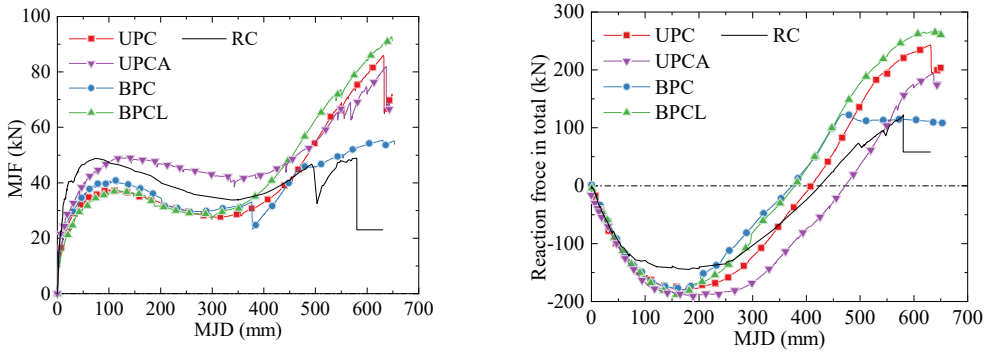

(a) Applied load on the middle joint versus MJD

(b) Total horizontal reaction force versus MJD

Figure 6. General structural behaviors of the five specimens.

3.3. Responses of strands

Figure 7 shows the tension force in the strand, which was obtained as the measured anchorage force at the side column. The pre-tensioning force in UPC, BPC, and BPCL were 153 kN, 145 kN, and 114 kN, respectively, where the steel strand was 15.2 mm in the nominal diameter. The pre-tensioning force in UPCA was 120 kN that had a D12.7 steel strand. The maximum tensile force in UPC, BPC, BPCL, and UPCA were 296 kN, 275 kN, 292 kN, and 226 kN, respectively. It can be found that the tension in both bonded and unbonded strands could still maintained after damages occurred. For example, the tensile force of the strand experienced a sharp decrease from 296 kN to 235 kN due to wire ruptures and then stabilized, maintaining a tension of 235 kN in the further loading. Besides, the comparison between UPC and BPCL revealed that bonded strands exhibited similar responses with unboned ones in PC frames except for the slightly faster growth in tension. This is mainly because the short beam span facilitated the tension stiffness of the unbonded strand which could be approaching the bonded cases. What's more, the deformation capability of bonded PC joints could be comparable to unbonded PC joints by properly determining the prestress. According to several related research [18], it was primarily recommended that he prestress level of bonded strands can be half of the yield strength of strands.

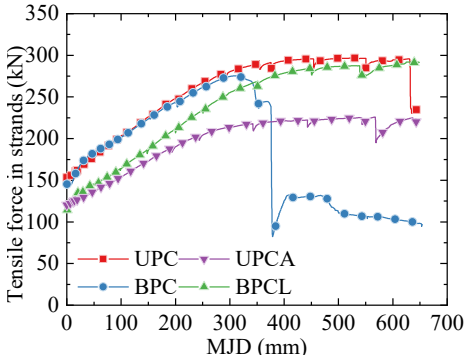

Figure 7. Tensile force in the strand versus MJD.

4. SUMMARY OF MECHANISM PROPERTIES

Table 3 summarizes the key structural responses of substructure specimens. The dynamic performances were also provided according to quasi-static responses by single-degree-of-freedom models and capacity curve method [25], and expressed as,

$$P_{\mathrm{d}}(u_{\mathrm{d}}) = \frac{1}{u_{\mathrm{d}}} \int_0^{u_{\mathrm{d}}} P_{\mathrm{qs}}(u)\mathrm{d}u \tag{1}$$

Where $P_{\mathrm{d}}(u_{\mathrm{d}})$ is the capacity function, and $P_{\mathrm{qs}}(u)$ is the quasi-static response at the displacement demand u.

According to the prototype building design, the yield lateral resistance of RC substructure was similar to PC ones. On this basis, the PC specimens had an average 15.8% decrease in the first peak load compared to RC (48.7 kN) and a remarkable increase up to 89.8% in the ultimate load than RC (48.9 kN), as listed in **Table 3**.

Table 3. Mechanism properties of tested specimens

Specimen	Critical disp. (mm)		Critical load (kN)		Max. horizontal force (kN)	Max. dynamic resistance (kN)
	First peak load	Ultimate load	First peak load	Ultimate load		
RC	80.2	580.0	48.7	48.9	-144.5	44.4
UPC	100.3	632.9	37.4	86.1	243.6	42.0
UPCA	138.9	637.3	49.0	82.0	194.5	49.3
BPC	110.7	628.8	40.7	55.3	-179.9	38.1
BPCL	118.7	648.1	37.2	92.8	266.5	44.9

Figure 8 illustrates the dynamic resistance of tested specimens. In terms of the dynamic collapse responses, the five specimens exhibited a similar dynamic load capacity around 40 kN, except for UPCA. The peak dynamic resistance of RC substructure occurred at the compressive

arch action due to the insufficient deformation capacity of rebars. For PC specimens, the dynamic resistance relied on the catenary action and could further increase with MJD increasing. The differences between quasi-static and dynamic responses indicated that the PC specimens were more flexible under the column removal scenario than RC substructures, mitigating their dynamic resistance.

Comparing UPCA and UPC, it was found that the substructure with external steel angles exhibited significantly higher dynamic resistance at the transition from compressive arch action to catenary action. This is primarily attributed to the fact that steel angles typically possess a much higher ultimate tensile strength than their yielding strength and had more tensile deformation than the post-tensioned strand at the center of cross section. On the other hand, the use of bonded strands had been shown to enhance the dynamic response by increase the stiffness of substructure, as evidenced by the dynamic load capacity of BPCL (44.9 kN) being greater than UPC (42.0 kN). Therefore, it was recommended to utilize bonded post-tensioned beam-column joint with external steel angles in PC frames to reduce the collapse risk.

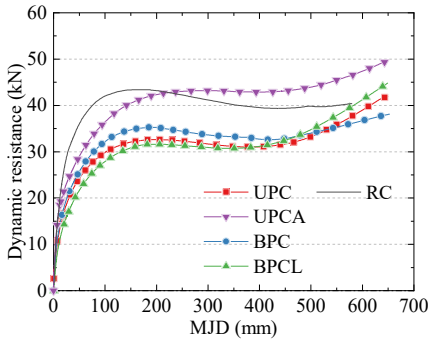

Figure 8. Dynamic load resistance versus MJD.

5. CONCLUSIONS

This paper conducted quasi-static tests on the performances of four post-tensioned precast concrete (PC) substructure specimens and one reinforced concrete (RC) substructure specimen under a penultimate column loss scenario. The main conclusions were as follows:

(1) On the basis that the yield lateral resistance of PC specimens was similar to RC, PC specimens had an average decrease of 15.8% in the first peak load and a remarkable increase of up to 89.8% in the ultimate load compared to RC.

(2) Bonded substructure BPC retained a considerable level of collapse resistance after the complete failure of one joint, indicating its high resilience against severe local damages.

(3) With a relatively low prestress, the premature failure of the bonded strand was successfully prevented in specimen BPCL, efficiently enhanced the ductility and collapse resistance of the bonded PC substructure. A prestress level of half of the yield strength was recommended.

(4) External steel angles and bonded strands could enhance the stiffness of substructures under the column loss scenario especially at the transmission from the compressive arch action to the catenary action. This significantly improved the dynamic performance of the PC substructure.

REFERENCES

[1] DoD, U. (2009). Unified facilities criteria: design of buildings to resist progressive collapse. UFC 4-023-03. United States Department of Defense.

[2] GSA (General Services Administration). (2013). Alternate path analysis & design guidelines for progressive collapse resistance. General Services Administration.

[3] Li, Y., Lu, X., Guan, H., & Ye, L. (2011). An improved tie force method for progressive collapse resistance design of reinforced concrete frame structures. Engineering Structures, 33(10), 2931-2942.

[4] Li, Y., Lu, X., Guan, H., Ren, P., & Qian, L. (2016). Probability-based progressive collapse-resistant assessment for reinforced concrete frame structures. Advances in Structural Engineering, 19(11), 1723-1735.

[5] Yu, J., & Tan, K. H. (2014). Special detailing techniques to improve structural resistance against progressive collapse. Journal of Structural Engineering, 140(3), 04013077.

[6] Yu, J., & Tan, K. H. (2014). Numerical analysis with joint model on RC assemblages subjected to progressive collapse. Magazine of concrete research, 66(23), 1201-1218.

[7] Qian, K., & Li, B. (2013). Performance of three-dimensional reinforced concrete beam-column substructures under loss of a corner column scenario. Journal of structural engineering, 139(4), 584-594.

[8] Parisi, F., & Scalvenzi, M. (2020). Progressive collapse assessment of gravity-load designed European RC buildings under multi-column loss scenarios. Engineering Structures, 209, 110001.

[9] Qian, K., & Li, B. (2015). Quantification of slab influences on the dynamic performance of RC frames against progressive collapse. Journal of Performance of Constructed Facilities, 29(1), 04014029.

[10] Qian, K., Lan, D. Q., Fu, F., & Li, B. (2020). Effects of infilled wall opening on load resisting capacity of RC frames to mitigate progressive collapse risk. Engineering Structures, 223, 111196.

[11] Yu, J., & Tan, K. H. (2014). Analytical model for the capacity of compressive arch action of reinforced concrete sub-assemblages. Magazine of Concrete Research, 66(3), 109-126.

[12] Priestley, M. N. (1996). The PRESSS program—current status and proposed plans for phase Ill. PCI journal, 4(2), 22-40.

[13] El-Sheikh, M. T., Sause, R., Pessiki, S., & Lu, L. W. (1999). Seismic behavior and design of unbonded post-tensioned precast concrete frames. PCI journal, 44(3), 54-71.

[14] Priestley, M. N., Sritharan, S., Conley, J. R., & Pampanin, S. (1999). Preliminary results and conclusions from the PRESSS five-story precast concrete test building. PCI journal, 44(6), 42-67.

[15] Shi, H. R., Yuan, Y., Qing, Y., Wang, C. L., & Liu, Y. (2022). Deformation and cyclic behavior of partially-restrained energy dissipaters with yielding end connections. Journal of Constructional Steel Research, 194, 107323.

[16] Wang, C. L., Liu, Y., Zheng, X., & Wu, J. (2019). Experimental investigation of a precast concrete connection with all-steel bamboo-shaped energy dissipaters. Engineering Structures, 178, 298-308.

[17] Wada, A., Sakata, H., Nakano, K., Matsuzaki, Y., Tanabe, K., & Machida, S. (2006). Study on Damage Controlled Precast-Prestressed Concrete Structure with P/C MILD-PRESSJOINT–Part 1: Overview of P/C Mild-Press-Joint Building Construction and its Practical Applications. In Proceedings of the 2nd FIB Congress (Vol. 400).

[18] Nakano, K., Tanabe, K., Matsuzaki, Y., Wada, A., Sakata, H., & Kuboyama, H. (2004). Experimental study on mechanical behavior of damage controlled precast-prestressed concrete structure with P/C MILDPRESS-JOINT. Proceedings of the 13th WCEE, Paper No, 2778.

[19] Qian, K., Liang, S. L., Xiong, X. Y., Fu, F., & Fang, Q. (2020). Quasi-static and dynamic behavior of precast concrete frames with high performance dry connections subjected to loss of a penultimate column scenario. Engineering Structures, 205, 110115.

[20] Qian, K., Liang, S. L., Fu, F., & Fang, Q. (2019). Progressive collapse resistance of precast concrete beam-column sub-assemblages with high-performance dry connections. Engineering Structures, 198, 109552.

[21] Zhao, Z., Cheng, X., Li, Y., Diao, M., Guan, H., & An, Y. (2023). Progressive collapse analysis of precast reinforced concrete beam-column assemblies with different dry connections. Engineering Structures, 287, 116174.

[22] Li, S., Wang, H., Liu, H., Shan, S., & Zhai, C. (2023). Experimental study on progressive collapse of self-centering precast concrete frame with infill walls. Engineering Structures, 294, 116746.

[23] Chinese Standard, G. B. (2008). 50011-2010. Code for Seismic Design of Buildings. Beijing, China: National Standard of the People's Republic of China (NSPRC).

[24] International Building Code (2003). International Code Council, Country Club Hills, IL, Sections 1613 to 1623.

[25] Tsai, M. H. (2010). An analytical methodology for the dynamic amplification factor in progressive collapse evaluation of building structures. Mechanics Research Communications, 37(1), 61-66.

Easy-to-use analytical model of compressive arch action of bi-directional primary RC beams in framed structures under different column removal scenarios

Bao Yintong[1], Qiao Meixia[2], and Tan Kang Hai[3]

[1] PhD, Nanyang Technological University (NTU), Singapore, yintong001@e.ntu.edu.sg.

[2] PhD, Nanyang Technological University (NTU), Singapore, meixia001@e.ntu.edu.sg.

[3] Professor, PhD, Nanyang Technological University (NTU), Singapore, ckhtan@ntu.edu.sg.

Corresponding Author: Tan Kang Hai, PhD.

Corresponding Author: Qiao Meixia, PhD.

School of Civil and Environmental Engineering, Nanyang Technological University,

Singapore, 639798.

Email: ckhtan@ntu.edu.sg , meixia001@e.ntu.edu.sg

ABSTRACT

Compressive arch action (CAA) in the affected sub-structural beams has pivotal role in mitigating progressive collapse resulting from column failure due to blast events, and how to predict the enhancement effect of CAA becomes urgent. However, the existing analytical models were developed to predict CAA in one-way reinforced concrete (RC) beams but not applicable to bi-directional primary beam system in framed structures. This study presents a user-friendly analytical model to predict CAA in bi-directional primary beams in framed structures under different column removal scenarios, incorporating different design details and horizontal restraint conditions of the beams in two directions, as well as different column removal scenarios (CMS).

To evaluate the validity of the analytical model, its predictions are contrasted with Finite Element Method（FEM) simulations of typical bi-directional RC sub-assemblages with diverse design details. This comparison confirms that the model can achieve good precision in predicting resistance and displacement of CAA. Furthermore, parametrical investigations are carried out to examine how the varied boundary condition under different column removal scenario, and span difference of bi-directional primary beams affect the peak resistance of CAA.

Keywords: *Progressive Collapse, Compressive Arch Action, Bi-directional Primary Beams, Analytical Model, Column Removal Scenarios.*

INTRODUCTION

When traditional reinforced concrete (RC) beams face a scenario where the central column is removed, the bridging beam over the missing column can effectively redistribute the vertical load to the supports at both ends via compressive arch action (CAA). Research has shown that the activation and intensity of CAA in the impacted beam largely rely on the conditions of horizontal restraint [1-7]. Furthermore, extensive analytical research [8-14] has been conducted to quantitatively assess CAA in RC frames. Notably, the semi-empirical method introduced by Park and Gamble [10] is broadly recognized for its ability to appraise the increased capacity of CAA and the maximum compression in the beam of RC structures. Nonetheless, the precision of this method is significantly influenced by the estimated displacement at the peak capacity of CAA, and the advantageous impact of CAA may be exaggerated due to the presumption of inflexible boundary conditions.

To more precisely reflect the stress conditions of longitudinal reinforcement during the CAA phase and boundary conditions, Yu and Tan [15] devised an implicit analytical model that accounts for the impact of rotational and horizontal restraints on CAA in RC sub-assemblies, capable of forecasting local shifts in the vertical load-displacement relationship at the apex of CAA resistance. Following this, Kang and Tan [16] enhanced the model by linking beam sag to the strain in the upper longitudinal reinforcement and the concrete at plastic hinge zones, enabling the prediction of the vertical load-displacement curve at the initial bending stage. Wang et al. [17] later introduced an implicit analytical model for CAA in RC sub-structures, which factored in the tension-stiffening effect of longitudinal steel bars post-cracking and the slippage of reinforcing bars at the ends of beams, thus improving precision. Azim et al. [18] applied Gene Expression Programming (GEP) to derive a GEP-based equation for estimating the CAA capacity of RC beam-column sub-assemblies, considering variables such as concrete strength, span-to-depth ratio, beam size, ratios of top and bottom longitudinal reinforcement, and normalized axial restraint stiffness. Additionally, Azim et al. [19] created a semi-analytical model to forecast CAA in RC beams, supported by an extensive database of 70 RC samples. This model used the GEP method to formulate a direct expression for CAA displacement based on the total net span and depth of the bridging beam. Consequently, the peak CAA capacity can be determined without iterative processes by combining the GEP technique with the revised Park and Gamble's model [10]. The precision of the predicted CAA displacement surpassed that of the original Park and Gamble's model and Lu's model, allowing for the computation of peak CAA capacity without iterative calculations, using the modified Park and Gamble's method and the determined CAA displacement.

However, the current models, originally designed for unidirectional primary beams, are not directly applicable to RC framed structures with primary beams oriented orthogonally in both X- and Y- directions. Specifically, the aggregate peak capacity of two orthogonally oriented primary beams cannot be accurately calculated by merely summing their individual peak capacities due to the current design methodology. This is attributed to a variety of factors, including differing beam spans, cross-sectional dimensions, and the varying horizontal restraint conditions present in the two orthogonal directions. These discrepancies may lead to the beams achieving their maximum CAA capacities at different vertical displacements, rendering the

simple addition of individual CAA peak capacities as potentially non-conservative. As a result, this limitation hinders the existing design methods from precisely predicting the CAA capacity in scenarios that involve the removal of penultimate, edge, and corner columns, where the impacted beams in the orthogonal X- and Y- directions may exhibit distinct design specifics and/or horizontal restraint conditions.

This paper introduces a novel, user-friendly analytical model that extends from a single-direction beam system to a bi-directional beam system within framed structures, enabling the prediction of CAA capacity for various column removal scenarios, including internal, penultimate, edge, and corner cases. This proposed model takes into account the bending curvature of the bridging double-span beam, along with the rotational and horizontal restraint conditions at the ends of the beam. Comparative analysis with 28 Finite Element Method (FEM) simulations demonstrates that the model accurately predicts the CAA capacity, displacement, and the maximal compression forces in the bi-directional primary beams. Additionally, a parametric study is presented to illustrate the influence of boundary conditions on the CAA capacity in two-way framed structures across different column removal scenarios.

DERIVATION OF CAA IN DIRECTIONAL RC BEAMS

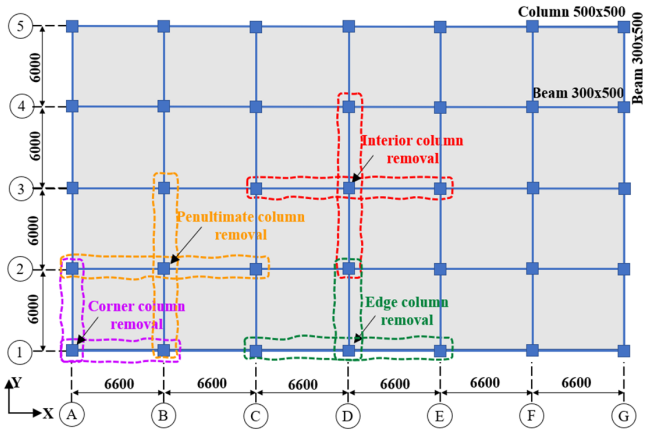

Fig. 1: Plan view of prototype structure (unit: mm)

Fig. 1 illustrates common column removal scenarios, each distinguished by the beam members that bear the vertical load where the column has been removed, and the specific horizontal restraint conditions at the ends of these beams. For instance, the removal of a corner column, like the one at grid A-1, affects the cantilever single-span beams extending from grids B-1 to A-1 in the X-direction and from grids A-2 to A-1 in the Y-direction, as highlighted by magenta lines. In such a scenario, the lack of horizontal restraint at the corner joint (where K_{ax} and K_{ay} are approximately equal to zero as shown in Fig. 2 (a)), prevents the activation of CAA, and the vertical load is supported solely by the flexural strength of the two cantilever single-span beams. Conversely, when the column at grid D-3 is removed, an interior column removal scenario, the affected two-span sub-assemblies in both directions, encircled by red lines in Fig. 1, benefit from adequate horizontal restraints (represented by K_{ax} and K_{ay} in Fig. 2 (c)) provided by the neighbouring beams. This allows for the development of CAA, which positively contributes to the vertical load resistance.

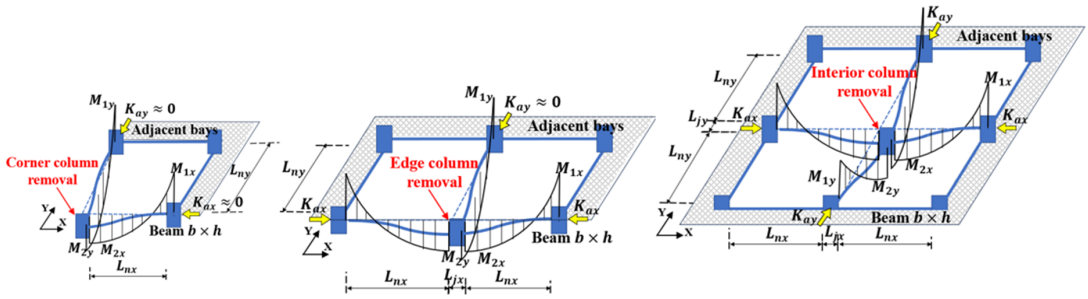

(a) Corner column removal (b) Edge column removal (c) Interior column removal

Fig. 2: Bending moment diagram of different column removal scenarios

Notes:
L_{nx} and L_{ny} represent the clear spans of single beams in X- and Y-directions, respectively.
M_{1x} and M_{2x} represent hogging moment at the side joint interface and sagging moment at the middle joint interface of the beam in X-direction, respectively.
M_{1y} and M_{2y} represent hogging moment at the side joint interface and sagging moment at the middle joint interface of the beam in Y-direction, respectively.
K_{ax} and K_{ay} represent the respective horizontal restraint stiffnesses of the beams in X- and Y-directions.
The shaded-filled regions represent adjacent bays providing boundary restraints.

Unlike the interior column removal scenario, the penultimate column removal scenario, such as at grid B-2, presents limited horizontal restraint from the edge column, which may not be adequate to fully activate CAA in the two-way bridging sub-assemblies. Regarding the edge column removal, consider the affected areas highlighted by green lines in Fig. 1 (a) above the removed column at grid D-1, with the corresponding moment diagram depicted in Fig. 2 (b). Here, the vertical load resistance at the position of the removed edge column is sustained by the double-span beams stretching from grids C-1 to E-1 in the X-direction, and by the cantilever single-span beam extending from grids D-2 to D-1.

Interior and penultimate column removal cases

The derivation process of interior column removal scenarios is elaborated in this section. The overall concept is to extend the force equilibrium and compatibility conditions from one-way beams to two-way beams in X- and Y-directions. Based on the moment diagrams shown in Fig. 2, the expression of vertical load P at the removed column position is shown below:

$$P = \frac{2}{L_{nx}}(M_{1x} + M_{2x} - N_x\delta - 0.5qL_{nx}^2) + \frac{2}{L_{ny}}\left(M_{1y} + M_{2y} - N_y\delta - 0.5qL_{ny}^2\right) \quad (1)$$

Based on the same assumptions proposed by Bao and Tan [20], when the beam end interfaces experience ductile bending failure (between the pure bending failure and balanced failure points in Fig. 3), the bending moments M (dash lines in Fig. 3 (a)) and neutral axis depth C (dash lines in Fig. 3 (b)) can be simplified as linear functions of compression force N, as expressed in Eqs. (2) and (3).

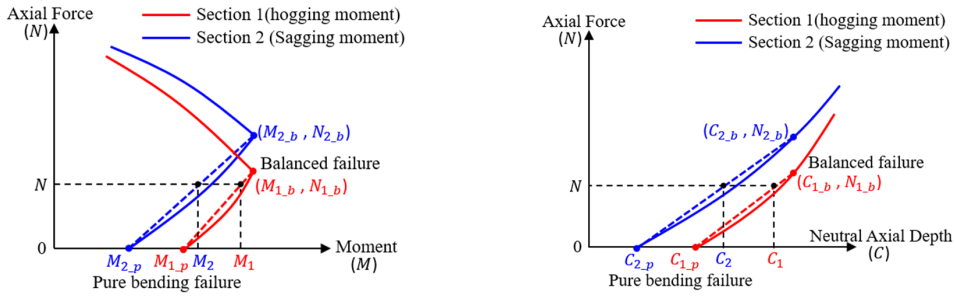

(a) Simplified M-N curve (b) Simplified C-N curve

Fig. 3. Linear assumptions of M-N and C-N relationships between pure moment status and balance failure status [20].

$$\begin{cases} M_1 = \left(\dfrac{M_{1\_b} - M_{1\_p}}{N_{1\_b}}\right) N + M_{1\_p} = m_1 N + M_{1\_p} \\ M_2 = \left(\dfrac{M_{2\_b} - M_{2\_p}}{N_{2\_b}}\right) N + M_{2\_p} = m_2 N + M_{2\_p} \end{cases} \tag{2}$$

$$\begin{cases} C_1 = \left(\dfrac{C_{1\_b} - C_{1\_p}}{N_{1\_b}}\right) N + C_{1\_p} = k_1 N + C_{1\_p} \\ C_2 = \left(\dfrac{C_{2\_b} - C_{2\_p}}{N_{2\_b}}\right) N + C_{2\_p} = k_2 N + C_{1\_p} \end{cases} \tag{3}$$

in which, M_{1_b} and N_{1_b} are the bending moment and the axial compression force at the left-end beam interface under balanced failure status, respectively, while C_{1_b} is the corresponding neutral axis depth. Clearly, M_{1_b} is the maximum bending moment at the balanced failure point in the axial force-bending moment interaction diagram (Fig. 3 (a)). The similar naming rule is applied to the expressions of M_2 and C_2 at the right-end beam interface.

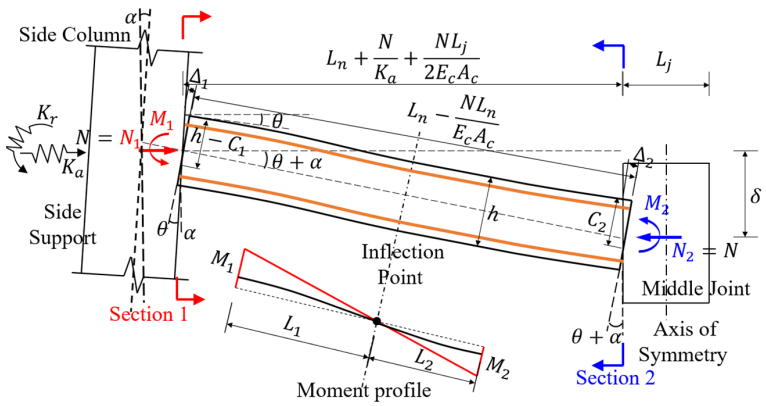

Fig. 4. Equilibrium and compatibility of bridging beams at CAA stage (only left-hand beam segment is shown due to Symmetry) [20].

Based on the compatibility condition proposed by Bao and Tan [20], as shown in Fig. 4, the axial compression force N_x and N_y at CAA stage can be expressed as functions of δ and horizontal restraint conditions at CAA stage, as expressed in Eq. (4).

$$\begin{cases} N_x = \dfrac{\delta + n_{3x}}{(n_{1x} + n_{2x}\delta)} \\ N_y = \dfrac{\delta + n_{3y}}{(n_{1y} + n_{2y}\delta)} \end{cases} \tag{4}$$

where:

$$\begin{cases} n_{1x} = \dfrac{\left[\dfrac{L_{nx}}{K_{ax}} + \dfrac{\beta L_{nx}^2}{E_c A_c} - (k_{1x} + k_{2x})(a_{1x}N_x + a_{2x})\right]}{\left(h - C_{1_{p_x}} - C_{2_{p_x}}\right)} \\ n_{2x} = \dfrac{(k_{1x} + k_2 x)}{\left(h - C_{1_{p_x}} - C_{2_{p_x}}\right)} \\ n_{3x} = -(a_{1x}N + a_{2x}) \end{cases}$$

$$\begin{cases} n_{1y} = \dfrac{\left[\dfrac{L_{ny}}{K_{ay}} + \dfrac{\beta L_{ny}^2}{E_c A_c} - \left(k_{1y} + k_{2y}\right)\left(a_{1y}N_y + a_{2y}\right)\right]}{\left(h - C_{1\_p\_y} - C_{2\_p\_y}\right)} \\ n_{2y} = \dfrac{\left(k_{1y} + k_{2y}\right)}{\left(h - C_{1\_p\_y} - C_{2\_p\_y}\right)} \\ n_{3y} = -\left(a_{1y}N + a_{2y}\right) \end{cases} \tag{5}$$

$$\begin{cases} a_1 = \dfrac{L_n^2}{3E_c I}[m_1\beta_5^2 + m_2(1-\beta_5)^2] + \dfrac{m_1}{K_r}L_n \\ a_2 = \dfrac{L_n^2}{3E_c I}\left[M_{1_p}\beta_5^2 + M_{2_p}(1-\beta_5)^2\right] + \dfrac{M_{1_p}}{K_r}L_n \\ \beta_5 = \dfrac{m_1 N + M_{1\_p}}{(m_1 + m_2)N + \left(M_{1\_p} + M_{2\_p}\right)} \end{cases}$$

Besides, when CAA capacity is attained, the relationships between bending moments at critical sections and axial compression forces of the beams in two directions are shown below:

$$\begin{cases} M_{1x} = \dfrac{M_{1\_b\_x} - M_{1\_p\_x}}{N_{1\_b\_x}}N_x + M_{1\_p\_x} = m_{1x}N_x + M_{1\_p\_x} \\ M_{2x} = \dfrac{M_{2\_b\_x} - M_{2\_p\_x}}{N_{2\_b\_x}}N_x + M_{2\_p\_x} = m_{2x}N_x + M_{2\_p\_x} \end{cases} \tag{6}$$

$$\begin{cases} M_{1y} = \dfrac{M_{1\_b\_y} - M_{1\_p\_y}}{N_{1\_b\_y}}N_y + M_{1\_p\_y} = m_{1y}N_y + M_{1\_p\_y} \\ M_{2y} = \dfrac{M_{2\_b\_y} - M_{2\_p\_y}}{N_{2\_b\_y}}N_y + M_{2\_p\_y} = m_{2y}N_y + M_{2\_p\_y} \end{cases} \tag{7}$$

Based on Eq. (1) to Eq. (7), vertical load P can be eventually represented as a function of δ, which is expressed as $P(\delta)$. The CAA capacity P_{CAA}, as the local maximum values of $P(\delta)$, can be obtained when displacement is equal to δ_{CAA} and $dP(\delta)/d\delta = 0$. The first derivative $dP(\delta)/d\delta$ of function $P(\delta)$ is expressed in Eq. (8), in which dM_{1x}/dN_x, dM_{2x}/dN_x,

dM_{1y}/dN_y, dM_{2y}/dN_y, can be obtained through Eq. (6) and Eq. (7), and $dN_x/d\delta$, $dN_y/d\delta$ can be calculated based on Eq. (4).

$$\left.\frac{dP}{d\delta}\right|_{\delta_{CAA}} = \left[\frac{2}{L_{nx}}\left(\frac{dM_{1x}}{dN_x}\frac{dN_x}{d\delta} + \frac{dM_{2x}}{dN_x}\frac{dN_x}{d\delta} - \left(N_x + \frac{dN_x}{d\delta}\delta\right)\right) + \frac{2}{L_{ny}}\left(\frac{dM_{1y}}{dN_y}\frac{dN_y}{d\delta} + \frac{dM_{2y}}{dN_y}\frac{dN_y}{d\delta} - \left(N_y + \frac{dN_y}{d\delta}\delta\right)\right)\right]\Bigg|_{\delta_{CAA}} = 0 \tag{8}$$

To satisfy $dP(\delta)/d\delta\,|\delta_{CAA} = 0$, the quartic equation of δ_{CAA} is expressed in Eq. (9).

$$C_4(\delta_{CAA})^4 + C_3(\delta_{CAA})^3 + C_2(\delta_{CAA})^2 + C_1(\delta_{CAA}) + C_0 = 0 \tag{9}$$

where:

$$C_4 = \frac{2}{L_{nx}}n_{2x}n_{2y}^2 + \frac{2}{L_{ny}}n_{2y}n_{2x}^2$$

$$C_3 = \frac{2}{L_{nx}}\left[2n_{1x}n_{2y}^2 + 2n_{2x}n_{1y}n_{2y}\right] + \frac{2}{L_{ny}}\left[2n_{1y}n_{2x}^2 + 2n_{2y}n_{1x}n_{2x}\right]$$

$$C_2 = \frac{2}{L_{nx}}\left[n_{1x}n_{3x}n_{2y}^2 + 4n_{1x}n_{1y}n_{2y} + n_{2x}n_{1y}^2 - (m_{1x}+m_{2x})(n_{1x}-n_{2x}n_{3x})n_{2y}^2\right] + \frac{2}{L_{ny}}\left[n_{1y}n_{3y}n_{2x}^2 + 4n_{1y}n_{1y}n_{2x} + n_{2y}n_{1x}^2 - (m_{1y}+m_{2y})(n_{1y}-n_{2y}n_{3y})n_{2x}^2\right]$$

$$C_1 = \frac{2}{L_{nx}}\left[2n_{1x}n_{3x}n_{1y}n_{2x} + 2n_{1x}n_{1y}^2 - 2(m_{1x}+m_{2x})(n_{1x}-n_{2x}n_{3x})n_{1y}n_{2y}\right] + \frac{2}{L_{ny}}\left[2n_{1y}n_{3y}n_{1x}n_{2y} + 2n_{1y}n_{1x}^2 - 2(m_{1y}+m_{2y})(n_{1y}-n_{2y}n_{3y})n_{1x}n_{2x}\right]$$

$$C_0 = \frac{2}{L_{nx}}\left[n_{1x}n_{3x}n_{1y}^2 - (m_{1x}+m_{2x})(n_{1x}-n_{2x}n_{3x})n_{1y}^2\right] + \frac{2}{L_{ny}}\left[n_{1y}n_{3y}n_{1x}^2 - (m_{1y}+m_{2y})(n_{1y}-n_{2y}n_{3y})n_{1x}^2\right]$$

After obtaining δ_{CAA}, the axial compression forces N_x and N_y at CAA stage can be calculated through (4. Thereafter, the bending moment at beam ends can be obtained based on (6 and (7. Finally, the CAA peak load P_{CAA} can be achieved based on the calculated δ_{CAA}, N_x, N_y, M_{1x}, M_{2x}, M_{1y}, M_{2y} of the two-span beams in two directions and Eq. (1).

Edge column removal cases

As for the cases of edge column removal, due to the absence of horizontal restraint at the end of the cantilever single-span beam, no enhancement effects can be considered and the pure flexural capacities ($M_{1\_p\_y}$ and $M_{2\_p\_y}$) are used to determine the contribution of this cantilever beam to the total vertical resistance P.

$$P = \frac{2}{L_{nx}}(M_{1x} + M_{2x} - N_x\delta - 0.5qL_{nx}^2) + \frac{1}{L_{ny}}\left(M_{1\_p\_y} + M_{2\_p\_y} - 0.5qL_{ny}^2\right) \quad (10)$$

The expression of total vertical resistance P is shown in Eq. (10). It could be found that only the vertical resistance arising from the one-way two-span beams in X-direction is influenced by CAA which is reflected by δ and axial compression force N_x. The resistance of Y-direction beam is a constant only determined by flexural capacities. Therefore, the local maximum resistance at CAA stage is determined by the one-way sub-assemblages in X-direction, and the calculation process can follow the design method developed for one-way sub-assemblages.

Corner column removal cases

For the corner column removal scenario, since the horizontal restraints are missing at free ends of the cantilever beams in X- and Y-directions, there are no compression forces and corresponding enhancements arising from CAA. The vertical resistance P is purely contributed by flexural action of the beams, which can be obtained through Eq. (11).

$$P = \frac{1}{L_{nx}}\left(M_{1\_p\_x} + M_{2\_P\_x} - 0.5qL_{nx}^2\right) + \frac{1}{L_{ny}}\left(M_{1\_p\_y} + M_{2\_p\_y} - 0.5qL_{ny}^2\right) \quad (11)$$

in which, $M_{1\_p\_x}$, $M_{2\_p\_x}$ are the pure flexural capacities at both ends of the beam in X-direction, while $M_{1\_p\_y}$, $M_{2\_p\_y}$ are those of the beam in Y-direction.

The whole calculation process in the analytical model to predict CAA of RC beams can be shown in Fig. 5.

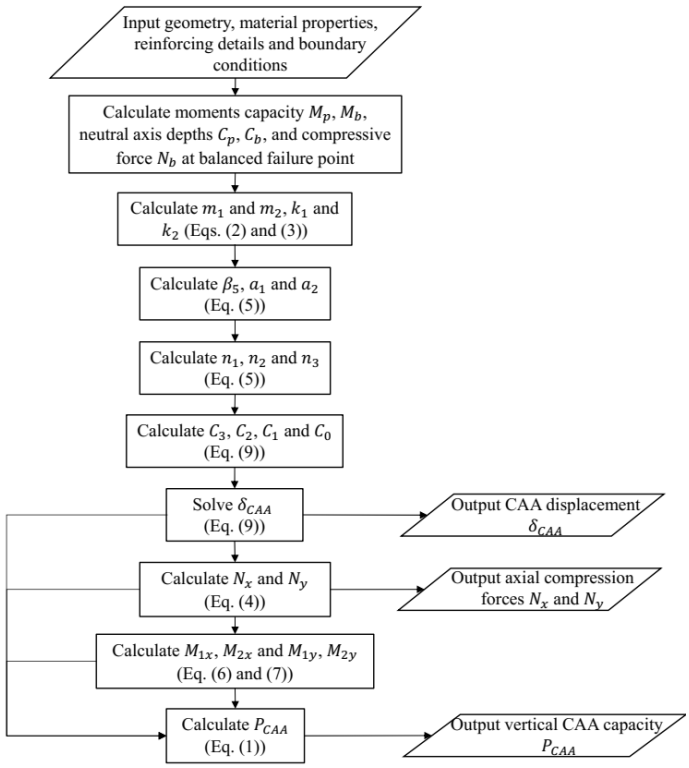

Fig. 5. Solution procedure for prediction of CAA of RC beams

VALIDATIONS AND DISCUSSIONS

Due to insufficient experimental data of bi-direction primary beams under MCRS, a series of finite element (FE) models were created by using OpenSees which is a widely accepted software to simulate the progressive collapse of concrete structures. A total of 28 FE models with various horizontal restraint stiffness at beam ends, clear span, height and width of beams, top and bottom reinforcement and concrete compressive strength were built to compare with the predictions of the proposed analytical model. The parameters in FE simulations and comparison are summarised in Table 1.

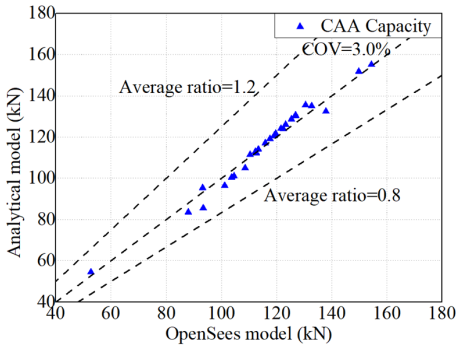

Fig. 6. Comparison on CAA capacity

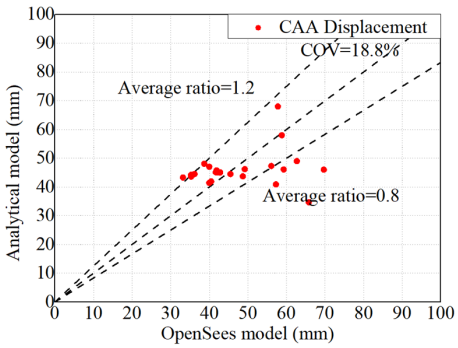

Fig. 7. Comparison on CAA displacement

Based on the comparison in Table 1 and Fig. 6, it is found that the average ratio of CAA capacities between the proposed analytical models to OpenSees FE models is 1.001 with a coefficient of variation of 3.0%. Besides, the CAA displacement is also well predicted with an average ratio of 1.015 and a coefficient of variation of 18.8%. As for estimating the maximum axial compressive forces of bi-direction beams at CAA stage, the average ratios of calculation to experimental values are 0.932 and 0.933 with coefficients of variation of 14.4% in X- and Y- directions. It can be concluded that the proposed analytical model is reliable to predict CAA enhancement in bi-directional primary beams with incorporating the effects of different horizontal restraint conditions, clear span, height and width of primary beams, top and bottom reinforcement and concrete compressive strength.

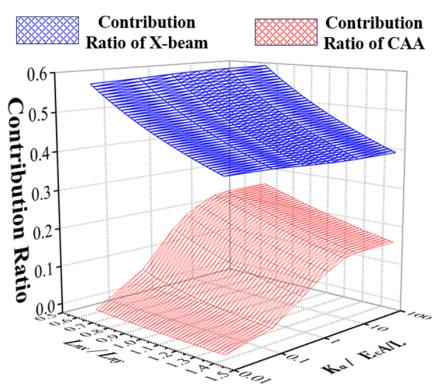

Fig. 8. CAA enhancement ratio under different ratios of L_{nx}/L_{ny} and $K_a/(E_cA/L)$

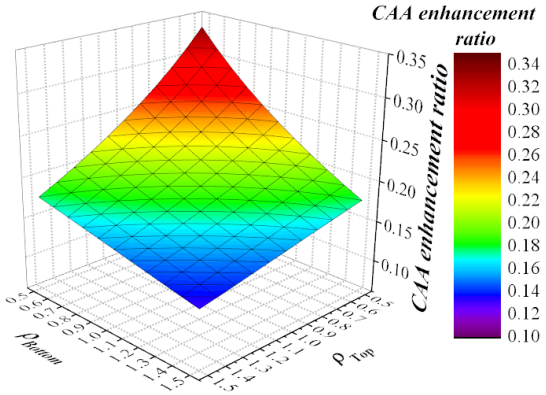

Fig. 9. Contribution of X-beam under different reinforcing ratios ρ_{Bottom} and ρ_{Top}

Based on the proposed model, parametric studies were conducted to investigate the effect of boundary conditions, reinforcing ratios and span ratio of bi-directional beams on the individual contribution of bi-direction beams and CAA enhancement effect.

Table 1. Comparisons between results of analytical models and OpenSees models

No.	x- span L_{nx} (m)	y- span L_{ny} (m)	x- horizotal restraint K_{ax} (x10^8N/m)	y- horizotal restraint K_{ay} (x10^8N/m)	Beam height h (m)	Beam width b (m)	Top steel bars A_{s_top}	Bottom steel bars A_{s_bot}	Concrete compressive strength f_c (MPa)	CAA capacity P (kN)			CAA displacement δ (m)			Maximum compressive force N_x (kN)			Maximum compressive force N_y (kN)		
										A	O	A/O	A	O	A/O	A	O	A/O	A	O	A/O
1	2.75	2.5	4.29	4.29	0.25	0.15	3H13	2H13	27.9	123.9	122.5	1.011	44.5	45.5	0.978	163.1	186.3	0.875	176.2	185.6	0.949
2	2.75	2.75								117.1	115.9	1.010	45.4	41.8	1.086	164.9	186.3	0.885	164.9	186.3	0.885
3	2.75	3.0								111.5	110.4	1.010	46.2	49.2	0.939	166.3	186.4	0.892	154.2	186.4	0.827
4	2.5	2.5								130.7	126.9	1.030	43.6	35.3	1.235	174.6	185.5	0.941	174.6	185.5	0.941
5	2.75	2.75	0.0000001	0.0000001	0.25	0.15	3H13	2H13	27.9	95.4	93.2	1.024	68.0	57.8	1.176	≈0	≈0	1.000	≈0	≈0	1.000
6			0.1x4.29	0.1x4.29						105.0	108.6	0.967	58.0	58.8	0.986	84.8	77.0	1.101	84.8	77.0	1.101
7			10x4.29	10x4.29						120.6	119.1	1.013	41.9	40.5	1.035	183.8	230.5	0.797	183.8	230.5	0.797
8			100x4.29	100x4.29						120.9	119.2	1.014	41.4	40.0	1.035	186.0	235.3	0.790	186.0	235.3	0.790
9	2.75	2.75	4.29	4.29	0.15	0.15	3H13	2H13	27.9	54.5	52.7	1.034	34.7	65.8	0.527	53.1	92.3	0.575	53.1	92.3	5.776
10					0.2					83.6	88.0	0.950	40.9	57.3	0.714	105.8	157.0	0.674	105.8	157.0	0.674
11					0.275					135.6	130.5	1.039	47.3	56.1	0.843	195.7	196.1	0.998	195.7	196.1	0.998
12					0.3					155.2	154.4	1.005	49.0	62.7	0.781	227.1	210.5	1.079	227.1	210.5	1.079
13	2.75	2.75	4.29	4.29	0.25	0.125	3H13	2H13	27.9	112.3	112.7	0.996	46.1	59.3	0.777	134.5	163.8	0.821	134.5	163.8	0.821
14						0.175				121.7	119.7	1.017	45.1	41.7	1.082	194.6	204.8	0.950	194.6	204.8	0.950
15						0.2				126.1	123.3	1.023	45.1	42.3	1.066	223.6	222.4	1.005	223.6	222.4	1.005
16						0.225				130.3	126.9	1.027	45.1	42.8	1.054	251.8	239.0	1.054	251.8	239.0	1.054
17	2.75	2.75	4.29	4.29	0.25	0.15	2H10	2H13	27.9	85.6	93.4	0.916	43.3	33.2	1.304	177.3	153.5	1.155	177.3	153.5	1.155
18							3H10			96.5	101.2	0.954	44.2	35.3	1.252	174.5	158.0	1.104	174.5	158.0	1.104
19							2H13			100.5	103.7	0.969	44.5	36.2	1.229	173.1	161.9	1.069	173.1	161.9	1.069
20							4H13			132.5	137.9	0.961	46.0	69.7	0.660	154.4	228.7	0.675	154.4	228.7	0.675
21	2.75	2.75	4.29	4.29	0.25	0.15	3H13	2H10	27.9	101.1	104.6	0.967	43.7	48.7	0.897	165.7	219	0.757	165.7	210	0.789
22								3H10		112.9	112.3	1.005	45.0	42.8	1.051	165.4	194.5	0.850	165.4	194.5	0.850
23								3H13		135.1	132.7	1.018	47.0	40.0	1.175	160.4	159.1	1.008	160.4	159.1	1.008
24								4H13		151.8	149.8	1.013	48.1	38.7	1.243	153.3	139.1	1.102	153.3	139.1	1.102
25	2.75	2.75	4.29	4.29	0.25	0.15	3H13	2H13	25	114.1	113.4	1.006	45.8	41.9	1.093	146.0	147.1	0.993	146.0	147.1	0.993
26									30	119.2	117.6	1.014	45.3	41.9	1.081	178.4	194.8	0.916	178.4	194.8	0.916
27									35	124.1	121.6	1.021	45.1	42.1	1.071	210.0	214.2	0.980	210.0	214.2	0.980
28									40	128.7	125.4	1.026	45.1	42.6	1.059	240.7	232.4	1.036	240.7	232.4	1.036
Mean Value												1.001			1.015			0.932			0.933
COV												3.0%			18.8%			14.4%			14.4%

Notes: ‘A’ refers to analytical model, ‘O’ referes to OpenSees model, and ‘A/O’ refers to ratio of results between analytical models and OpenSees model; COV: Coefficients of Variation.

Fig. 8 shows that with a smaller ratio L_{nx}/L_{nx} (referring to a shorter span of X-beams), the contribution ratio of X-beams to the total vertical resistance was increased from 0.39 to 0.58, as shown by the blue lines. Besides, the changing horizontal restraint condition has little effect on the increasing trend. This higher resistance contribution of X-beams under a shorter beam span is not only attributable to a stronger flexural action, but also caused by a larger CAA enhancement effect which can be reflected by the red curves in Fig. 8. When horizontal restraint is strong, the enhancement ratio of CAA (referring to the contribution factor of CAA to the total vertical resistance) can increase from 0.17 to 0.28. Furthermore, Fig. 9 demonstrates that when the bottom reinforcing ratio ρ_{Bottom} and top reinforcement ratio ρ_{Top} of the bi-directional beams are small, CAA enhancement effect becomes more prominent, and the ratio reaches up to 0.33.

PARAMETRIC STUDY

The prototype structure, depicted in Fig. 1, is a 4-storey concrete frame with span lengths of 6.6 m in the X-direction and 6.0 m in the Y-direction. It features a standard floor height of 3.0 m, beams measuring 300 mm in width and 500 mm in depth, and columns that are 500 mm square. The slab is 130 mm thick, and the concrete has a compressive strength of 38 MPa and an elastic modulus of 27.84 GPa. Due to 1/2 scale ratio used in the test specimens and subsequent predictions by using the proposed approaches, the prototype frame is also scaled down to 1/2 in the following calculations. The beam reinforcement in the X-direction consists of 3H13 bars at both the top and bottom, while in the Y-direction, there are 3H13 bars at the top and 2H13 at the bottom, aligning with specimen S4 from Yu's study [21]. This variation in span lengths and reinforcement configurations in the X and Y directions is intended to more accurately reflect a situation in reality.

Table 2.Predicted CAA of 2-span sub-assemblages under different CRS

Removed column position (Fig. 1)	X-direction K_{ax} ($\times 10^8$ N/m)	Y-direction K_{ay} ($\times 10^8$ N/m)	Classification of column removal	CAA capacity (kN)	CAA disp. (mm)	X-direction N_x (kN)	Y-direction N_y (kN)
A-1	0	0	C-CRS	56.4	77.8	0	0
B-1	0.029	0	EP-CRS	85.9	89.5	8.1	0
C-1	2.09	0	E-CRS	92.5	79.5	166.7	0
D-1	3.60	0	E-CRS	93.6	77.8	189.8	0
A-2	0	0.017	E-CRS	83.8	86.0	0	5.5
B-2	0.25	0.24	IP-CRS	117.2	84.7	52.2	60.8
C-2	5.08	0.24	I-CRS	123.9	78.1	204.9	54.0
D-2	8.92	0.23	I-CRS	124.5	77.1	219.1	51.1
A-3	0	2.39	E-CRS	92.6	73.1	0	183.7
B-3	0.25	6.25	IP-CRS	125.7	72.7	39.9	225.6
C-3	9.43	8.00	I-CRS	133.6	72.5	205.2	232.4
D-3	12.05	7.81	I-CRS	133.8	72.3	210.0	231.4

Notes:
K_{ax} represents X-direction horizontal restraint stiffness at beam ends, while K_{ay} is the Y-direction horizontal restraint stiffness at beam ends. The Vierendeel girder action in multiple storeys is not considered.
C-CRS represents corner column removal scenario, EP-CRS represents edge penultimate column removal scenario, E-CRS represents edge column removal scenario, IP-CRS represents interior penultimate column removal scenario, I-CRS represents interior column removal scenario.

Taking into account the building's planar symmetry, Column Removal Scenarios (CRS) are examined within grids A to D in the X-direction and grids 1 to 3 in the Y-direction. The corresponding horizontal restraint stiffness k_{ax} and k_{ay} , for both directions, along with the Compressive Arch Action (CAA) capacity of the impacted sub-assemblies featuring different beam-column joint configurations, are all detailed in Table 2.

To facilitate a clearer comparison of vertical resistance at various column removal locations, Fig. 10 (a) encapsulates the CAA predictions. Transitioning from a penultimate CRS at grid B-2 to an interior CRS at grid D-3 results in a 14.2% increase in the CAA capacity of RC sub-assemblies, attributable to the more robust horizontal restraints in both directions. Moreover, the CAA capacity at the corner CRS of grid A-1 is below 43% of that in the interior scenario at grid D-3, due to the absence of horizontal restraints necessary for CAA activation. With adequate horizontal restraints, as seen in the column removal at grid D-3, the CAA capacity exceeds the vertical resistance from mere flexural action by 18%. In scenarios like the corner CRS at grid A-1 and the edge penultimate CRS at grids A-2 and B-1, the horizontal restraints at the beam ends are markedly weak, rendering the CAA's contribution to vertical resistance from flexural action virtually insignificant (under 2%). Nonetheless, the traditional plastic hinge theory, indicated by red dashed lines, fails to account for the increased vertical resistance afforded by CAA when horizontal restraints are sufficiently rigid.

As depicted by the black lines in Fig. 10 (b), the proposed model effectively accounts for the scenario where increased horizontal restraint leads to reduced vertical displacement at the peak of vertical resistance during the CAA phase. Additionally, in the corner CRS instances at grid A-1, the vertical displacement predicted by the proposed model is substantially greater (approximately 55% higher) than the estimates of the plastic hinge theory. This discrepancy arises because the proposed model adequately incorporates the flexural curvature deformation of cantilever beams, a factor that the plastic hinge theory does not capture due to its assumption of rigid-body rotation.

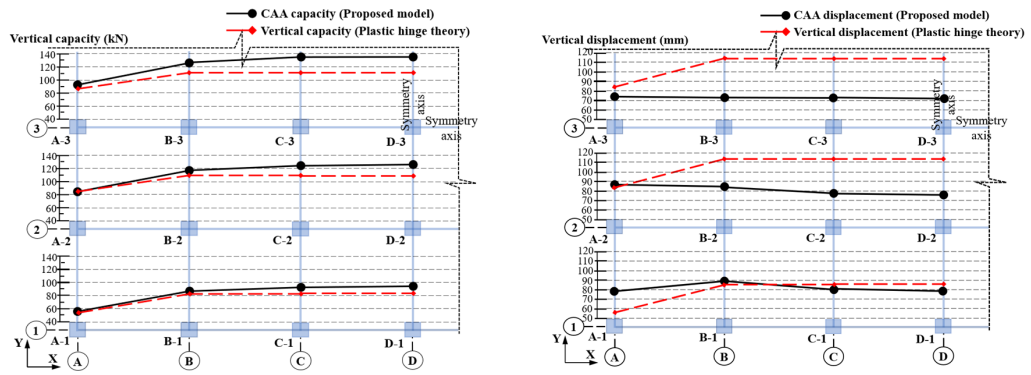

(a) Vertical capacities (b) Vertical displacements

Fig. 10. Vertical resistances and displacements under different CRS

CONCLUSIONS

In this paper, a user-friendly analytical model is introduced for assessing the compressive arch action (CAA) in RC framed sub-structures with bi-directional primary beams under different

column removal. The model incorporates common design details such as different horizontal restraint conditions, clear span and sections of the beams, reinforcement details and concrete compressive strengths. To validate the model, it is compared against simulation results obtained from finite element models. The key findings of this study are summarized as follows:

1 The proposed model can predict the combined contribution of CAA from the bi-directional primary beams with incorporating different design details and boundary conditions of the beams in X- and Y- directions, instead of summing up the individual capacities of the beams and generating non-conservative CAA capacity. This could not be achieved by previous analytical models.
2 The proposed model is an explicit model and does not require complex iterative calculations. This can be easily employed in practical collapse-resisting design.
3 The proposed model can well predict the CAA capacity, CAA displacement, maximum compression forces in bi-direction beams. Based on comparisons with FEM simulations, the accuracy of this model is acceptable.
4 Parametric studies on CAA enhancement effects of 2-way framed substructures shows that the horizontal restraint conditions under different column removal scenarios will highly affect the CAA capacity and displacement. At CAA stage, the penultimate and edge column removal scenarios have much lower resistances than the interior column removal case.

REFERENCES

1. Yu, J. and K.H. Tan, Experimental and numerical investigation on progressive collapse resistance of reinforced concrete beam column sub-assemblages. J Engineering Structures, 2013. **55**: p. 90-106.
2. Yi, W.J., et al., Experimental study on progressive collapse-resistant behavior of reinforced concrete frame structures. J ACI Structural Journal, 2008. **105**(4): p. 433.
3. Yu, J. and K.H. Tan, Structural behavior of reinforced concrete frames subjected to progressive collapse. ACI structural journal, 2017. **114**(1): p. 63-74.
4. FarhangVesali, N., et al., Development of arching action in longitudinally-restrained reinforced concrete beams. Construction, 2013. **47**: p. 7-19.
5. Qian, K., B. Li, and J.X. Ma, Load-carrying mechanism to resist progressive collapse of RC buildings. Journal of Structural Engineering, 2015. **141**(2): p. 04014107.
6. Su, Y., Y. Tian, and X. Song, Progressive collapse resistance of axially-restrained frame beams. J ACI Structural Journal, 2009. **106**(5).
7. Rankin, G., A. Long, and Buildings, ARCHING ACTION STRENGTH ENHANCEMENT IN LATER ALLY-RESTRAINED SLAB STRIPS. Proceedings of the Institution of Civil Engineers Structures, 1997. **122**(4): p. 461-467.
8. GSA, Alternate path analysis & design guidelines for progressive collapse resistance. General Services Administration, 2013.
9. Guice, L.K., T.R. Slawson, and E.J. Rhomburg, Membrane analysis of flat plate slabs. Structural Journal, 1989. **86**(1): p. 83-92.
10. Park, R. and W.L. Gamble, Reinforced concrete slabs. 1999: John Wiley & Sons.
11. Li, Y., et al., An improved tie force method for progressive collapse resistance design of reinforced concrete frame structures. Engineering Structures, 2011. **33**(10): p. 2931-

2942.
12. Lu, X., et al., New analytical calculation models for compressive arch action in reinforced concrete structures. Engineering Structures, 2018. **168**: p. 721-735.
13. Lim, N.S., K.H. Tan, and C.K. Lee, A simplified model for alternate load path assessment in RC structures. Engineering Structures, 2018. **171**: p. 696-711.
14. Almusallam, T., et al., Development limitations of compressive arch and catenary actions in reinforced concrete special moment resisting frames under column-loss scenarios. 2020. **16**(12): p. 1616-1634.
15. Yu, J. and K.H. Tan, Analytical model for the capacity of compressive arch action of reinforced concrete sub-assemblages. Magazine of Concrete Research, 2014. **66**(3): p. 109-126.
16. Kang, S.B. and K.H. Tan, Analytical Model for Compressive Arch Action in Horizontally Restrained Beam-Column Subassemblages. ACI Structural Journal, 2016. **113**(4).
17. Wang, S., J. Peng, and S.B. Kang, Evaluation of compressive arch action of reinforced concrete beams and development of design method. Engineering Structures, 2019. **191**: p. 479-492.
18. Azim, I., et al. Prediction model for compressive arch action capacity of RC frame structures under column removal scenario using gene expression programming. in Structures. 2020. Elsevier.
19. Azim, I., et al. Semi-analytical model for compressive arch action capacity of RC frame structures. in Structures. 2020. Elsevier.
20. Bao, Y. and K.H. Tan, Analytical model of compressive arch action for one-way RC beams and two-way framed substructures under column removal scenarios. Engineering Structures, 2024. **304**: p. 117694.
21. Yu, J. and K.-H. Tan, Experimental and numerical investigation on progressive collapse resistance of reinforced concrete beam column sub-assemblages. Engineering Structures, 2013. **55**: p. 90-106.

PROTECT2024